

# New Slip Synthesis and Theoretical Approach of CVT Slip Control

THÈSE N° 4337 (2009)

PRÉSENTÉE LE 13 MARS 2009

À LA FACULTÉ SCIENCES ET TECHNIQUES DE L'INGÉNIEUR  
LABORATOIRE DE SYSTÈMES ROBOTIQUES 1  
PROGRAMME DOCTORAL EN SYSTÈMES DE PRODUCTION ET ROBOTIQUE

ÉCOLE POLYTECHNIQUE FÉDÉRALE DE LAUSANNE

POUR L'OBTENTION DU GRADE DE DOCTEUR ÈS SCIENCES

PAR

Yves ROTHENBÜHLER

acceptée sur proposition du jury:

Prof. M.-O. Hongler, président du jury  
Prof. H. Bleuler, Prof. J. Giovanola, directeurs de thèse  
Dr G. Carbone, rapporteur  
Dr Ph. Müllhaupt, rapporteur  
J. van Rooij, rapporteur



ÉCOLE POLYTECHNIQUE  
FÉDÉRALE DE LAUSANNE

Suisse  
2009



# Preface

This project deals with the analysis and control of continuously variable transmissions (CVT) with the objective of optimizing their performance. The idea of analyzing the slip of each pulley and the theoretical tool to describe the continuously variable transmission has originated from the industrial need to understand more clearly the behavior of the variator. Mr. Kazuo Rokkaku gave me the opportunity to conduct this project as an employee at the Research & Development Center of JTEKT Co. in Nara, Japan. Simultaneously, this thesis has been under the supervision by Professor Jacques Giovanola and Professor Hannes Bleuler. Moreover, this research was possible only under the licensee agreement and research cooperation between JTEKT Co. and Gear Chain Industrial B.V. (GCI), located in Nuenen, Netherlands.

This thesis reflects not only technical achievements, but also a professional and a cultural experience. Every year, with a business trip from Japan, I had the opportunity to go to the Netherlands to discuss with GCI engineers and to visit EPFL to discuss my progress with my supervisors. Living in Japan and exchanging ideas with people from different cultures was a rich experience both humanly and socially.

This thesis results from many discussions I have shared with others whom I thank for their time and interest. I am particularly grateful to the following people:

Mr. Kazuo Rokkaku, my general manager, for giving me the opportunity to undertake this thesis under good conditions and supported me during this work.

Professor Jacques Giovanola and Professor Hannes Bleuler, who encouraged and also supported me for this abroad Ph.D. Despite the long distance between Japan and Switzerland, they provided advice and guidance during this work.

Dr. Philippe Müllhaupt for his continuous support on the control aspects of this work.

All the members of the Mechatronic Systems Research and Development Department of JTEKT Co., Mr Kenji Asano, Mr Shigeo Kamamoto, Mr Seiji Tada, Mr. Joel Kuster and Ms. Kozue Matsumoto. My special thanks goes to Mr. Yasuhiko Hasuda, my direct colleague; with him I have worked and shared most of this experience.

Mr. Isaac Theraz and Mr. Leos Urbanek for their direct contributions through their internships.

All the staff members of Gear Chain Industrial B.V. for the interesting discussions we had during my visit in the Netherlands. Especially, I would like to thank Mr. Jacques Van Rooij, CEO of Gear Chain Industry B.V., for his constant support and for accepting to be one of my external experts.

Dr. Giuseppe Carbone for giving me some of his time and for accepting to be one of my external experts.

My overwhelming gratitude goes to my wife Akiko and to my children Yulika and Lei. The free time with my children gave me the opportunity to relax. My wife's daily support was most appreciated during the ups and downs of this thesis endeavor.



# Contents

<b>Contents</b>	<b>v</b>
<b>Abstract</b>	<b>ix</b>
<b>Résumé</b>	<b>xi</b>
<b>1 Introduction</b>	<b>1</b>
1.1 Contribution . . . . .	2
1.2 Outlines . . . . .	3
<b>2 Belt or chain type continuously variable transmission</b>	<b>5</b>
2.1 Intermediate element . . . . .	5
2.1.1 Metallic belt . . . . .	5
2.1.2 CVTs chain . . . . .	5
2.2 Hydraulic system . . . . .	7
2.3 CVT efficiency . . . . .	9
2.3.1 Loss due to slip . . . . .	9
2.3.2 Pump losses . . . . .	10
2.3.3 Belt-related torque losses . . . . .	10
2.4 Efficiency improvement strategies . . . . .	11
2.4.1 Variator losses improvement . . . . .	11
2.4.2 Hydraulic losses . . . . .	12
2.5 System used in this thesis . . . . .	14
2.6 Summary . . . . .	14
<b>3 New slip synthesis</b>	<b>17</b>
3.1 Pulley slip . . . . .	17
3.2 New analysis of the total slip . . . . .	18
3.3 Traction coefficients . . . . .	20
3.3.1 Micro and macro slip definition . . . . .	22
3.4 Discussion of new slip synthesis . . . . .	22
3.4.1 Standard slip synthesis . . . . .	22
3.4.2 New slip synthesis . . . . .	23
3.4.3 Comparison of the two synthesis . . . . .	24
3.4.4 Remark . . . . .	25
3.5 Efficiency . . . . .	25

3.6	Stability analysis with a simple model . . . . .	28
3.7	Summary . . . . .	30
<b>4</b>	<b>Low level model</b>	<b>33</b>
4.1	State of the art . . . . .	33
4.2	Geometric model of the variator . . . . .	34
4.3	Steady-state model of the variator . . . . .	37
4.3.1	Kinematic model . . . . .	37
4.3.2	Mechanical model . . . . .	40
4.3.3	Friction coefficient . . . . .	42
4.4	Elastic deformation . . . . .	43
4.4.1	Pulley deformation . . . . .	43
4.4.2	Pulley sheave and shaft clearance . . . . .	45
4.4.3	Pin compression . . . . .	46
4.4.4	Pulley radius deformation . . . . .	46
4.5	Numerical procedure . . . . .	48
4.6	Intermediate element speed . . . . .	49
4.6.1	Geometrical ratio constant . . . . .	49
4.6.2	Speed ratio constant . . . . .	50
4.7	Efficiency model . . . . .	50
4.7.1	Hertz contact . . . . .	50
4.7.2	Friction forces and moments . . . . .	51
4.7.3	Chain efficiency . . . . .	53
4.8	Simulation . . . . .	54
4.8.1	Chain forces and slip . . . . .	55
4.8.2	Variator matrix . . . . .	56
4.8.3	Shifting . . . . .	56
4.9	Summary . . . . .	56
<b>5</b>	<b>High level model</b>	<b>59</b>
5.1	State of the art . . . . .	59
5.1.1	Variator dynamics . . . . .	59
5.1.2	Servo pumps modelling . . . . .	60
5.2	System interactions . . . . .	60
5.2.1	Actuators interactions . . . . .	60
5.2.2	Hydraulic and variator interactions . . . . .	60
5.3	Actuator models . . . . .	60
5.3.1	Control mode of the servo pump . . . . .	62
5.3.2	Servo pump model . . . . .	62
5.4	Hydraulic model . . . . .	63
5.5	Shifting model . . . . .	64
5.6	Slip model . . . . .	64
5.7	Mechanical model . . . . .	65
5.8	Variator dynamics with slip . . . . .	67
5.8.1	Linearized model . . . . .	67
5.9	Summary . . . . .	68

<b>6</b>	<b>Simulation and experiment comparisons</b>	<b>69</b>
6.1	Test bench . . . . .	69
6.1.1	Pulley radius measurement . . . . .	70
6.1.2	Chain speed measurement . . . . .	71
6.2	Low level model . . . . .	71
6.2.1	Clamping force . . . . .	71
6.2.2	Slip and traction coefficient . . . . .	71
6.3	High level model . . . . .	73
6.3.1	Geometrical model validation . . . . .	75
6.3.2	Variator model . . . . .	76
6.4	Summary . . . . .	76
<b>7</b>	<b>Variator control</b>	<b>81</b>
7.1	State of the art . . . . .	81
7.2	Actuator flow control . . . . .	82
7.2.1	Control problem . . . . .	83
7.2.2	Flow control design with pole placement . . . . .	83
7.2.3	Design validation of the flow control . . . . .	85
7.3	Pressure control . . . . .	85
7.3.1	Pressure control constraint . . . . .	85
7.3.2	Input-Output feedback linearization design . . . . .	85
7.3.3	Pressure linear control design . . . . .	87
7.4	Ratio and secondary clamping force control . . . . .	88
7.4.1	Secondary clamping force control . . . . .	89
7.4.2	Speed ratio control design . . . . .	89
7.5	Validation of the variator control design . . . . .	90
7.6	Summary . . . . .	92
<b>8</b>	<b>Slip control</b>	<b>93</b>
8.1	State of the art . . . . .	93
8.2	Slip control problem . . . . .	93
8.2.1	Slip control strategy . . . . .	94
8.2.2	Frequency response . . . . .	94
8.3	Slip control with PI . . . . .	96
8.3.1	Simple feedforward design . . . . .	96
8.3.2	Mapping feedforward design . . . . .	97
8.3.3	Bode diagram for the PI control . . . . .	97
8.4	Slip control with model reference adaptive control . . . . .	97
8.4.1	Slip control with MRAC . . . . .	100
8.5	Slip control performances . . . . .	102
8.5.1	Efficiency gain . . . . .	102
8.5.2	Torque perturbations . . . . .	102
8.5.3	Speed ratio perturbations . . . . .	105
8.5.4	Frequency response . . . . .	106
8.6	MRAC parameters . . . . .	108
8.7	Summary . . . . .	108

<b>9</b>	<b>Conclusions and recommendations</b>	<b>111</b>
9.1	Recommendations . . . . .	113
<b>A</b>	<b>Differential equations of the pulley slip</b>	<b>115</b>
A.1	Primary slip . . . . .	115
A.2	Secondary slip . . . . .	116
<b>B</b>	<b>Other figures</b>	<b>119</b>
B.1	Traction coefficient . . . . .	119
B.2	Pulley radiuses and traction coefficients . . . . .	119
B.3	Experiments and simulation . . . . .	119
B.4	Clamping force comparison . . . . .	119
<b>C</b>	<b>Pulley deformation comparison</b>	<b>127</b>
C.1	Sattler model . . . . .	127
C.2	Deformation comparison . . . . .	127
<b>D</b>	<b>Servo pump: detailed model</b>	<b>131</b>
D.1	Motor model . . . . .	131
D.2	Pump model . . . . .	133
D.2.1	Hydraulic model . . . . .	133
<b>E</b>	<b>Standard slip</b>	<b>135</b>
<b>F</b>	<b>Linearization</b>	<b>137</b>
<b>G</b>	<b>Testing facilities</b>	<b>141</b>
G.1	Electric motor . . . . .	141
G.2	Dynamo . . . . .	141
G.3	Input and output sensor . . . . .	141
G.4	CVT variator . . . . .	143
G.5	Hydraulic system . . . . .	143
G.5.1	Servo amplifier . . . . .	143
G.5.2	Servo motor . . . . .	143
G.5.3	Pump . . . . .	144
G.6	Test bench control . . . . .	144
<b>H</b>	<b>CVT Linear Control</b>	<b>145</b>
H.1	Transfer function . . . . .	145
H.2	Secondary pressure control . . . . .	146
H.3	Ratio control . . . . .	146
	<b>Nomenclature</b>	<b>147</b>
	<b>Bibliography</b>	<b>151</b>
	<b>Curriculum Vitae</b>	<b>159</b>

# Abstract

Today's vehicle must be efficient in terms of gas (CO<sub>2</sub>, NO<sub>x</sub>) emissions and fuel consumption. Due to improvements in material and oil, the continuous variable transmission (CVT) is now making a breakthrough in the automotive market. The CVT decouples the engine from the wheel speed. CVT enables significant fuel gains by shifting the engine operating point for specific power demands. This optimization of the operating point enables a reduction of this fuel consumption.

A CVT is constituted of two pulley sheaves, one fixed and the other one movable in its axial direction when subjected to an external axial force, in general hydraulic. The transition from the minimum to the maximum speed ratio is continuous and an infinite numbers of ratio is available between these two limits. An intermediate element (a metallic belt or chain) transmits the power from the input (the primary) to the exit (the secondary) of the CVT or variator.

Further improvements of the fuel consumption and gas emission are still required for example by improving the variator efficiency. Increasing hydraulic performance or decreasing mechanical losses by reducing the axial forces are some solutions. The latter method is not without risks. The diminution of the clamping forces increases the slip between pulley sheaves and the intermediate element. If the axial forces decrease too much, high slip values can be reached and cause damage to the pulleys and the intermediate element. Control of the slip is an attractive solution to decrease the clamping forces in order to safely improve the variator efficiency.

The objective of this thesis is to understand and model the slip of each pulley and establish analytic tools dedicate to the variator control. The slip study and the theoretical approach of the CVT variator is applied to the slip control of the variator with a chain.

The contribution of this work is threefold. Firstly, the slip and the traction coefficient are analyzed for each pulley. The slip analysis of each pulley is then used to define a new slip synthesis as the summation of the slip of each pulley. It is demonstrated that the slip and the traction coefficient are different for each pulley and depend on the speed ratio of the variator. In low ratios, both the secondary pulley and the primary pulley slip, but only the primary reaches macro slip. For middle or higher ratios, only the secondary pulley slips and reaches high values of slip. Experiments show that the pulley with the smallest clamping force limits the system. Secondly, based on

kinematics, force equilibrium, elastic deformations of the pulleys and the intermediate element, a detail model of the variator is proposed. The principal results are the estimation of the clamping forces, of the traction curve for each pulley and of the chain efficiency. These results are implemented in a simpler model that describes the variator dynamics. This last model considers the two pulleys and the intermediate element as free bodies. The hydraulic circuit and the actuators, which are important to take into account for control, are also modeled. Thirdly, the new slip synthesis and the results of the dynamic models are applied to the slip control of the variator in order to improve the efficiency. A pole placement law is applied to the actuators to control the flow that enters or exits the pulleys. With this law, the actuators are decoupled and the bandwidth is increased sufficiently for actuators dynamics to be neglected. The primary and the secondary pressures are decoupled and linearized by an input-output feedback linearization. The resulting system is linear and linear control theory can be applied to control the two pressures. The speed ratio is controlled by the primary clamping force. The secondary pressure is chosen as a function of the control mode of the variator: standard mode or slip mode. In standard mode, the intermediate element is overclamped by 30%, whereas in slip mode, the secondary clamping force is set as a function of the desired slip. By controlling the slip at 2%, the mechanical efficiency was increased by more than 2% and the clamping forces reduced by more than 30%. For the slip control, a proportional-integrator law and a model reference adaptive control (MRAC) are presented and the performances compared. The MRAC gives slightly better results.

**Keywords:** CVT, variator, metallic belt, chain, slip, traction, efficiency, pole placement, non-linear control, model reference adaptive control (MRAC).

# Résumé

De nos jours, les fabricants de voitures doivent de plus en plus faire face aux exigences d'émission de CO<sub>2</sub> et NO<sub>x</sub>. Les récents progrès technologiques dans les domaines des matériaux, des huiles de lubrification, ont permis l'essor des boîtes à vitesses continue (Continuous Variable Transmission, CVT). Ces transmissions découplent la vitesse du moteur par rapport à celle des roues. Son utilisation permet d'optimiser le point d'opération du moteur pour une puissance donnée. Cette optimisation permet une réduction de la consommation d'essence.

Une CVT est constituée d'une poulie dont une moitié est fixe et l'autre mobile dans sa direction axiale sous une certaine force externe, en général sous forme hydraulique. La transition du rapport minimum au rapport maximum est continue et une infinité de rapports de transmission est possible entre ces deux bornes. Un élément intermédiaire (une courroie métallique ou une chaîne) transmet la puissance entre l'entrée (le primaire) et la sortie (le secondaire) de la boîte à vitesses, aussi appelée variateur.

Il est encore possible de diminuer l'émission des gaz en augmentant le rendement de la transmission, par exemple en améliorant le système hydraulique, ou en diminuant les pertes mécaniques par une réduction des forces axiales de serrage. Cette dernière méthode n'est pas sans risque. La diminution des forces de serrages augmente le glissement entre les poulies et l'élément intermédiaire. Si des grandes valeurs de glissement sont atteintes, les poulies et l'élément intermédiaire peuvent être endommagés. En contrôlant le glissement, il est donc possible de diminuer les forces dans le système et d'augmenter le rendement en toute sécurité.

L'objectif de cette thèse est d'étudier le glissement de chaque poulie et d'établir une approche théorique dédiée au contrôle du variateur. Cette nouvelle définition du glissement ainsi que cette approche théorique du modèle de la CVT sont appliquées au contrôle du glissement d'un variateur et d'une chaîne comme élément intermédiaire.

Trois contributions de ce travail méritent d'être soulignées. Premièrement, le glissement et le coefficient de traction sont analysés pour chaque poulie et additionnés pour estimer le glissement total du variateur. Il est montré que le glissement et le coefficient de traction sont différents pour chaque poulie et dépendent du rapport de transmission. Dans les bas rapports, le secondaire et le primaire glissent, mais seulement le primaire atteint de grandes valeurs de glissement. En revanche, dans les moyens et hauts rapports, seul le sec-

ondaire glisse. Les expériences montrent que la limite du système (grandes valeurs de glissement) est atteinte par la poulie avec la plus petite force de serrage. Deuxièmement, basé sur la cinématique, l'équilibre des forces, la déformation des poulies et de l'élément intermédiaire, un modèle détaillé du variateur est obtenu. Les principaux résultats consistent en une estimation des forces de serrage, de la courbe de traction de chaque poulie et du rendement de la chaîne. Ces résultats sont utilisés dans un modèle plus simple qui décrit la dynamique du variateur. Ce modèle considère les poulies et la chaîne comme des éléments indépendants. Il décrit également la dynamique du circuit hydraulique et des actionneurs, éléments importants à considérer pour le contrôle. Troisièmement, la nouvelle définition du glissement et les résultats des modèles sont appliqués au contrôle du glissement dans le but d'augmenter le rendement du variateur. La stratégie du placement de pôles découple les actionneurs et augmente leurs bandes passantes. Les bandes passantes des actionneurs deviennent suffisamment élevées par rapport au reste du système et les actionneurs peuvent être négligés. Un contrôle non linéaire de l'entrée sur la sortie (input-output feedback linearization) linéarise et découple les pressions de chaque poulie. Le système étant devenu linéaire, les théories du contrôle linéaire peuvent être utilisées pour contrôler les deux pressions. La pression du primaire est utilisée pour contrôler le rapport de transmission et la pression du secondaire est choisie en fonction du mode de contrôle: mode standard, mode de glissement. En mode standard, la chaîne est surserrée de 30%; en mode de glissement, elle est asjutée en fonction de la valeur de glissement désirée. Ce dernier mode augmente le rendement mécanique du variateur de 2% et diminue les forces de serrage de plus de 30%. Pour le contrôle du glissement, un proportionnel-intégrateur (PI) et un contrôle adaptatif avec modèle de référence (Model Reference Adaptive Control, MRAC) sont présentés et les performances comparées. Les performances du MRAC sont légèrement meilleures que le PI.

**Mots Clés:** CVT, variateur, courroie métallique, chaîne, glissement, traction, rendement, placement de pôle, contrôle non linéaire, contrôle adaptatif avec modèle de référence.



# Chapter 1

## Introduction

Today's vehicle must be efficient in terms of emissions and fuel consumption. The development of continuously variable transmission (CVT) technology has proved its effectiveness in providing a solution to reduce the fuel consumption while maintaining good vehicle performances. The CVT for use in automotive powertrains is motivated by the added ability of optimizing the engine operation point. This ability means that for the same power, the engine of a vehicle containing a CVT can operate at lower regime. A significant reduction in fuel consumption can then be achieved.

The concept of CVT based powertrains was introduced over 100 years ago. However it is only because of improvements in material and oil over the past 30 years, that this technology is now making a breakthrough in automotive market (metallic belt, chain, half or full toroidal).

Further improvements are still required, notably the fuel consumption reduction obtained by the optimized operation of the engine and the efficiency of the transmission. Development on infinitely variable transmission (IVT) will enable an optimization of the engine. The hybrid electric vehicle (HEV) reduces idle emissions by shutting down the combustion engine and restarting it when needed (start-stop system). A HEV's engine is smaller than a non-hybrid petroleum fuel vehicle and may be run at various speeds, providing more efficiency. A good control of clamping forces or an improvement of the hydraulic circuit will lead to an improvement of the transmission efficiency for a variator type belt or chain.

This thesis focuses on belt or chain type CVT. A CVT variator is composed of two variables conical pulleys with a fixed center distance and connected by an intermediate element (metallic belt or chain). One of the conical sheaves is movable in its axial direction under the influence of an axial force. The variator can have an infinite number of transmission ratios bounded by the low ratio, called underdrive (UD), and the high ratio, called overdrive (OD).

The power transmission from the primary pulley (input of the variator) to the intermediate element and the intermediate element to the secondary pulley (output of the variator) occurs through friction forces of a finite number of contact points. An equivalent friction coefficient can be defined and called the traction coefficient. This coefficient mainly depends on the slip value between

the pulley sheaves and the intermediate element. A traction curve can then be defined that relates the traction coefficient with the slip. The slip value is directly related to the clamping forces.

High clamping forces decrease the slip by augmenting friction forces and then reduce the efficiency. In contrast, low clamping forces increase the slip and if the clamping forces are too small, the power transmission is not longer possible and the variator efficiency reduces to zero. An optimum of the variator efficiency can then be found. In usual CVT control, the intermediate element is over clamped, a situation leading to unnecessary losses. The diminution of clamping forces is then a solution to improve the variator efficiency, but not without risk: with too low clamping forces, large slip values can be reached and damage the variator (macro slip), furthermore the system becomes unstable. As the slip depends strongly on clamping forces, the control of the slip is an attractive solution to safely reduce the clamping forces in order to improve the variator efficiency (Bonsen (2006)).

## 1.1 Contribution

The contribution of this work is twofold. Firstly the primary and the secondary slip involved in the CVT are modelled to define a new total slip synthesis. This new synthesis is applied to a CVT variator with an involute chain <sup>1</sup> as intermediate element. More specifically, the main technical achievements are outlined in the following points:

- New synthesis of the slip and the traction curve by analyzing them separately for each pulley. The slip and the traction curve of each pulley are estimated using the speed of the pulleys and the intermediate element speed.
- Using this new synthesis of the slip analyzes, the total slip of the variator is estimated and the dynamics derived to obtain a complete model of the variator considering each element as a free body.
- Development of a generic slip control based on the new slip synthesis. The nonlinear control technique of input-output feedback linearization is applied to control the two pressures and two different control laws (a proportional-integrator (PI) controller and a model reference adaptive control (MRAC)) are outlined to control the slip.

Secondly, use of a theoretical approach to reach the goal of the slip control. At first a low level model of the variator is considered. Based on kinematics and force equilibrium, pulley forces, torques, slip and traction curves for each pulley are calculated. These results are then used in a high level model that describes the dynamic of the CVT considering the slip of each pulley. Finally, this tool can be used for the synthesis of the CVT control and especially for achieving slip control.

---

<sup>1</sup>Covered an international patent

## 1.2 Outlines

The structure of this thesis comprises four parts. First, the belt or chain type CVT technologies are described. Losses of the variator are pointed out and some solutions to improve them are also given. Secondly, the new slip synthesis is presented and compared with the actual synthesis. Also, the stability of the system is briefly tackled. Third, a theoretical overview composed of two levels of CVT modeling is introduced and validated. Fourthly the new total slip synthesis is applied to slip control of the variator in order to improve the efficiency.

Most readers may wish to focus their interest only on certain specific parts. Readers interested only on the basics of the belt or chain type CVT should consult *Chapter 2*. The new total slip synthesis and the efficiency of the variator are discussed in *Chapter 3*. Detail information on the CVT variator modeling can be found in *Chapter 4*, with a more general view in *Chapter 5*. *Chapter 6* presents the validation of these models. Readers interested in control should read *Chapter 7* for the general control of the CVT variator and *Chapter 8* for the slip control. A brief description of each chapter is given in the following lines.

*Chapter 2* describes in more details the variator, the intermediate element and the actuators used to control the system. Also, different approaches to improve the efficiency of the variator are proposed.

*Chapter 3* discusses the slip in the variator by defining the slip and the traction curve of each pulley and finally obtaining a new synthesis of the total slip of the variator. The new synthesis is also compared with the usual one. Then, the efficiency and losses of the variator are discussed. The last section of this chapter discusses the slip stability on the basis of simple model.

Based on force equilibrium, *Chapter 4* describes the low level model of the variator. This model describes in details forces involved in the system, deformations of the different elements constituting the variator, and the slip between intermediate element and pulleys. It also gives an estimating of the traction curve and efficiency of the variator.

*Chapter 5* models the variator with a more general view i.e. consider external forces and torques acting on the system. Considering the slip of each pulley and the result of the low level model, differential equations and the linearization of the variator dynamics are derived. This high level model considers the three elements forming the variator (two pulleys, one intermediate element) as free bodies.

*Chapter 6* compares the experimental data with simulation results with the models outlined in the two previous chapters. This validation gives the level of reliability and the limitations of these models.

*Chapter 7* depicts the design of the variator control. The primary clamping force is used to control the speed ratio. The secondary clamping force defines a based clamping force to avoid the slip of the intermediate element. The control design includes the flow control for each pulley flow, the input-output feedback linearization to linearize and decouple the system and finally the

variator control.

The new synthesis of the total variator slip is used in *Chapter 8* to outline the slip control design of the variator. The ratio control is similar to the control describes in the previous chapter. The secondary clamping force is used to control the slip. The slip reference is defined to be the slip value where the efficiency is maximum or near this maximum. Two slip controllers are proposed: a PI controller and a Model Reference Adaptive Control (MRAC). Some results and comparisons of the two slip controllers performances are also discussed.

Finally the last chapter, *Chapter 9*, gives a summary of the major results and contributions of the theses. Some recommendations for extending this work are also given.

## Chapter 2

# Belt or chain type continuously variable transmission

The variator of the continuously variable transmission (CVT), type belt or chain, consists of three bodies: the primary pulley, the intermediate element and the secondary pulley as shown in Figure 2.1. Each pulley is composed of two conical sheaves. One of the conical sheave is fixed; the other one is movable along its axial direction under the influence of an axial force. The variator has an infinite number of transmission ratios bounded by the low ratio, called underdrive (UD), and the high ratio called overdrive (OD). The power is transmitted from the primary pulley, input of the variator, to the intermediate element, then the last one transmits the power to the secondary pulley, the output of the variator. Friction forces of a finite number of contact points are the main mechanisms that transmit the power.

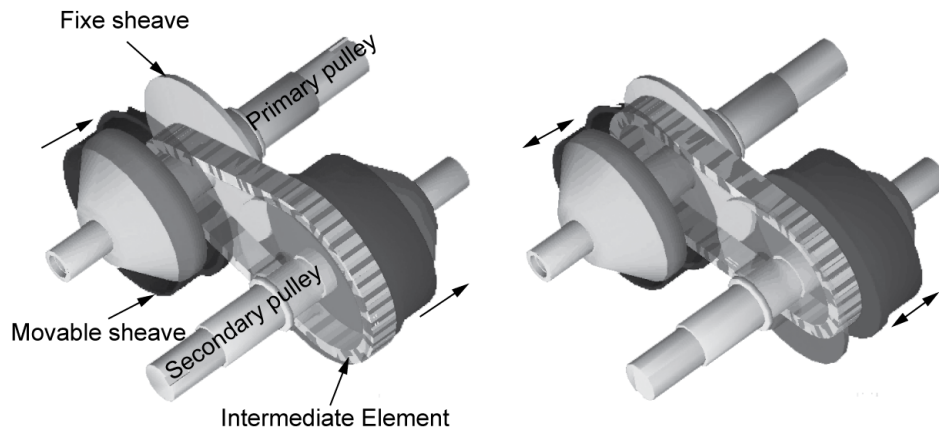
### 2.1 Intermediate element

#### 2.1.1 Metallic belt

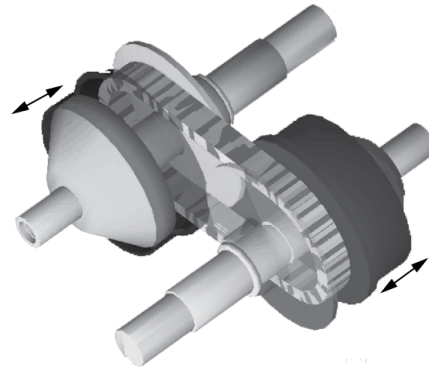
The metallic belt is the most wide spread in the market. It consists of laminated steel bands holding steel elements called V-shaped steel elements or blocks (Figure 2.2). The torque is transmitted from the primary to the secondary mainly by the compression between blocks and the rest is transmitted by the tension in the bands. There is a combined push-pull action in the belt that enables torque transmission.

#### 2.1.2 CVTs chain

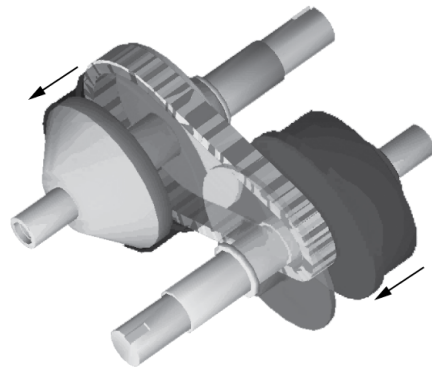
In contrast with the metallic belt, the chain transmits torque only by tensile force. The advantage of the chain is a higher transmission torque compared to the belt, but the disadvantage is the noise. As far as we know, two CVT



(a) Low ratio (underdrive)



(b) Medium ratio (1:1)



(c) High ratio (overdrive)

Figure 2.1: Variator type belt or chain in low ratio (underdrive), medium ratio (1:1) and high ratio (overdrive)

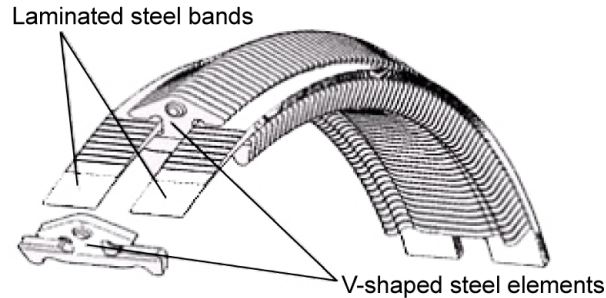


Figure 2.2: Metallic belt

chains are used: the LuK chain (Figure 2.3(a)) and the Involute Chain <sup>1</sup> (Figure 2.3(b)).

### LuK Chain

The LuK chain is already on the market. Stacks of links and rocker-pins constitute it. The two rocker-pins are in contact with the pulley sheave. The two rocker-pins are inconstant over a circular rolling surface. This chain can transmit higher power than the metallic belt and also, maybe more importantly, has a better efficiency (Englisch et al. (2004), Linnenbruegger et al. (2007)). The LuK pulleys differ from the metallic belt pulleys by the crowning of the pulleys sheave (Linnenbruegger et al. (2004)).

### Involute Chain

The Involute Chain is constituted by three elements: stack of links, pins and strips. The strip is shorter than the pin and only the pin is clamped between the two pulley sheaves. Strips and pins are in rolling contact over a flat, respectively involute surface. The pulleys for the chain are identical to the metallic belt pulleys and the belt can be easily replaced by the involute chain. The main advantages are a lower price and a higher efficiency than the metallic belt (Shastri & Franck (2004), van Rooij et al. (2007)).

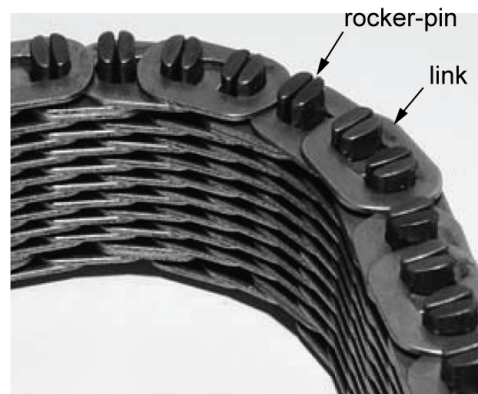
## 2.2 Hydraulic system

Generally, a hydraulic system gives the necessary pressures (forces) to clamp the intermediate element between the pulley sheaves. To generate the necessary flow, the usual method (Figure 2.4) uses a hydraulic pump connected to the engine shaft. Valves control the primary and the secondary pressures. The secondary pressure (or secondary clamping force) provides a line pressure to avoid the slip between the pulley sheaves and the intermediate element.

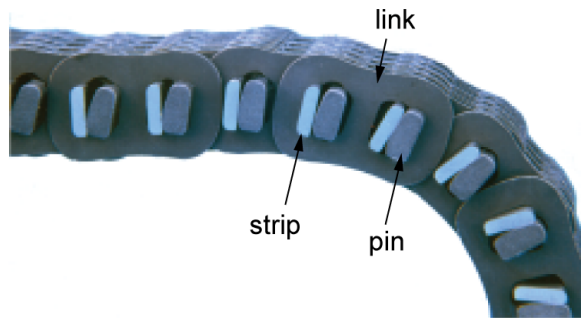
<sup>1</sup>Held an international patent

CHAPTER 2. BELT OR CHAIN TYPE CONTINUOUSLY  
VARIABLE TRANSMISSION

8



(a) LuK Chain (trade mark)



(b) Involute Chain (trade mark)

*Figure 2.3: CVT Chains*



The primary pressure controls the ratio by changing the forces equilibrium for the shifting or by keeping it for a fixe ratio.

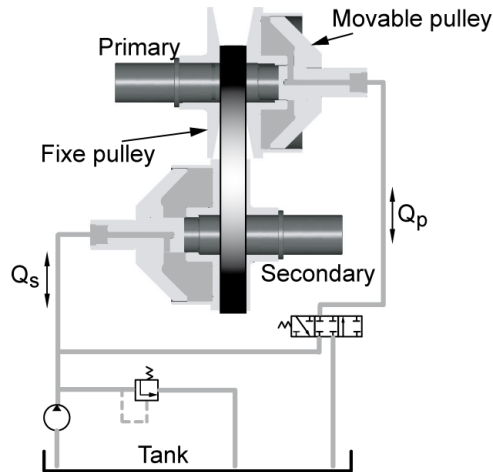


Figure 2.4: Hydraulic system using valves to set the pulleys pressures

## 2.3 CVT efficiency

High clamping forces needed to transmit the torque reduce the efficiency of the CVT. To prevent the slip of the belt or the chain, clamping forces are usually higher than needed for normal operation. A safety factor  $S_f$ , of at least 30% is usually used. High clamping forces result in increasing pump losses and friction forces.

The CVT efficiency is influenced by three main factors:

- Loss due to slip
- Pump loss
- The belt-related torque loss

### 2.3.1 Loss due to slip

For both chains and metallic belts, the slip loss is mainly due to slip between pulley sheaves and the intermediate element. In the case of the metallic belt, losses also occurred between each band and between bands and blocks due to relative motions. Blocks are running along a line of the rocking edges so the metallic belt is continuous along this line. Each band is running at different velocity i.e. the outer bands will run faster than the inner bands (Micklem et al. (1994b, 1996)).

Different authors have studied the loss mechanisms of the metallic belt or chain. Sattler (1999) analyzes the power losses by considering not only pulley

deformations but also the longitudinal and transversal stiffness of the chain. A series of three papers details an investigation of the loss mechanism of the metallic belt (Akehurst et al. (2004a,b,c)). The first paper analyzes the losses that occur due to relative motion between the bands and the segments of the metallic belt. The second paper focuses on the loss between the pulleys and the metallic belt due to pulley deflection effects. Finally, the third paper presents a number of models to predict the metallic belt-slip losses based on force distribution models. Poll et al. (2006) study the efficiency of the transmission by considering the pulley and shaft deformations and Poll & Meyer (2007) study the losses due to the sliding motion and the ratio change. The problem is solved by a set of differential equations for the forces and motions coupled with FEM computations of the deformations.

### **2.3.2 Pump losses**

The hydraulic pump is connected to the engine and it is spinning as long as the engine is running. It is always over designed to ensure sufficient pressure under all conditions. The pump is designed for a situation in which the shifting speed of the variator is maximum thus requiring high oil flow, while the engine connected to the pump rotates at low speed. When the engine rotates at higher speed, the excess flow under pressure is discharged to the sump by a pressure relief valve and, as such, causes losses, which increase the fuel consumption of the car (Ide (1999)).

### **2.3.3 Belt-related torque losses**

Belt-related torque losses are described by Micklem et al. (1994a). It is caused by the radial sliding losses when the metallic belt enters or exits the pulleys. When the blocks of the belt enter the pulley, the pulley sheave deforms and the blocks are compressed. The blocks will slightly move radially against friction forces between the block and the pulley sheave. A certain amount of energy is needed to overcome these frictions forces both on entry and exit of the pulleys, and large radial forces are required.

At the entry of the pulley, the radial forces arise. The penetrations of the blocks into the pulley take a finite time, the pulley turns a small angle when the block of the belt enters with a larger radius than the equilibrium one. The equilibrium radius will be reached after a small rotation angle of the pulley.

At the exit of the pulley, the blocks stay inside the two pulley sheaves until a reverse angle of the metallic belt provides a sufficient radial force component from the tension of the bands to remove the segment clamped between the two pulley sheaves. The exit radius will tend to be smaller than the equilibrium radius.

The difference between the pulley radius and the equilibrium radius increases the required input torque. The extra torque providing the energy is dissipated in the sliding losses.

## 2.4 Efficiency improvement strategies

To summaries, the losses of a CVT can be divided in two different types of losses: the variator and the hydraulic losses. The variator losses or the mechanical losses mainly come from the relative sliding of the different elements making up the variator. The hydraulic losses are due to the over design of the hydraulic pump.

Different solutions exist to reduce the variator and the hydraulic losses to improve the efficiency of the CVT variator.

### 2.4.1 Variator losses improvement

#### CVT Chain

The losses of the metallic belt due to sliding of the different elements forming the belt are quite important and could be reduced by replacing it by a CVT chain as it was discussed in *Section 2.1.2*. Linnenbruegger et al. (2007) and Bradley & Frank (2002) show the higher efficiency of the LuK chain and the Involute Chain respectively compared to the metallic belt. The losses of the bands that constitute the belt are minimized in CVT chains, furthermore, the belt related torque loss at the exit of the pulley is smaller with the chain than the metallic belt (Rothenbühler (2005)).

#### Reducing of the clamping forces

The intermediate element (metallic belt or chain) is over-clamped to avoid excessive slip between this element and the pulley sheaves. These over-clamping forces give a certain safety margin against unknown disturbances but increase friction and variator losses. Furthermore, the hydraulic system should provide more flow at higher pressure and then the hydraulic losses become higher. On the other hand, too small clamping forces reduce friction forces and increase slip (Figure 2.5). If clamping forces are too small, adequate power cannot be transmitted and the efficiency decreases. As shown in Figure 2.6, a maximum of the efficiency exists and depends on the slip value of the variator.

Faust et al. (2002), Bonsen (2006) and Kurosawa & Okahara (2007), for example, propose to reduce the clamping forces to improve the efficiency of the variator. Smaller clamping forces mean decreasing the safety margin. That is not without risk because the variator becomes susceptible to external perturbations and macro-slip can occur and damage the variator (van Drogen & van der Laan (2004)). Due to this uncertainty, the slip of the variator should be controlled. Bonsen (2006) presents a slip control strategy and shows its validity.

He measures slip through the primary pulley position to determine the geometrical ratio. Faust et al. (2002) measure slip by a clamping force modulation. In the over clamping range, the secondary pulley speed is not affected by the modulation. However, the oscillations increase as slip augments and the frequency corresponds to the modulation frequency of the clamping force.

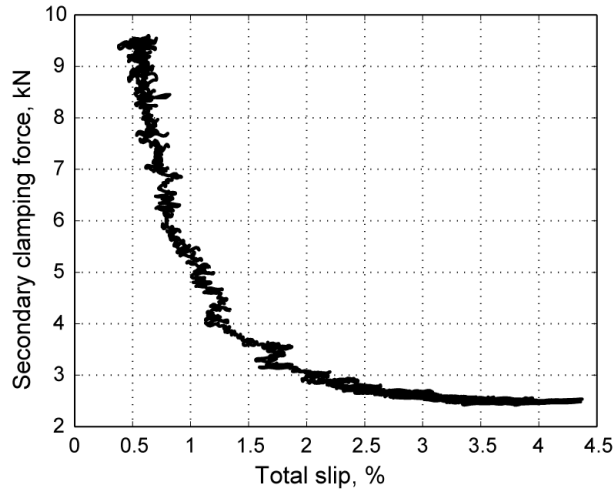


Figure 2.5: Secondary clamping force as a function of the total slip of the variator

Sakagami et al. (2007) identify slip by measuring the transfer function between the secondary and the primary rotation speeds. When belt slip occurs between the belt and the pulley sheaves, the transmitted energy is partially absorbed by the friction. If some disturbance is applied to the primary pulley, the resultant response through the variator is modified.

## 2.4.2 Hydraulic losses

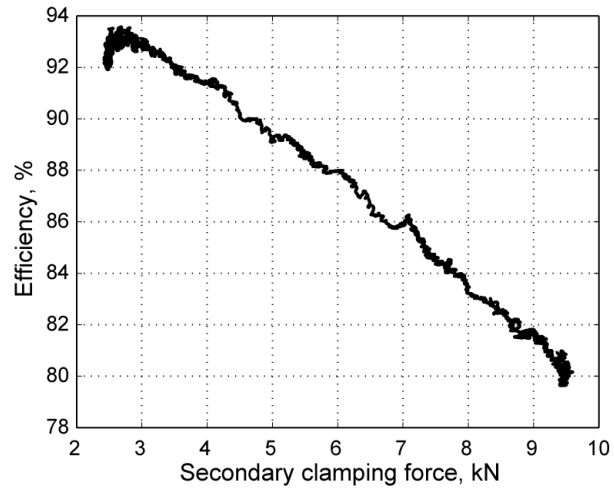
### Servo pump system

Bradley & Frank (2002) use a servo pump hydraulic system<sup>2</sup> using two servo pumps (Figure 2.7) to provide the desired flow. The shifting pump displaces the primary pulley flow  $Q_p$ , from the primary to the secondary pulley (or vice versa) in order to control the speed ratio. The clamping pump controls the secondary clamping force  $F_s$  by the displacement of the flow  $Q_{ps}$ . As this system works on flow demand, a part of the excessive flow is eliminated. When the ratio is not changing, the pumps need to deliver the flow to compensate the leak. This system reduces the control power required by more than 83% and approximately a 5% improvement in vehicle fuel economy is possible (Bradley & Frank, 2002).

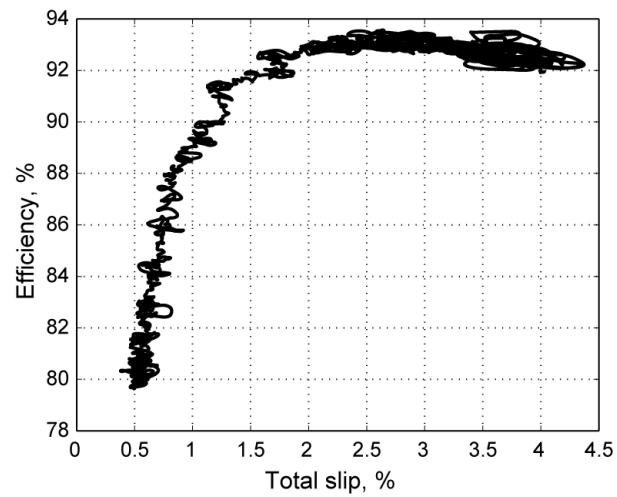
### Electromechanical actuator

van de Meerakker et al. (2004) and Klassen (2007) propose an electromechanically actuated system called EMPAct CVT. The system is using two servo motors to actuate the two movable sheaves. A double epicycloidal gear decouples the rotation of the pulley from the rotation of the servo motors. To

<sup>2</sup>This layout currently is covered by an international patent



(a) Variator efficiency as a function of the secondary clamping force



(b) Variator efficiency as a function of the slip

Figure 2.6: Dependence of variator efficiency on the secondary clamping force and slip value

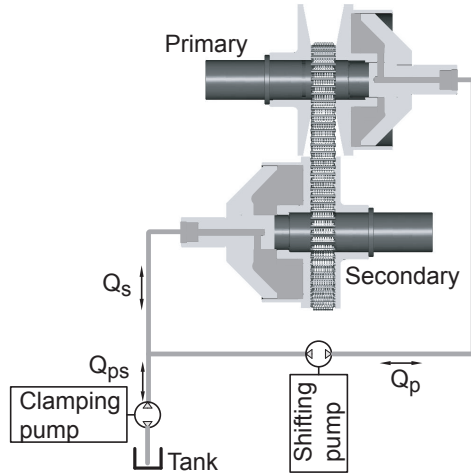


Figure 2.7: Servo pump hydraulic system used to generate the necessary pulleys pressures

optimize even more the efficiency of the system, the slip of the variator is controlled. Compared to conventionally controlled variators, the efficiency was increased up to 20% and up to 10% compared to an optimally slip controlled variator.

### Hydraulic optimization

Faust et al. (2002) propose to reduce the pump size by using a double piston that permits to reduce the hydraulic pressure. They also proposed to optimize the leakage of the variator. Kurosawa & Okahara (2007) propose to use a variable flow oil pump and to optimize the hydraulic control valves.

## 2.5 System used in this thesis

Section 2.4 discussed different approaches to improve the efficiency of the variator in order to reduce the fuel consumption. Instead of the metallic belt, the Involute Chain is chosen. The hydraulic system using valves is replaced by the servo pump actuator system presented in *Section 2.4.2*. Using the chain speed, a new slip synthesis (introduced in this work) will be applied to slip control to reduce the clamping forces and improve the efficiency of the variator.

## 2.6 Summary

The continuously variable transmission type belt or chain were discussed in this chapter. The variator has two pulleys. Each pulley is composed of one fixed conical sheave and a second conical sheave movable in its axial direction

under external forces, usually hydraulic. A metallic belt or a chain is clamped by the pulleys and transmits the power from the primary to the secondary pulley.

The efficiency of the variator is influenced by three main factors: losses due to slip, hydraulic pump losses and finally the belt-related torque losses. Losses due to slip come from the difference of speed between the pulley sheave and the intermediate element. Pump losses are due to the over dimension of the hydraulic pump and the pressure hydraulics. The belt-related torque losses come from the behavior of the metallic belt at the entry and exit of the pulley. Different strategies improving the efficiency were discussed, as for example changing the hydraulic actuation by an electromechanical actuation, or reducing the clamping force by controlling the slip.

A new slip synthesis of the variator is introduced in the next chapter.





## Chapter 3

# New slip synthesis

Slip in the variator plays an important role. First, slip can damage the pulley sheaves and the intermediate element; furthermore can destabilize the system. Therefore, operating limits are important to know. This chapter discusses slip and the relation between slip and traction coefficient for each pulley to obtain a new total slip synthesis of the variator.

This chapter is structured as follows. The first section describes the slip behavior of each pulley. Analyzing this slip, a new total slip synthesis is introduced in the second section. The third section defines the relation between slip and traction coefficient for each pulley. The fourth section compares the new synthesis with the usual one used in the literature. Finally, the two last sections define the efficiency of the variator and the stability of the system, respectively.

### 3.1 Pulley slip

Slip is linked to the power transmission of the variator, which relies on friction between the intermediate element and the pulley sheaves. The slip behavior is different for each pulley as shown in Figure 3.1 which shows experimental measurements of speed and clamping force in the variator for different speed ratios. During these experiments, the geometrical ratio is fixed geometrically <sup>1</sup> i.e the primary radius is constant, the primary speed and the secondary clamping force are constant while the resisting torque is rising.

Figure 3.1(a) shows the tangential speed of the pulleys, the chain speed and the clamping forces of each pulley in UD ratio . As the secondary clamping force is constant and the load rises, the slip of the variator increases. Until a certain limit value of the load, the chain speed is constant and the secondary pulley velocity goes down i.e. slip occurs on the secondary pulley. When the load exceeds this limit value, the chain velocity and the secondary pulley speed decrease i.e. the primary pulley starts to slip and the secondary slip remains constant, finally the system becomes unstable. Note that the primary clamping force is smaller than the secondary clamping force. Figure 3.1(b)

---

<sup>1</sup>The axial position of the primary pulley is measured and controlled to stay constant

shows the same experiments for a ratio smaller than one. It can be seen that the slip occurs only on the secondary pulley and the secondary clamping force is smaller than the primary clamping force. From these experiments, it can be concluded that the critical pulley (the pulley that will reach the macro slip, i.e. instability) is the pulley with the smallest clamping force i.e. the pulley with the highest friction coefficient. In low ratio, macro slip occurs on the primary pulley and in middle or higher ratios, macro slip occurs on the secondary pulley.

With these results, a different slip value and traction coefficient can be expected for each pulley and finally obtain a new synthesis of the total slip.

### 3.2 New analysis of the total slip

A speed loss  $v_x$ <sup>2</sup> between each pulley and the intermediate element can be defined by the difference of the tangential pulley speed at the contact radius  $R_x$  and the velocity of the chain  $v_{ch}$  (Yamaguchi et al. (2006)).

$$v_p = \omega_p R_p - v_{ch} \quad (3.1)$$

$$v_s = v_{ch} - \omega_s R_s \quad (3.2)$$

Using the speed loss terminology, the dimensionless relative slip of each pulley  $s_x$  is defined to describe the relative motion between each pulley and the intermediate element:

$$s_p = \frac{v_p}{\omega_p R_p} = 1 - \frac{v_{ch}}{\omega_p R_p} \quad (3.3)$$

$$s_s = \frac{v_s}{\omega_s R_s} = \frac{v_{ch}}{\omega_s R_s} - 1 \quad (3.4)$$

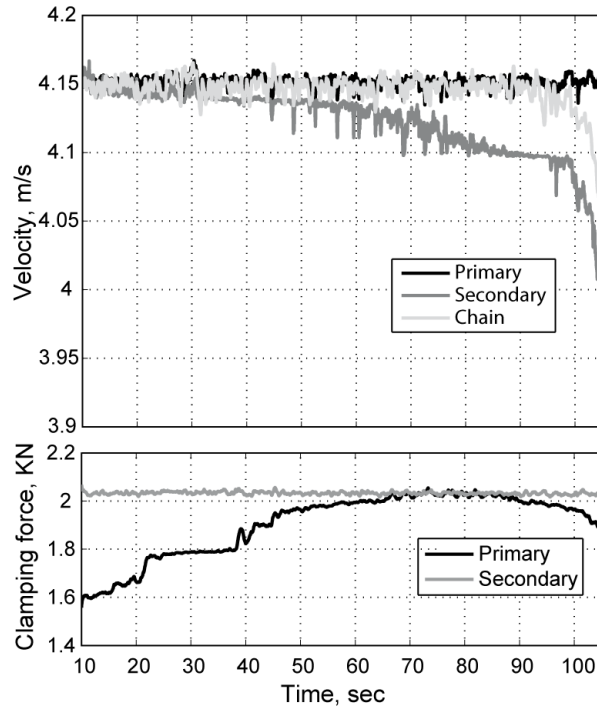
The slip of each pulley is then used to estimate the total slip of the variator as the sum of the primary and the secondary slip. This new synthesis of the total slip is discussed in more detail in *Section 3.4*.

$$\begin{aligned} s_{tot} &= s_p + s_s \\ &= v_{ch} \left( \frac{1}{\omega_s R_s} - \frac{1}{\omega_p R_p} \right) \end{aligned} \quad (3.5)$$

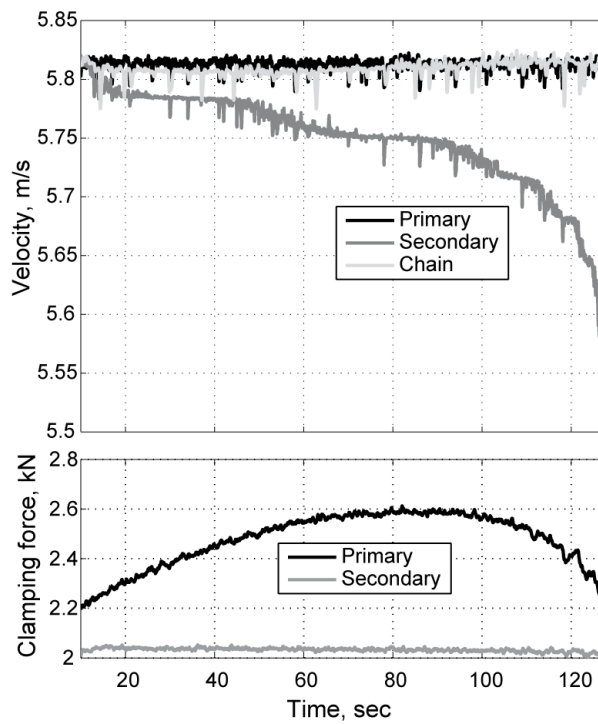
By means of the logarithmic derivation with respect to time and by re-arranging terms, the differential equation of the primary and the secondary slip,  $\dot{s}_p$  and  $\dot{s}_s$  respectively, are derived as a function of variator geometric and kinematic parameters (Appendix A) .

---

<sup>2</sup> $x = p$  for primary pulley,  $x = s$  for secondary pulley



(a)  $r_{cvt,g} = 0.49, R_p = 39.67mm, R_s = 80.94mm$



(b)  $r_{cvt,g} = 0.835, R_p = 55.53mm, R_s = 66.54mm$

Figure 3.1: Tangential pulleys speed, chain speed and the pulley clamping forces during slip measurements for different geometrical ratio

$$\dot{s}_p = \frac{1-s_p}{\omega_p} \dot{\omega}_p + \frac{1-s_p}{R_p} \dot{R}_p - \frac{1}{\omega_p R_p} \dot{v}_{ch} \quad (3.6)$$

$$\dot{s}_s = -\frac{1+s_s}{\omega_s} \dot{\omega}_s - \frac{1+s_s}{R_s} \dot{R}_s + \frac{1}{\omega_s R_s} \dot{v}_{ch} \quad (3.7)$$

The first term in the two equations corresponds to pulley dynamics, whereas the second term is due to change in pulley radius (geometrical ratio) and finally the third term is due to the dynamics of the intermediate element.

The total slip dynamics is now defined by:

$$\begin{aligned} \dot{s}_{tot} &= \dot{s}_p + \dot{s}_s \\ &= \frac{1-s_p}{\omega_p} \dot{\omega}_p - \frac{1+s_s}{\omega_s} \dot{\omega}_s + \frac{1-s_p}{R_p} \dot{R}_p - \frac{1+s_s}{R_s} \dot{R}_s + \\ &\quad \left( \frac{1}{\omega_s R_s} - \frac{1}{\omega_p R_p} \right) \dot{v}_{ch} \end{aligned} \quad (3.8)$$

$$= \frac{1-s_p}{\omega_p} \dot{\omega}_p - \frac{1+s_s}{\omega_s} \dot{\omega}_s + \frac{1-s_p}{R_p} \dot{R}_p - \frac{1+s_s}{R_s} \dot{R}_s + \overbrace{\frac{s_p+s_s}{v_{ch}}}^s \dot{v}_{ch} \quad (3.9)$$

A traction curve can now be defined as a function of each pulley slip  $s_x$ .

### 3.3 Traction coefficients

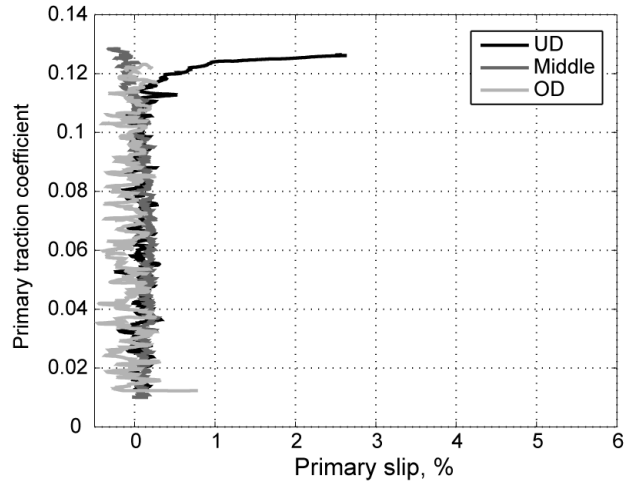
The traction coefficient  $\mu_x$  is the equivalent friction coefficient of the considered pulley and is defined by:

$$\mu_x(r_{cvt,g}, F_s, s_x) = \frac{\cos \beta_0}{2R_x} \frac{T_x}{F_x} \quad (3.10)$$

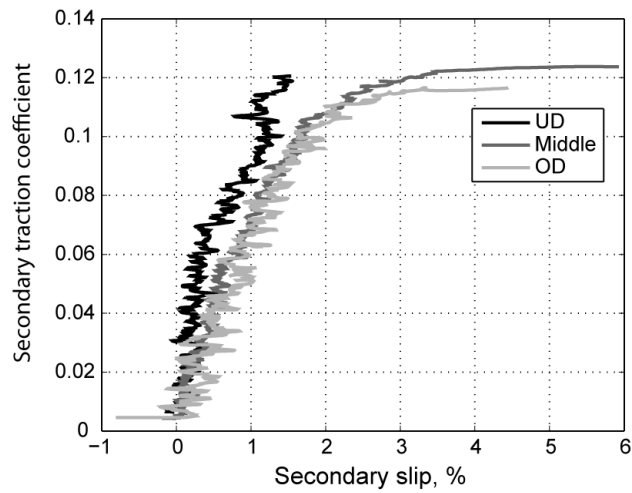
where  $R_x$  is the pulley radius,  $T_x$  is the pulley torque,  $F_x$  is the pulley clamping force and finally  $\beta_0$  is the non-deformed half angle of the pulley.

Figure 3.2(a) and Figure 3.2(b) show the measured primary and the secondary traction coefficients respectively as a function of slip for different geometrical ratios. As expected, the traction curve of each pulley strongly depends on the geometrical ratio and is different for each pulley. Also, these experiments show that the intermediate element does not slip on the primary pulley except for low ratios.

As it can be seen in Figure B.2, clamping force amplitude slightly affects the traction coefficient. The rotation speed of the pulleys does not affect the traction coefficient (Figure B.3).



(a) Primary traction coefficient as a function of the slip for different ratio



(b) Secondary traction coefficient as a function of the slip for different ratio

Figure 3.2: Primary (a) and secondary (b) traction coefficients as a function of slip for different geometrical ratio

### 3.3.1 Micro and macro slip definition

As evidenced by the previous figures, the traction coefficient increases with slip until it reaches a maximum and then remains constant or slightly decreases. For small amounts of slip, the traction coefficient is almost linear with slip. This part of the curve with viscous behavior is called the micro-slip area. The macro-slip area is defined as the region where the traction coefficient decreases with increasing slip (Figure 3.3).

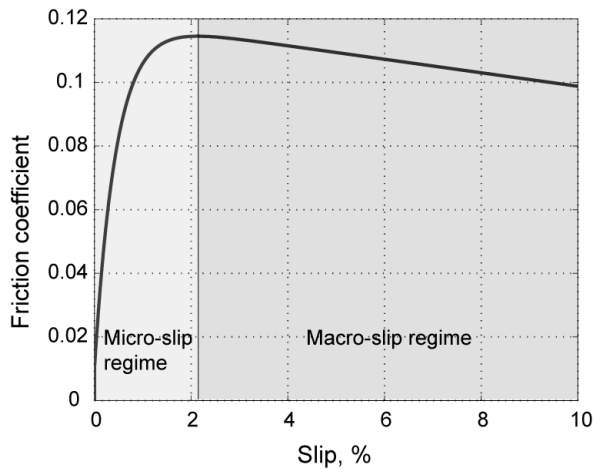


Figure 3.3: Definition of micro and macro slip: positive slope is define as the micro-slip, negative slope is define as the macro-slip

It can be expected to have different behavior of the system with a positive or a negative slope of the traction coefficient. This phenomenon will be analyzed in *Section 3.6* using a simple model.

## 3.4 Discussion of new slip synthesis

The new synthesis of the total slip defined in *Section 3.2* is discussed and compared with the synthesis used by several authors (from now on called standard synthesis) (Kobayashi et al. (1998); Veenhuizen et al. (2002); van Drogen & van der Laan (2004); van der Laan et al. (2004); Metsenaere et al. (2005); Pulles et al. (2005); van Eersel (2005); Bonsen (2006)).

### 3.4.1 Standard slip synthesis

#### Slip

The standard slip synthesis  $s_{sd}$  is a global measure of slip. This synthesis considers a speed loss  $v_{sd}$  in the variator, defined by the difference tangential speeds between the primary and the secondary pulleys.

$$v_{sd} = \omega_p R_p - \omega_s R_s \quad (3.11)$$

The relative slip is defined as the speed loss divided by the input speed  $\omega_p R_p$  and is thus expressed as

$$s_{sd} = \frac{v_s}{\omega_p R_p} = 1 - \frac{\omega_s R_s}{\omega_p R_p} = 1 - \frac{r_{cvt}}{r_{cvt,g}} \quad (3.12)$$

where  $r_{cvt} = \frac{\omega_s}{\omega_p}$  is the speed ratio and  $r_{cvt,g} = \frac{R_p}{R_s}$  is the geometrical ratio.

### Differential equation

The rate of change of the standard slip  $\dot{s}_{sd}$  is obtained by the time derivation of (3.12). Considering the geometric and speed ratio dynamics (Simons (2006)), the resulting differential equation can be written as (Appendix E):

$$\dot{s}_{sd} = \frac{1 - s_{sd}}{\omega_p} \dot{\omega}_p - \frac{1 - s_{sd}}{\omega_s} \dot{\omega}_s + \frac{1 - s_{sd}}{R_p} \dot{R}_p - \frac{1 - s_{sd}}{R_s} \dot{R}_s \quad (3.13)$$

The first and the second term of the equation represent the dynamics of the primary and the secondary pulley respectively, the last two terms are due to the change in the geometrical ratio.

### Traction coefficient

The standard synthesis introduces an effective traction coefficient of the variator  $\mu_{sd}$  defined as the transmitted output torque divided by the normal component of the contact force between the intermediate element and the pulley subjected to the smaller of the two clamping forces (Bonsen (2006)).

$$\mu_{sd}(s_{sd}) = \frac{\cos \beta_0}{2} \frac{T_s}{\min(F_p, F_s) R_s} = \frac{\cos \beta_0}{2} \frac{T_p}{\min(F_p, F_s) R_p} \quad (3.14)$$

### 3.4.2 New slip synthesis

#### Slip

The new slip synthesis was defined by (3.5). Taking into account (3.3) and (3.4) and rearranging terms, (3.5) yields

$$\begin{aligned} s_{tot} &= \frac{v_{ch}}{\omega_s R_s} \left( \frac{1}{\omega_s R_s} - \frac{1}{\omega_p R_p} \right) \\ &= \frac{v_{ch}}{\omega_s R_s} \left( 1 - \frac{r_{cvt}}{r_{cvt,g}} \right) \end{aligned} \quad (3.15)$$

Where the term  $1 - \frac{r_{cvt}}{r_{cvt,g}}$  is the standard slip synthesis (3.12).

### Differential equations

The rate of change of slip for the new slip synthesis was derived in *Section 3.2*:

$$\begin{aligned}\dot{s}_{tot} &= \dot{s}_p + \dot{s}_s \\ &= \frac{1 - s_p}{\omega_p} \dot{\omega}_p - \frac{1 + s_s}{\omega_s} \dot{\omega}_s + \frac{1 - s_p}{R_p} \dot{R}_p - \frac{1 + s_s}{R_s} \dot{R}_s \\ &\quad + \frac{s_p + s_s}{v_{ch}} \dot{v}_{ch}\end{aligned}\quad (3.16)$$

Compared to the standard slip (3.13), the last term in (3.16) is added, since the intermediate element dynamics is considered in the new synthesis.

### Traction coefficient

As shown in *Section 3.3*, the new synthesis defines an effective traction coefficient  $\mu_x$  for each pulley.

$$\mu_p(s_p) = \frac{\cos \beta_0}{2} \frac{T_p}{F_p R_p} \quad (3.17)$$

$$\mu_s(s_s) = \frac{\cos \beta_0}{2} \frac{T_s}{F_s R_s} \quad (3.18)$$

### 3.4.3 Comparison of the two synthesis

Taking into account the secondary slip (3.4), we can rewrite (3.15) as:

$$\begin{aligned}s_{tot} &= \frac{v_{ch}}{\omega_s R_s} \left( 1 - \frac{r_{cvt}}{r_{cvt,g}} \right) \\ &= (1 + s_s) \left( 1 - \frac{r_{cvt}}{r_{cvt,g}} \right)\end{aligned}\quad (3.19)$$

For small values of slip i.e.  $s_s \ll 1$ , (3.19) coincides with the standard slip definition:

$$s_{tot} \approx 1 - \frac{r_{cvt}}{r_{cvt,g}} = s_{sd} \quad (3.20)$$

For low secondary slip values, the two syntheses are equivalent. In contrast, for high secondary slip values, the two approaches differ. In usual CVT use, slip is small and the two syntheses can be considered as equivalent. This equivalence introduces some questions: what are the differences between the two slip syntheses ? What are the advantages of the new one ?



The standard synthesis of slip defines slip and traction coefficient from a global point of view. Slip is defined by the difference of the tangential speed of the two pulleys (3.11) and the dynamics of the intermediate element is not considered. Slip on each pulley is unknown.

In contrast with the standard synthesis, the new one analyzes slip in more details by looking at the difference in tangential speed between each pulley and the intermediate element to define the total slip of the variator. Also, a traction curve for each pulley is defined. *Section 3.3* indicates that the traction curve is different for the primary and the secondary pulley. The new synthesis gives more information on the CVT state: slip on each pulley is well known. These new informations may open the way to a new CVT control strategy.

The intermediate element dynamics is an additional dynamics introduced by the new slip synthesis. The four first terms of the differential equation of the new slip synthesis (3.16) are identical to the terms in the standard one (3.13). The last term of the new synthesis stands the added dynamics. This additional dynamics is helpful for improving the model of slip and its control.

Compared to the standard slip synthesis, the new one needs additional information such as the speed of the intermediate element.

#### 3.4.4 Remark

Figure 3.4 shows the measured total slip and the slip at each pulley in UD and middle ratio for a constant load and speed ratio, while the total slip varied. These experiments clearly demonstrate that in UD or low ratio, not only the secondary pulley slips but also the primary. In middle or higher ratio, only the secondary pulley slips.

### 3.5 Efficiency

The efficiency of the variator  $\eta_{var}$  is given by the ratio of the output and the input power of the transmission.

$$\eta_{var} = \frac{\omega_s T_s}{\omega_p T_p} \quad (3.21)$$

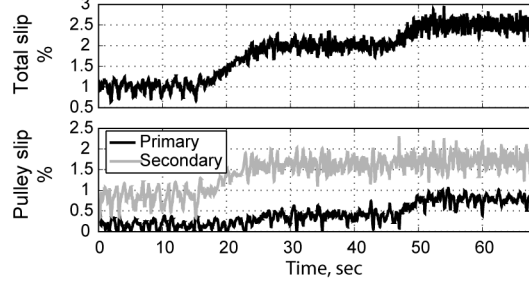
Where  $\omega_p$  and  $\omega_s$  are the primary and the secondary pulley speed respectively,  $T_x$  the pulley torques.

Figure 3.5 shows the efficiency for different configurations of the geometrical ratio, clamping forces and primary rotation speed. An optimum is observed and is slightly affected by the different configurations.

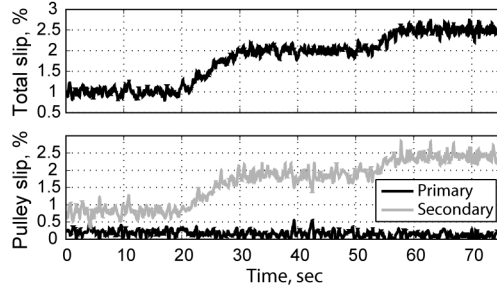
If the losses of the system are considered, the secondary torque  $T_s$  and the secondary pulley speed  $\omega_s$  are expressed as

$$T_s = \frac{T_p}{r_{cvt,g}} - T_{loss} \quad (3.22)$$

$$\omega_s = \omega_p r_{cvt,g} - \omega_{loss} \quad (3.23)$$



(a) Underdrive ratio



(b) Middle ratio

Figure 3.4: Total slip and pulley slip in underdrive and middle ratio

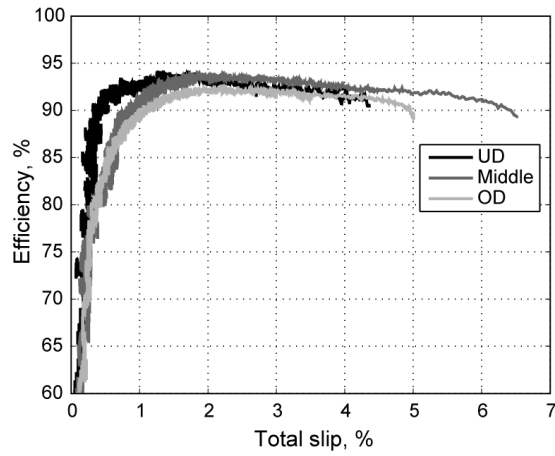
where  $T_{loss}$  is the torque losses and  $\omega_{loss}$  is the speed losses. Bearing losses, which depend on the rotation speed and load, the belt-related torque loss (*Section 2.3.3*), the miss-alignment of the intermediate element and the friction between each part of the belt generate torque losses. The slip between the intermediate element and the pulley sheave, in the case of the metallic belt the speed difference between each band and block constitute the speed losses of the variator.

Introducing equations, (3.21) yields to:

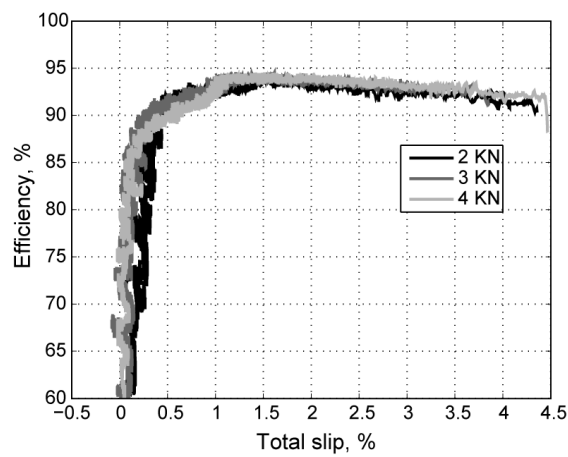
$$\begin{aligned} \eta_{var} &= \left(1 - \frac{r_{cvt,g} T_{loss}}{T_p}\right) (1 - s) \\ &= \eta_T \eta_s \end{aligned} \quad (3.24)$$

Where the first right term is equivalent to the torque efficiency  $\eta_T$  and the second right term is equivalent to the slip efficiency  $\eta_s$ .

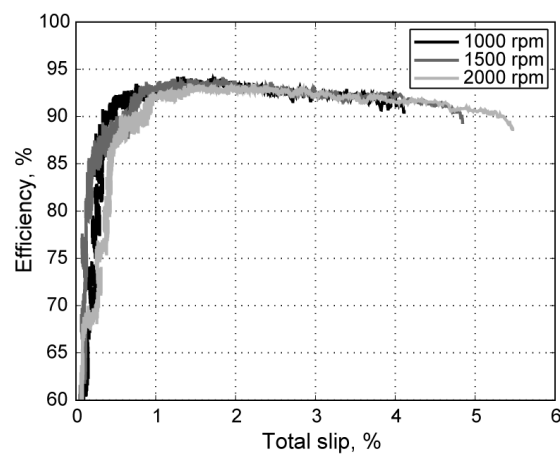
Figure 3.6(a) and Figure 3.6(b) represent total, torque and slip efficiencies ( $\eta_{var}$ ,  $\eta_T$  and  $\eta_s$  respectively) as a function of total slip  $s_{tot}$  and as a function of the input torque  $T_p$  respectively. Figure 3.6(c) depicts the torque loss as a function of slip. During those experiments, the secondary clamping force and geometrical ratio were held constant, while the input torque was allowed to rise. Because the secondary clamping force is constant, slip augments with torque.



(a) Variator efficiency as a function of total slip for different geometrical ratios



(b) Variator efficiency as a function of total slip for different secondary clamping forces



(c) Variator efficiency as a function of total slip for different primary rotation speeds

Figure 3.5: Summary of the variator efficiency as a function of slip

Figure 3.6(b) shows that the slip efficiency decreases linearly and then drops precipitously. When the torque reaches the maximum transmissible value, the system reaches the macro-slip regime. At this point the system becomes unstable. Using a simple model, we explain this instability in the next section.

Figure 3.6(c) depicts that the torque loss is only slightly dependent on slip or input torque but strongly depends on speed ratio.

### 3.6 Stability analysis with a simple model

*Section 3.3.1*, discussed that the traction curve has a portion with a positive and a portion with a negative slope. The positive slope defines the micro-slip regime and the negative slope the macro-slip regime. We will demonstrate that the negative sign of the slope indicates instability to the system.

Let us consider the simple model shown in Figure 3.7. *BodyI* is considered to be one of the pulley. It rotates at a constant velocity  $\omega$ . A force  $F_1$  is applied to it. *BodyII* is equivalent to the intermediate element and moves in  $e_y$  direction. A force  $F_2$  is applied to this body.

The dynamics of *BodyII* in the vertical direction are described by :

$$\begin{aligned} M\dot{v} &= F_{fr} - F_2 \\ &= F_1\mu(s) - F_2 \end{aligned} \quad (3.25)$$

Where  $\mu(s)$  is the traction coefficient and is a function of the slip  $s$ ,  $M$  is the mass of *BodyII*.

The slip  $s$  is defined by:

$$s = \frac{\omega R - v}{\omega R} \quad (3.26)$$

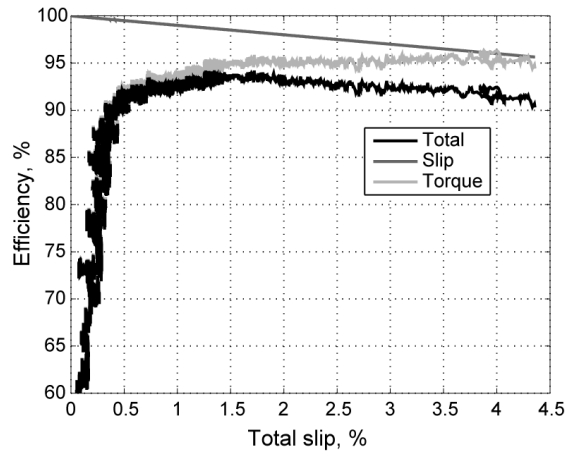
By means of a logarithmic derivation with respect to time and by rearranging terms, the rate of change of the slip becomes

$$\dot{s} = -\frac{1}{\omega RM} (F_1\mu(s) - F_2) \quad (3.27)$$

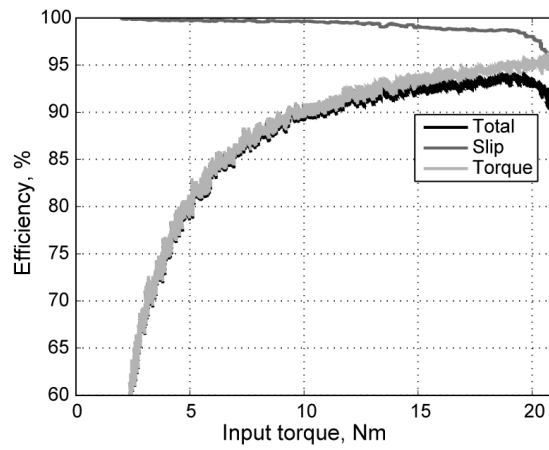
Defining the state  $x = s$ , the input  $u = F_1$ , the output  $y = x = s$  and linearizing around a working point  $x_0 = s_0$ , the state-space formulation of the dynamics of *BodyII* becomes

$$\begin{aligned} \dot{x} &= Ax + Bu \\ y &= Cx \end{aligned} \quad (3.28)$$

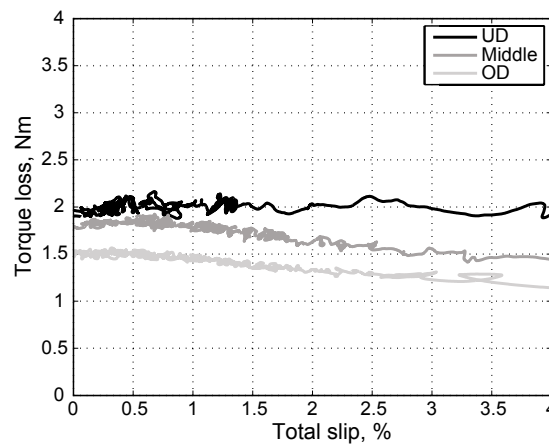
with



(a) Total slip and torque efficiencies as a function of total slip



(b) Total slip and torque efficiencies as a function of input torque



(c) Torque losses as a function of total slip

Figure 3.6: Summary of the different losses present in the variator type belt or chain

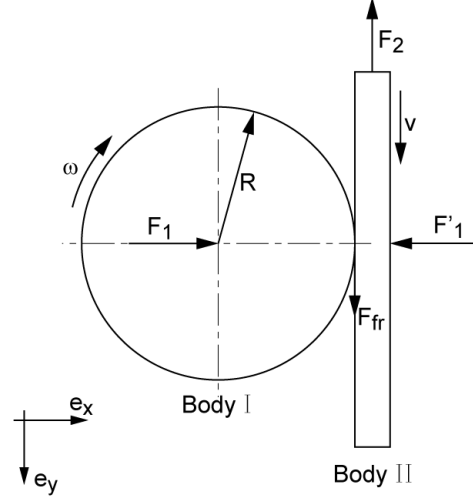


Figure 3.7: Simple model of the chain in contact with the pulley used for stability study

$$A = -\frac{F_{1,0}}{\omega R} \frac{d\mu}{ds} \Big|_0 \quad (3.29)$$

$$B = -\frac{\mu_0}{\omega R M} \quad (3.30)$$

$$C = 1 \quad (3.31)$$

The stability of the system is given by the sign of the constant  $A$ . The system is stable if and only if  $A \leq 0$ . Except for the term  $\frac{d\mu}{ds}$ , all the terms are positive, therefore, the stability is directly defined by the sign of  $\frac{d\mu}{ds}$  i.e. the slope of the traction coefficient. If the slope is positive, then  $A$  is negative ( $A < 0$ ) and the system is stable. If the slope is negative,  $A$  becomes positive and the system is unstable.

As expected, the slope of the traction curve defines the stability of the variator and should be positive (micro-slip) to guarantee the stability of the system.

### 3.7 Summary

Slip of each pulley of the CVT variator and the relation between traction coefficient and slip were discussed in this chapter. During the measurements of the traction curve, the geometrical ratio and the secondary clamping force are constant while the load rises. In UD configuration, the secondary pulley slips until a certain value of the applied load is reached. When this limit is exceeded, the primary pulley slips and reaches macro-slip. In middle or higher ratio, only the secondary pulley slips and reaches macro-slip. Using these results, a new synthesis of the total slip, given as the sum of the primary

and the secondary slip, is proposed. Also, a traction curve can be defined for each pulley. This new definition introduced new dynamics considerations as the intermediate element dynamics.

Micro and macro slip regimes were defined in terms of the sign of slope of the traction curve. During micro-slip, the slope is positive; macro-slip is defined by the negative slope. Using a simple model, it was demonstrated that if the slope is negative the system is unstable.

The next chapter gives the calculation of the clamping forces, the traction coefficient, the slip and the efficiency of the variator taking into account the elastic deformation of the different elements.





## Chapter 4

# Low level model

The kinematics and forces involved in the CVT variator must be described in detail in order to understand the entire system. Especially, the primary and the secondary clamping force, the traction coefficient and the slip on each pulley are of interest in this chapter.

The low level model approach presented here tries to provide the best mathematical representation of the variator. This model will give a good understanding of the system and the results will be used in the high level model described in *Chapter 5*.

The chapter is structured as follows. Firstly, the state of the art in modeling CVTs is presented, followed by the geometry of the variator. Then, the kinematics and forces involved in the system are developed. Elastic deformations of the pulley and the chain are discussed. After a description of how to solve the modeling problem is given, the chain efficiency is estimated by means of the losses at each contact point is provided. Finally, some simulations results using the low level model are presented.

### 4.1 State of the art

A lot of models can be found for the CVT metallic belt, but only few models for CVT chain.

For example, Asayama et al. (1995) and Kobayashi et al. (1998) propose models for the metallic belt. In their models, all bodies are rigid and they take into account the action of the bands. As other authors, Tarutani et al. (2006) consider band interactions and augment the model by taking into account pulley deformations. These pulley deformations are determined using finite element method (FEM) calculation. Poll & Meyer (2007) do not only consider pulley deformations, but also bending of the shafts.

Sorge (1996) considers pulley deformations and uses the virtual displacement approach to solve the problem of the metallic belt trajectory, clamping forces and slip. More recently, he studied the shift mechanics of the metallic belt including belt deformations (Sorge (2007)).

Carbone et al. (2001) developed a theoretical model of a metal pushing

V-belt to understand the CVT transient dynamics during rapid speed ratio variations. Carbone et al. (2003) used two friction models, namely a Coulomb friction and a visco-plastic friction to model friction between the belt and pulley. Later Carbone et al. (2005) extended their previous work Carbone et al. (2001) to investigate the influence of pulley deformation on the shifting mechanism of a metal V-belt CVT. In this model the belt is considered as continuous, but the model can also be used for CVT chain (Carbone et al. (2006)). This model uses the Sattler model (Sattler (1999)) to describe pulley deformations. Sattler describes the deformations of the radius using trigonometric relations. This model contains a parameter equivalent to pulley stiffness. Using FEM calculation, Sferra et al. (2002) propose a mathematical relation for this parameter.

Kanokogi & Hashino (2000) present a multi-body model of the metallic belt using a multi-body software simulation called ADAMS. Each component of the metallic belt are rigid or flexible bodies. The results obtained are claimed to be similar to the experiments. However, the simulation is time consuming because of the large number of degrees of freedom.

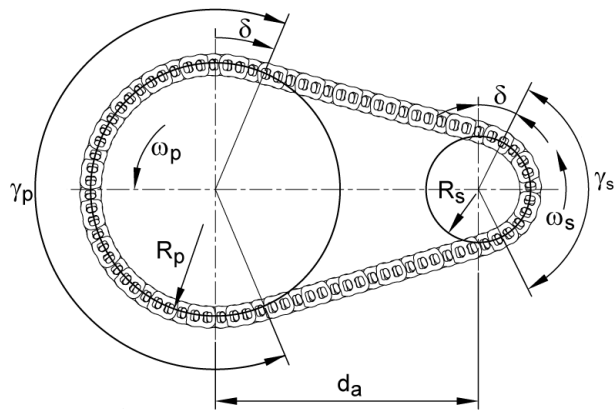
Srnik (1998) and Tenberge (2004) describe models of CVT chains. Srnik has developed a multi body dynamics model of a chain. This model takes into account not only pulley deformations but also links and pins deformations. Tenberge's model is using a pseudo multi body model by considering the equilibrium of the forces in steady-state. This model considers only the pulley deformations. Srivastava & Haque (2007) augment the Srnik model by including clearances to see their effect on the dynamic performances.

Several authors used the classical Coulomb friction law to describe friction between the intermediate element and the pulley sheaves. Only a few such as Srnik (1998), Yamaguchi et al. (2006), Srivastava et al. (2006), Poll et al. (2006) use an exponential law. Micklem et al. (1994b) suggest that a viscous model is more appropriate to describe slip and develop an empirical relation based on elastohydrodynamic lubrication (EHL) theory. Recently, Carbone et al. (2008) analyze in detail the EHL squeeze process with a non-Newtonian rheology of the lubricant and the visco-elastic response. It was concluded that the lubricant may not be able to avoid direct asperity contact between the two surfaces i.e direct metal-metal contact.

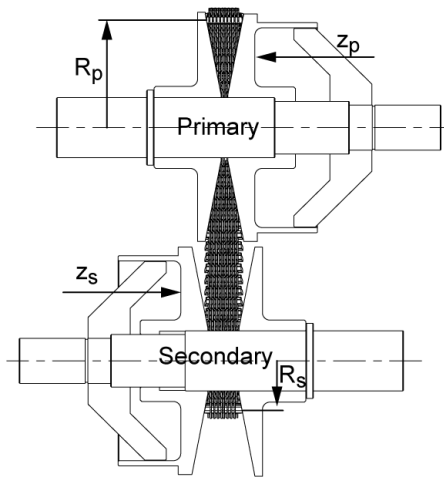
## 4.2 Geometric model of the variator

Figure 4.1 shows the geometry of the variator.  $\omega_x$  is the pulley velocity,  $R_x$  is the pulley radius,  $d_a$  is the distance between pulley centers and finally  $\gamma_x$  is the wrapped angle.

The two pulley speed ratios and the two pulley radius ratios define the speed ratio  $r_{cvt}$  and the geometrical ratio  $r_{cvt,g}$  respectively:



(a) Frontal view of the variator



(b) Over view of the variator

Figure 4.1: Frontal and over view of the variator

$$r_{cvt} = \frac{\omega_s}{\omega_p} \quad (4.1)$$

$$r_{cvt,g} = \frac{R_p}{R_s} \quad (4.2)$$

The ratio is lower bounded by the underdrive ratio and upper boundary by the overdrive ratio.

The geometrical ratio  $r_{cvt,g}$  considers the following assumptions: the chain does not slip, the pulleys and the intermediate element do not deform, the chain runs at a perfect radius and the intermediate element length is constant.

With these assumptions and the geometry of the variator (Figure 4.1(a)) the length of the intermediate element  $L_{ch}$  yields:

$$\delta = \arcsin\left(\frac{R_s - R_p}{d_a}\right) \quad (4.3)$$

$$L_{ch} = 2\delta(R_s - R_p) + \pi(R_s + R_p) + 2d_a \cos \delta \quad (4.4)$$

Solving numerically the equation, the primary and the secondary radius,  $R_p$  and  $R_s$  respectively, are determined as a function of the geometrical ratio  $r_{cvt,g}$  as shown in Figure 4.2. A polynomial of degree three approximates the two radiuses.

$$R_x = a_{3,x}r_{cvt,g}^3 + a_{2,x}r_{cvt,g}^2 + a_{1,x}r_{cvt,g} + a_{0,x} \quad (4.5)$$

$$\frac{dR_x}{dr_{cvt,g}} = 3a_{3,x}r_{cvt,g}^2 + 2a_{2,x}r_{cvt,g} + a_{1,x} \quad (4.6)$$

Furthermore, the axial position of the primary and secondary movable pulleys is give by:

$$z_x = (R_x - R_{min,x}) \tan \beta_0 \quad (4.7)$$

where  $R_{min,x}$  is the minimum radius of the pulley,  $\beta_0$  is the half angle of the non deformed pulley.

The axial speed of the movable pulley is then given by:

$$\dot{z}_x = \frac{dR_x}{dt} \tan \beta_0 \quad (4.8)$$

Using the rate of the geometrical ratio change  $\dot{r}_{cvt,g}$ , the term  $\frac{dR_x}{dt}$  becomes

$$\begin{aligned} \frac{dR_x}{dt} &= \frac{dR_x}{dr_{cvt,g}} \frac{dr_{cvt,g}}{dt} \\ &= \frac{dR_x}{dr_{cvt,g}} \dot{r}_{cvt,g} \end{aligned} \quad (4.9)$$

Where  $\frac{dR_x}{dr_{cvt,g}}$  is given by (4.6)

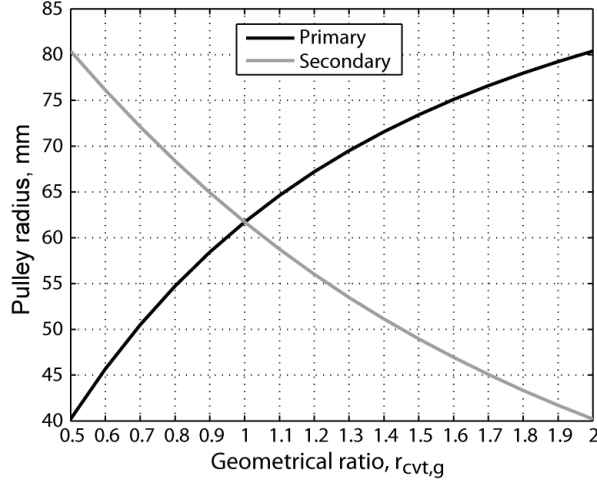


Figure 4.2: Primary and secondary pulley radius as a function of the geometrical ratio  $r_{cvt,g} = R_p/R_s$

### 4.3 Steady-state model of the variator

As it was previously discussed (*Section 4.1*), different models have been developed to determine the clamping forces or the belt tension. Some models take into account elastic deformations of the belt and pulleys. These deformations are important for the efficiency and slip calculations. These stationary models calculate the force distribution by considering the variator in equilibrium.

The steady state model presented in this section considers elastic deformations of pulleys, the longitudinal and transversal elastic deformations of the intermediate element and contact point deformations.

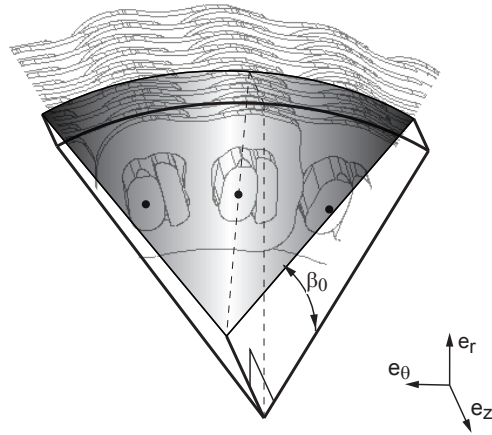
#### 4.3.1 Kinematic model

Figure 4.3 show the 3D and the planar view of kinematic quantities involved in the system.  $\theta$  is the angular position of the pin when it is clamped into the pulley,  $v_s$  is the sliding velocity between the pulley sheave and the chain pin,  $\psi$  is the sliding angle and  $r$  is the pulley radius.

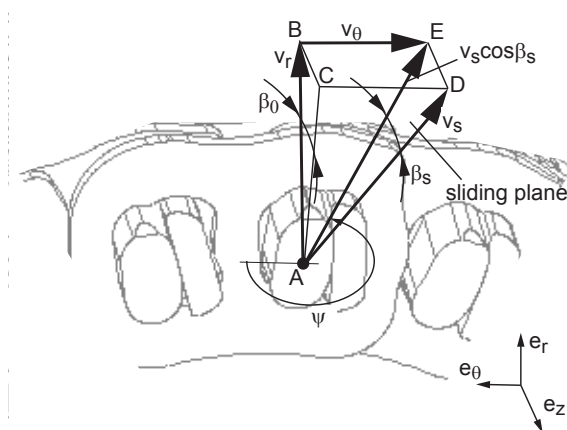
The plane ADE in the 3D view (Figure 4.3(b)) is the sliding plane where the chain slides on the pulley sheave with a slip velocity  $v_s$ . The chain moves tangentially and radially in the pulley groove. The planes ABE and ABC are the rotational plane and the pulley wedging angle respectively. The angle  $\beta_s$  represents the pulley wedging-angle in the sliding plane of the chain.

The velocity  $v_s \cos \beta_s$  is the sliding velocity projected onto the vertical plan and decomposed in radial sliding  $v_r$  and in tangential sliding  $v_\theta$ . The angle  $\beta_s$  corresponds to the half angle of the sliding plane.

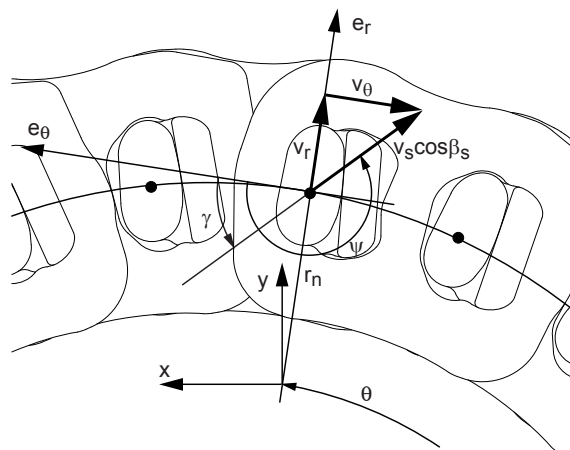
Using geometric relations, the half opening angle of the sliding plane is given by



(a) General 3D view of the chain in contact with the pulley sheave



(b) 3D view zoom around the contact point when the chain is in contact with the pulley sheave



(c) Planar view

Figure 4.3: General 3D view and planar view of the chain is in contact with the pulley sheave

$$\tan \beta_s = \tan \beta \sin \gamma \quad (4.10)$$

### Radial slip velocity

The radial sliding velocity  $v_r$  is equal to the summation of the radial sliding velocity  $\dot{R}$  due to the shifting ratio and the sliding velocity due to the elastic deformations  $\dot{r} = \frac{dr}{dt}$ . The deformed radius  $r$  is a function of the angular position  $r(\theta)$ , and  $\dot{r}$  can be written as  $\dot{r} = \frac{dr}{d\theta} \frac{d\theta}{dt}$ , where  $\frac{d\theta}{dt}$  equals the pulley angular velocity  $\omega$ . Finally, the radial slip  $v_r$  is equal to

$$v_r = \dot{R} + \frac{dr}{d\theta} \omega \quad (4.11)$$

### Tangential slip velocity

The chain velocity  $v_{ch}$  has a tangential and a radial component,  $V_\theta$  and  $V_r$  respectively (Figure 4.4). The first component is defined by the tangential pulley speed at the contact point  $\omega r$  and the tangential slip velocity between the pulley and the chain  $v_\theta$  i.e.  $V_\theta = \omega r + v_\theta$ . The second component is equal to the radial slip velocity  $v_r$  (4.11). Usually it can be assumed that the radial velocity  $V_r$  is smaller than the tangential velocity  $V_\theta$  i.e.  $V_r \ll V_\theta$ . The chain velocity becomes:

$$v_{ch} = \omega r + v_\theta \quad (4.12)$$

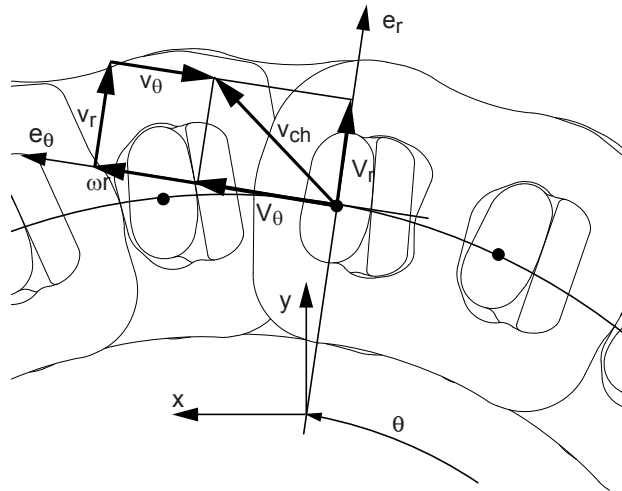


Figure 4.4: Speed component involve in the system when the chain is in contact with the pulley sheave

Due to chain elongation, the chain speed is not constant along the pulley. Considering the longitudinal strain of the chain  $\epsilon_{ch}$  and the velocity of the non deformed chain  $v_{ch,0}$ , the chain velocity is expressed as

$$v_{ch} = v_{ch,0} (\epsilon_{ch} + 1) \quad (4.13)$$

$$\epsilon_{ch} = \frac{F_{ch,n}}{E_{ch} A_{ch}} \quad (4.14)$$

Considering the time derivative of (4.12) and (4.13) and rearranging terms, the tangential slip  $v_\theta$  yields

$$\frac{\partial v_\theta}{\partial \theta} = \frac{\omega r}{\epsilon_{ch} + 1} \frac{\partial \epsilon_{ch}}{\partial \theta} - v_r \quad (4.15)$$

### 4.3.2 Mechanical model

Figure 4.5(a) and Figure 4.5(b) show a transversal and respectively an axial view of the pin clamped between the two pulley sheaves. The position of each pin is given by the angle  $\theta_{n-1}$ ,  $\theta_n$  and  $\theta_{n+1}$ . The force  $N_n$  is the normal force acting on the pin  $n$ ,  $F_{ax,n}$  is the axial force and the term  $2\mu N_n \cos \beta_s$  is the friction force. The forces  $F_{ch,n-1}$  and  $F_{ch,n}$  are the chain forces acting on the pin  $n$ .

The equilibrium equations written in the referential  $e_r, e_\theta, z$  yields to:

$$0 = F_n \cos \frac{\Delta\theta_n}{2} - F_{n-1} \cos \frac{\Delta\theta_{n-1}}{2} + 2\mu N_n \cos \beta_s \cos \gamma \quad (4.16)$$

$$0 = -F_n \sin \frac{\Delta\theta_n}{2} - F_{n-1} \sin \frac{\Delta\theta_{n-1}}{2} - 2\mu N_n \cos \beta_s \sin \gamma + 2N_n \cos \beta_0 \quad (4.17)$$

$$0 = N_n \cos \beta_0 + \mu N_n \sin \beta_s - F_{ax,n} \quad (4.18)$$

Solving these three equations, the chain force  $F_{ch,n}$ , the normal force  $N_n$  and the axial force  $F_{ax,n}$  acting on the contact point can be expressed as

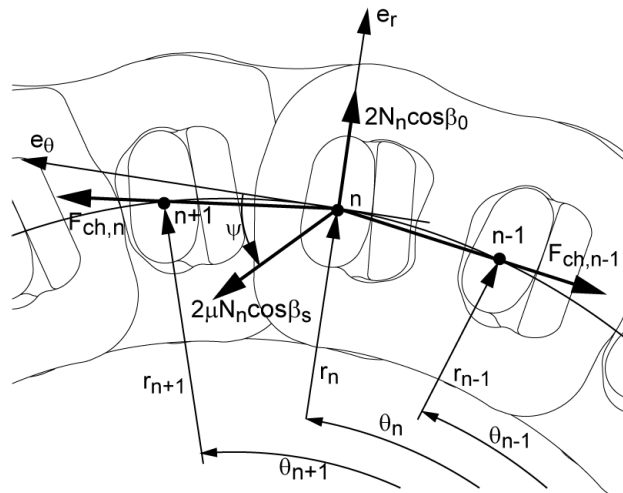
$$F_n = F_{n-1} \frac{\cos \frac{\Delta\theta_{n-1}}{2} \frac{\cos \beta_0 - \mu \cos \beta_s \cos \gamma}{\mu \cos \beta_s \cos \gamma} - \sin \frac{\Delta\theta_{n-1}}{2}}{\cos \frac{\Delta\theta_n}{2} \frac{\cos \beta_0 - \mu \cos \beta_s \cos \gamma}{\mu \cos \beta_s \cos \gamma} + \sin \frac{\Delta\theta_n}{2}} \quad (4.19)$$

$$N_n = \frac{F_{n-1} \cos \frac{\Delta\theta_{n-1}}{2} - F_n \cos \frac{\Delta\theta_n}{2}}{2\mu \cos \beta_s \cos \gamma} \quad (4.20)$$

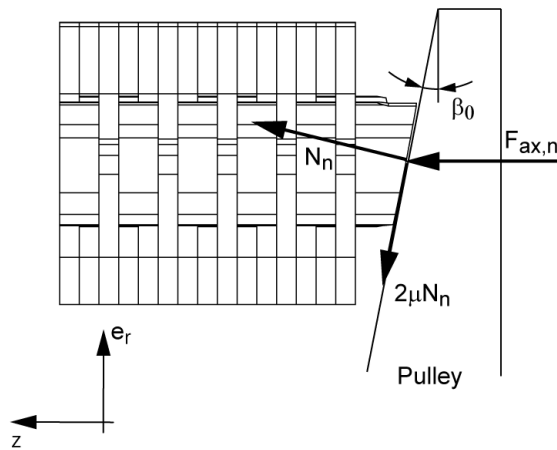
$$F_{ax,n} = F_n (\cos \beta_0 + \mu \sin \beta_s) \quad (4.21)$$

Each contact point transmit a part of the total torque by friction. The torque at the contact point is the product of the tangential friction force and the pulley radius.





(a) Frontal view



(b) Axial view

Figure 4.5: Frontal and axial view of the forces acting on the pin when it is in contact with the pulley sheave

$$\begin{aligned}
T_n &= r_n 2F_{fr} \\
&= r_n 2\mu F_n \cos \beta_s \cos \gamma
\end{aligned} \tag{4.22}$$

Finally the resultant axial force  $F_{ax}$  and torque  $T_n$  on the pulley are the summation of each axial force and torque respectively.

$$F_{ax} = \sum_n F_{ax,n} \tag{4.23}$$

$$T = \sum_n T_n \tag{4.24}$$

### 4.3.3 Friction coefficient

As mentioned in *Section 4.1*, the contact point between the intermediate element and the pulley sheave is EHL type. Calculating the thickness of the lubricating film and the resultant fluid friction are complicated tasks. Therefore, as done by some authors, an exponential law is used to relate slip to traction coefficient at each contact point.

The coefficient of friction is governed by the following relationship and represented in Figure 4.6:

$$\mu = \mu_o \left( 1 - e^{-\frac{|v_s|}{v_0}} \right) \tag{4.25}$$

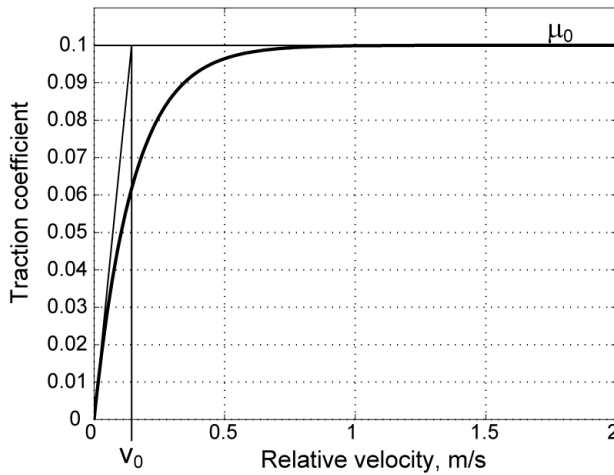


Figure 4.6: Exponential friction law

## 4.4 Elastic deformation

In the literature, different elastic models of CVT are available (*Section 4.1*). All the authors take into account the pulley deformations, some also include the intermediate element deformations (longitudinal and transversal) and only few shaft bending, but no one considers the contact point deformation. In the case of the metallic belt, this can be justified, as the longitudinal stiffness of the belt is high. In the case of CVT chains, the contact point deformations could be of same order as the pulley deformations or the pin compression. This is especially true for small radius of contact, where the pulley is stiffer than for large radius.

The elastic deformations considered in this thesis are:

1. elastic deformations of the pulley and contact point due to the normal forces, Figure 4.7(a)
2. clearance between the sheave pulley and the shaft, Figure 4.7(b)
3. pin compression, Figure 4.7(c)

### 4.4.1 Pulley deformation

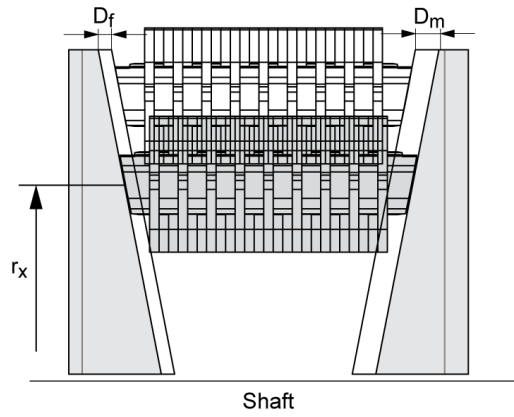
Sattler models the radius change due to pulley deformation using trigonometric relation (Sattler (1999)). A few authors (Carbone et al. (2005), Srivastava et al. (2006); Srivastava & Haque (2007)) use this model for the pulley elastic deformations. This model uses a parameter to describe the pulley stiffness. Using FEM calculations, the equation of this parameter can be determined (Sferra et al. (2002)). The Sattler model is simple therefore attractive. Unfortunately, FEM simulations show this model is not appropriate for the pulleys used in this thesis (*Appendix C*), therefore a specific model is developed.

To avoid FEM simulation (as shown in Figure 4.8) for each step of the calculation, an on line FEM simulation for different radius  $R_{x,0}$ , different normal forces  $N_n$  is used. The output of the FEM simulation is the axial deformation  $D_{n,y}$ <sup>1</sup> (Figure 4.7(a)) that depends on the angular position  $\theta_{def}$  where the elastic deformation is measured. A 3D table is then obtained and allows to interpolate deformations for any data set  $(R_{x,0}, N_n, \theta_{def})$ . The total movable or fixed pulley elastic deformations  $D_y$  is then equal to the summation of each deformation due to each normal force  $D_{n,y}$ , i.e. theorem of superposition. Finally, the total axial pulley elastic deformations  $D_{fm}$  is equal to the summation of the total movable pulley deformations  $D_m = \sum_n D_{n,m}$  and the total fixed pulley deformations  $D_f = \sum_n D_{n,f}$ .

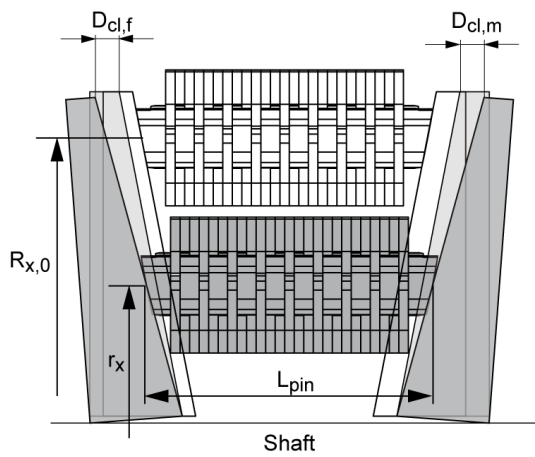
$$D_{fm} = \sum_n D_{f,n} + \sum_n D_{m,n} \quad (4.26)$$

---

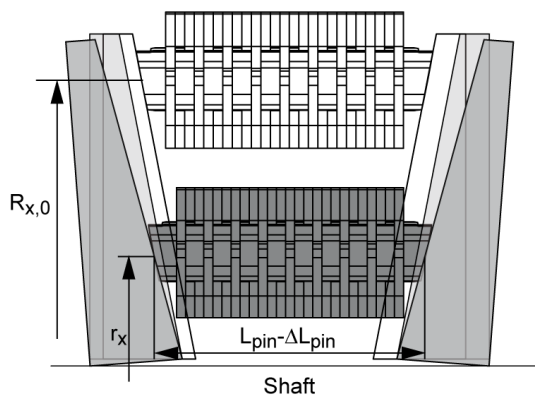
<sup>1</sup>y = f for the fixed pulley, y = m for the movable pulley



(a) Radius change due to the pulleys sheave and contact point deformations



(b) Radius change due to the clearance between the shaft and the pulley sheaves



(c) Radius change due to the pin compression

Figure 4.7: The different elastic deformations of the pulley sheaves and pins

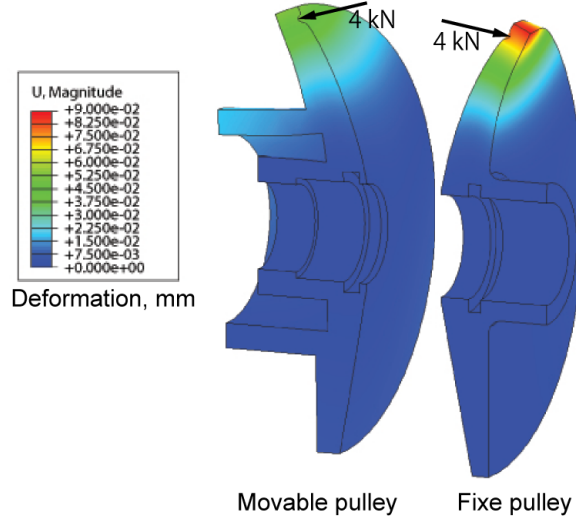


Figure 4.8: FEM simulation of the movable and fixed pulley with a normal force equal to 4 kN

Several authors who consider pulley deformations are using a contact point load. As it was already pointed out, in the case of the chain, the contact point deformation between the pin and the pulley sheave can be of the same order than the pulley deformation or the pin compression. Therefore, instead of a point load contact, the crowning of the pin is directly considered in the FEM simulation.

#### 4.4.2 Pulley sheave and shaft clearance

Due to the clearance between the pulley and the shaft, the pulley sheave is inclined (Figure 4.9). The pulley inclination is determined by a rather straight forward geometrical formula (Sattler (1999), Carbone et al. (2005), Tarutani et al. (2006)). If the contact point deformation between the pulley and shaft is neglected, and the maximum value of the inclination allowed by the clearance is defined by  $\delta_y$ , the axial displacement at radius  $R_{x,0}$  and angle position  $\theta$  in each pulley become  $D_{cl,y}$ :

$$D_{cl,y} = \delta_y R_{x,0} \cos(\theta - \theta_c) \quad (4.27)$$

Where  $\theta_c$  is the center of the wedge expansion. This angle depends on the normal force distribution. Considering the equilibrium of moments (Tarutani et al. (2006) and Carbone et al. (2005)), this angle is written

$$\tan \theta_c = \frac{\sum_n N_n \sin \theta}{\sum_n N_n \cos \theta} \quad (4.28)$$

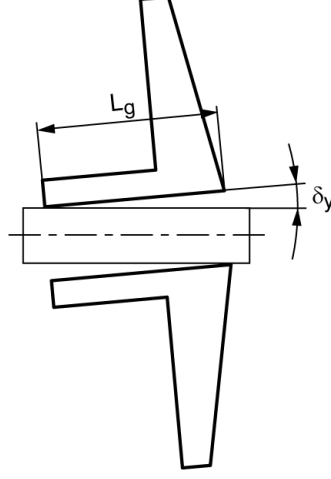


Figure 4.9: Pulley deformation due to the clearance between shaft and pulley

Finally, the total deformation due to the shaft and pulley sheaves clearance is then the summation of the two displacements (fixed and movable sheave).

$$D_{cl} = D_{cl,f} + D_{cl,m} \quad (4.29)$$

#### 4.4.3 Pin compression

Each pin in contact with pulleys are compressed due to the normal force  $N_n$  acting on it. The pin compression is calculated by the law of elasticity:

$$\sigma_{pin} = \frac{\Delta L_{pin}}{L_{pin}} E_{pin} \quad (4.30)$$

Where  $\sigma_{pin}$  is the stress,  $L_{pin}$  and  $\Delta L_{pin}$  are the pin length and the pin compression respectively and  $E_{pin}$  is the Young modulus. The stress is equivalent to the axial force acting on the pin divided by the pin area  $A_{pin}$ . Finally, the variation of the pin length  $\Delta L_{pin}$  could be written as a function of the normal force  $N_n$ .

$$\Delta L_{pin} = N_n \cos \beta_0 \frac{L_{pin}}{A_{pin}} E \quad (4.31)$$

#### 4.4.4 Pulley radius deformation

The two previous section described pulleys and pins deformations in the axial direction. As the radial direction is the interest, geometrical relations are used to transform axial deformations in radial one. Figure 4.10 represents the elements in position when the deformations are considered or not.

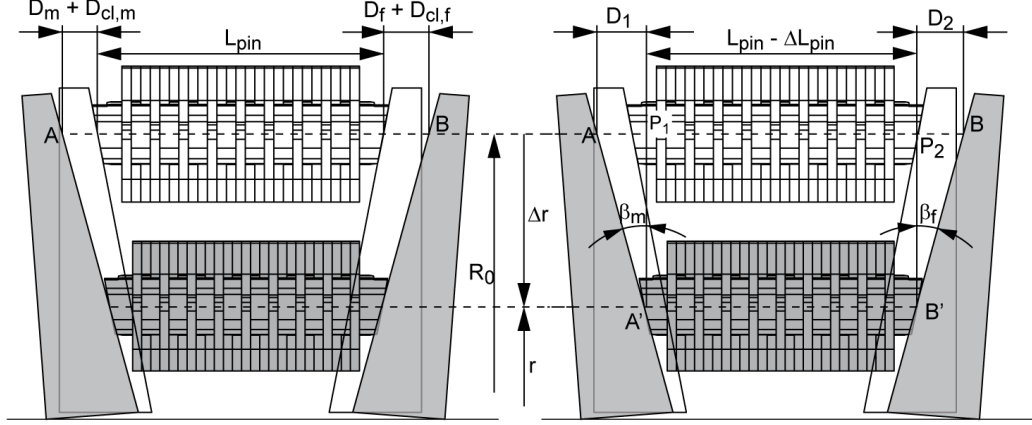


Figure 4.10: Radial movement of the pin due to the pulley elastic deformations and pin compression

Considering the top line at radius  $R_0$ , the length of the line from A to B can be expressed:

$$AB = (D_m + D_{cl,m}) + L_{pin} + (D_f + D_{cl,f}) \quad \text{or} \quad (4.32)$$

$$AB = D_1 + (L_{pin} - \Delta L_{pin}) + D_2 \quad (4.33)$$

By rearranging the terms one obtains:

$$D_m + D_{cl,m} + D_f + D_{cl,f} + \Delta L_{pin} = D_1 + D_2 \quad (4.34)$$

Using the geometry of the triangle  $AA'P_1$  and  $BB'P_2$ , the radial displacement  $\Delta r$  yields to:

$$\Delta r = \frac{D_1}{\tan \beta_m} \quad \text{or} \quad (4.35)$$

$$\Delta r = \frac{D_2}{\tan \beta_f} = \frac{D_m + D_{cl,m} + D_f + D_{cl,f} + \Delta L_{pin} - D_1}{\tan \beta_f} \quad (4.36)$$

By replacing  $D_1 = \Delta r \tan \beta_m$  from (4.35) into (4.36), one can express the deformed radius as

$$r = R_0 - \Delta r = R_0 - \frac{D_m + D_{cl,m} + D_f + D_{cl,f} + \Delta L_{pin}}{\tan \beta_m + \tan \beta_f} \quad (4.37)$$

## 4.5 Numerical procedure

The model presented in Section 4.3 shows many interactions. The elastic deformations depend on the normal forces acting on the pulley sheave. The normal forces belong to the chain forces that depend on the sliding friction angle  $\gamma$ . This angle belongs itself to the sliding speed that is influenced by the elastic deformations of the pulley.

The algorithm to solve the problems is shown in Figure 4.11 (Tenberge (2004), Tarutani et al. (2006)).

Inputs needed to solve the algorithm are the secondary clamping force  $F_s$ , the primary torque  $T_p$ , the primary and the secondary pulley radius  $R_p$  and  $R_s$  respectively and finally the time rate of the radius change  $\frac{dR_x}{dt}$ . If the steady-state condition are considered,  $\frac{dR_x}{dt} = 0$

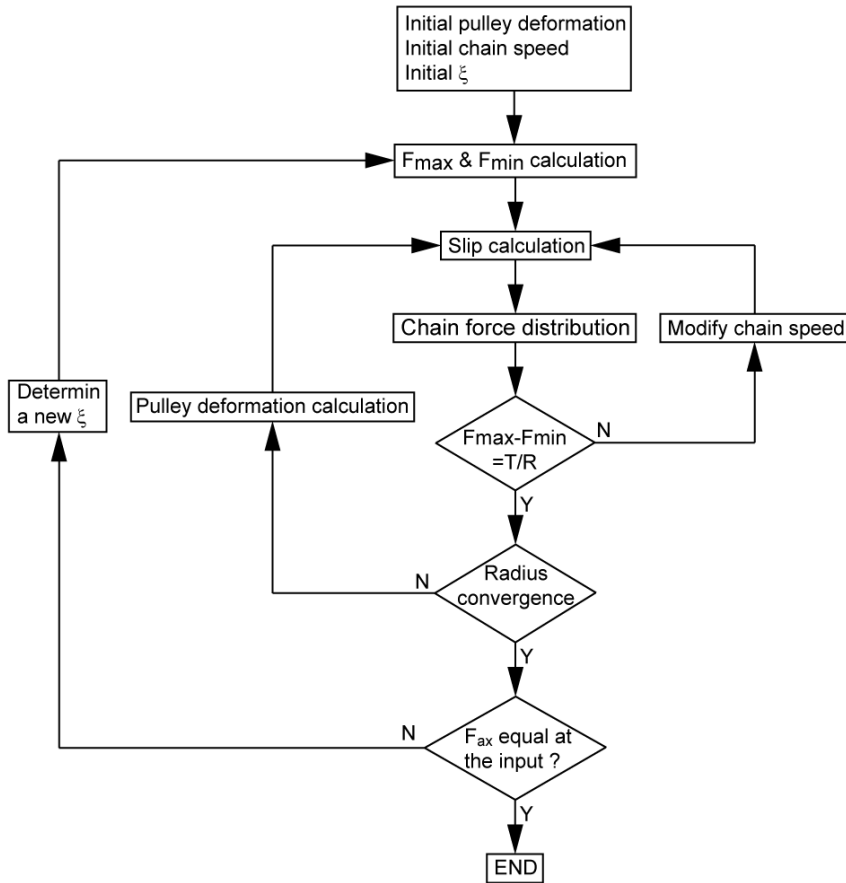


Figure 4.11: Calculation procedure

The process starts with an arbitrary elastic deformation, an initial chain speed and initial value of  $\xi = \frac{F_{min}}{F_{max}}$ . Where  $F_{min}$  and  $F_{max}$  are the minimum and respectively the maximum chain force. In a first step, the maximum and minimum chain force  $F_{max}$  and  $F_{min}$  are calculated:



$$F_{max} = \frac{T_p}{R_p} \frac{1}{\xi - 1} \quad (4.38)$$

$$F_{min} = \xi F_{max} \quad (4.39)$$

In a second step, the sliding angles between the pins and the pulley sheaves and the chain force distribution is calculated using the initial pulley deformations. As the torque transfer does not correspond any more to the desired torque, the chain speed is varied in a first iteration until the torque transfer equals the desired one. The change of the chain speed varies the tangential slip that affects the sliding angle and finally the chain force distribution.

The chain forces obtained at this point of the simulation use an estimate of pulley deformations. With these new chain forces distributions, a new pulley deformation can be calculated in a second iteration. This iteration is repeated until the deformed radius distribution does not change any more.

Finally, the ratio of the minimum and maximum chain force  $\xi$  is varied in a third iteration until the pulley clamping force is equal to the input. At this step of the simulation, the maximum and the minimum chain forces, the secondary pulley torque, sliding angle, for example, are determined.

Using the maximum and minimum chain forces,  $F_{max}$  and  $F_{min}$  respectively, the same algorithm is applied to the primary pulley. At this time, the third iteration is not necessary, as the maximum and the minimum chain force are used as inputs. At the end of the secondary and the primary pulley calculations, for example the clamping force, the torque, the sliding velocity, the chain force distribution and the normal force for each contact point are determined.

## 4.6 Intermediate element speed

The primary and the secondary pulleys are not only coupled by the minimum and the maximum chain forces  $F_{min}$  and  $F_{max}$  respectively (*Section 4.5*) but also by the velocity of the intermediate element. The speed at the output of one pulley should be equal to the velocity at the entry of the other pulley.

The chain velocity  $v_{ch}$  is

$$v_{ch} = \sqrt{(r\omega + v_\theta)^2 + v_r^2} \quad (4.40)$$

Two cases can be considered: the geometrical ratio  $r_{cut,g}$  is constant or the speed ratio  $r_{cut}$  is constant.

### 4.6.1 Geometrical ratio constant

In the case of a constant geometrical ratio, the primary and the secondary pulley radius  $R_p$  and  $R_s$  respectively are constant. The primary pulley velocity is considered to be known and the secondary pulley velocity should be varied

until the chain velocity of the exit of the primary pulley is equal to the chain velocity at the entry of the secondary pulley.

#### 4.6.2 Speed ratio constant

For the case of a constant speed ratio, the primary speed and ratio speed are supposed to be known and constant. In this case, the pulleys radiuses should be changed until the second coupling condition is reached.

After solving the problems, forces and the slip involved in the system are known and can be used to estimate the chain efficiency.

### 4.7 Efficiency model

The calculation of the chain efficiency is based on the determination of the losses of each contact point in contact with the pulley.

The following assumptions are made:

- No losses between each links
- No losses between pins and strips
- No losses between pins and links
- No losses between strips and links

The contact point between the pin and the pulley sheave is locally deformed due to the normal force acting on it. We assume the area of contact and elastic deformation is equivalent to an ellipse that can be determined by the Hertz contact theory (Johnson (1985), Harris (1991)).

#### 4.7.1 Hertz contact

Two bodies of revolution having different radius of curvature may contact each other at single point if no load is applied. Such a condition is called point contact (Harris (1991)). Figure 4.12 shows this condition.

The radius  $R_{\Lambda, pin}$  and  $R_{\Gamma, pin}$  are defined by the crowning of the pin and  $R_{\Lambda, pl}$  and  $R_{\Gamma, pl}$  are defined by the crowning of the pulley where,  $R_{\Gamma, pl}$  is infinite and  $R_{\Lambda, pl}$  is proportional to the pulley radius.

$$R_{\Lambda, pl} = \frac{R_x}{\sin \beta_0} \quad (4.41)$$

The two radius of the contact ellipse (Figure 4.13) are expressed as (Harris (1991)):

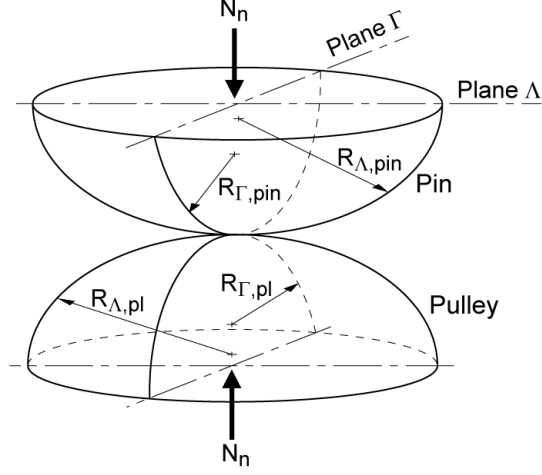


Figure 4.12: Geometry of contacting bodies (Harris (1991))

$$a = \left( \frac{2\kappa^2 \mathcal{E}}{\pi} \right)^{\frac{1}{3}} \left[ \frac{3N_n}{2\Sigma_\rho} \left( \frac{1-\nu_1^2}{E_{pin}} + \frac{1-\nu_2^2}{E_{pl}} \right) \right]^{\frac{1}{3}} \quad (4.42)$$

$$b = \left( \frac{2\mathcal{E}}{\pi\kappa} \right)^{\frac{1}{3}} \left[ \frac{3N_n}{2\Sigma_\rho} \left( \frac{1-\nu_1^2}{E_{pin}} + \frac{1-\nu_2^2}{E_{pl}} \right) \right]^{\frac{1}{3}} \quad (4.43)$$

where  $E_{pin}$  and  $E_{pl}$  are the Young modulus of the pin and the pulley respectively,  $\nu_{pin}$  and  $\nu_{pl}$  are the Poisson coefficient of the two bodies.

In accordance with Figure 4.13, the normal contact pressure  $p_{xy}$  at a certain position  $(x, y)$  within the contact is:

$$p_{xy} = \frac{3N_n}{2\pi ab} \sqrt{1 - \left(\frac{x}{a}\right)^2 - \left(\frac{y}{b}\right)^2} \quad (4.44)$$

#### 4.7.2 Friction forces and moments

The elliptical ellipse generated by the contact between the pin and the pulley can be divided a differential area  $dS$ . Figure 4.14 shows a part of the ellipse with the differential area  $dS$  at the coordinate  $x$  and  $y$  from the center of the ellipse. The velocity  $v_s = [v_\theta \ v_r]^T$  is the slip velocity vector between the pin and the pulley sheave.  $\omega_s$  is the sliding slip due to the relative angular velocity between the pin and the pulley.

If we assume a sliding friction model, the differential friction force  $dF_{fr}$  defined inside the ellipse is equivalent to the product of the normal stress at the coordinate point  $(x, y)$ , the friction coefficient  $\mu$  and the area  $dS$ :

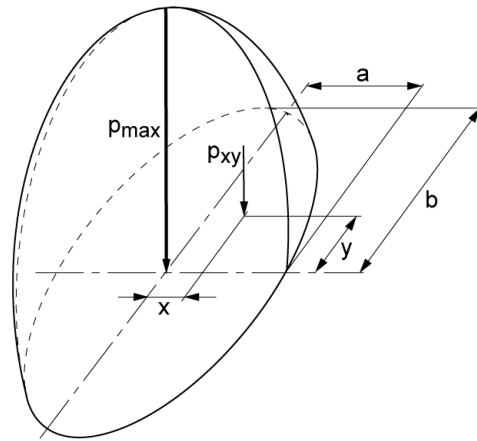


Figure 4.13: Ellipsoidal contact pressure distribution (Harris (1991))

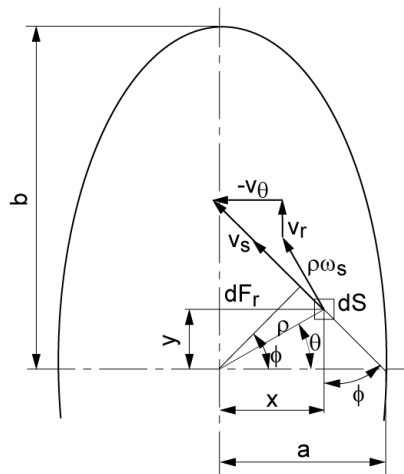


Figure 4.14: Friction force and sliding velocities acting on differential area  $dS$  of the elliptical contact surface (Harris (1991))

$$dF_{fr} = \frac{3\mu N_n}{2\pi ab} \sqrt{1 - \frac{x^2}{a^2} - \frac{y^2}{b^2}} dS \quad (4.45)$$

The friction force  $dF_{fr}$  can be decomposed in  $x$  and  $y$  direction  $dF_{fr,x} = dF_{fr} \sin \phi$  and  $dF_{fr,y} = dF_{fr} \cos \phi$  respectively. Then the total friction force in each direction is given by the integral around the ellipse (Harris (1991)):

$$F_{fr,x} = \frac{3\mu N_n}{2\pi ab} \int_{-a}^a \int_{-b\sqrt{1-\left(\frac{x}{a}\right)^2}}^{b\sqrt{1-\left(\frac{x}{a}\right)^2}} \sqrt{1 - \left(\frac{x}{a}\right)^2 - \left(\frac{y}{b}\right)^2} \sin \phi dy dx \quad (4.46)$$

$$F_{fr,y} = \frac{3\mu N_n}{2\pi ab} \int_{-a}^a \int_{-b\sqrt{1-\left(\frac{x}{a}\right)^2}}^{b\sqrt{1-\left(\frac{x}{a}\right)^2}} \sqrt{1 - \left(\frac{x}{a}\right)^2 - \left(\frac{y}{b}\right)^2} \cos \phi dy dx \quad (4.47)$$

The differential friction force  $dF_{fr}$  does not necessarily act at right angles to a radius drawn from the geometrical center of the contact ellipse and generate a certain moment  $dM_s$  about the center of the contact ellipse given by:

$$dM_s = \rho \cos(\phi - \theta) dF_{fr} \quad (4.48)$$

With the geometry, the value of  $\rho$  and  $\theta$  can be found and replaced into (4.48) to give the total frictional moment about the center of the contact ellipse (Harris (1991)):

$$M_s = \frac{3\mu N_n}{2\pi ab} \int_{-a}^a \int_{-b\sqrt{1-\left(\frac{x}{a}\right)^2}}^{b\sqrt{1-\left(\frac{x}{a}\right)^2}} \sqrt{x^2 + y^2} \sqrt{1 - \left(\frac{x}{a}\right)^2 - \left(\frac{y}{b}\right)^2} \cos(\phi - \theta) dy dx \quad (4.49)$$

Friction forces and the friction moment are now used to calculate the losses at the contact point and the chain efficiency.

### 4.7.3 Chain efficiency

The chain efficiency is estimated by the summation of all contact point losses. The eventual losses between links, links and pins or strips and finally between pins and strips are neglected.

The contact loss  $\Delta P_{l,i}$  of one contact yields to :

$$\Delta P_{l,i} = F_{fr,x} v_\theta + F_{fr,y} v_r + M_s \omega_s \quad (4.50)$$

The first and second term are losses due to the slip in  $x$  and  $y$  direction. The third is loss due to the spin torque.

The summation of all contact points losses then gives the total loss  $\Delta P_{l,x}$  and the efficiency  $\eta_x$  for one pulley :

$$\Delta P_{l,x} = 2 \sum_n \Delta P_{l,i} \quad (4.51)$$

$$\begin{aligned} \eta_x &= \frac{P_{out,x}}{P_{in,x}} \\ &= \frac{P_{in,x} - \Delta P_x}{P_{in,x}} \\ &= 1 - \frac{\Delta P_x}{P_{in,x}} \end{aligned} \quad (4.52)$$

The input power of the primary pulley  $P_{in,p}$  is given by the rotation speed and input torque of the primary pulley  $\omega_p$  and  $T_p$  respectively. Finally the efficiency in the primary pulley yields to

$$\eta_p = 1 - \frac{\Delta P_{l,p}}{T_p \omega_p} \quad (4.53)$$

The primary pulley efficiency  $\eta_p$  gives the input power  $P_{in,s}$  of the secondary pulley if no other losses are considered.

$$\begin{aligned} P_{in,s} &= P_{in,p} \eta_p \\ &= T_p \omega_p \eta_p \end{aligned} \quad (4.54)$$

and the efficiency of the secondary pulley becomes

$$\eta_s = 1 - \frac{\Delta P_s}{T_{l,p} \omega_p \eta_p} \quad (4.55)$$

Finally the chain efficiency  $\eta_{ch}$  is the multiplication of the primary and the secondary pulley efficiency,  $\eta_p$  and  $\eta_s$  respectively.

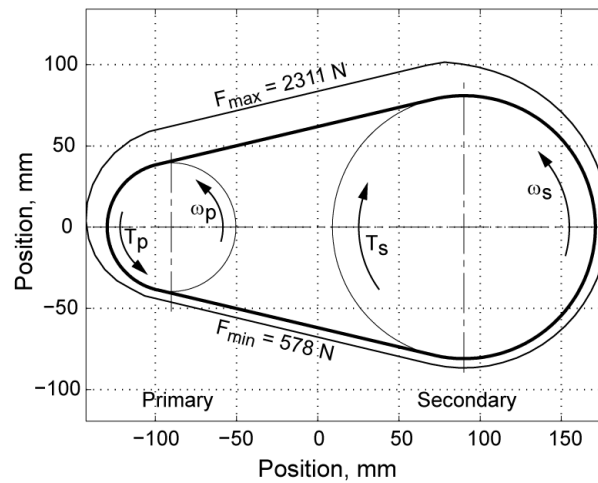
$$\eta_{ch} = \eta_p \eta_s \quad (4.56)$$

## 4.8 Simulation

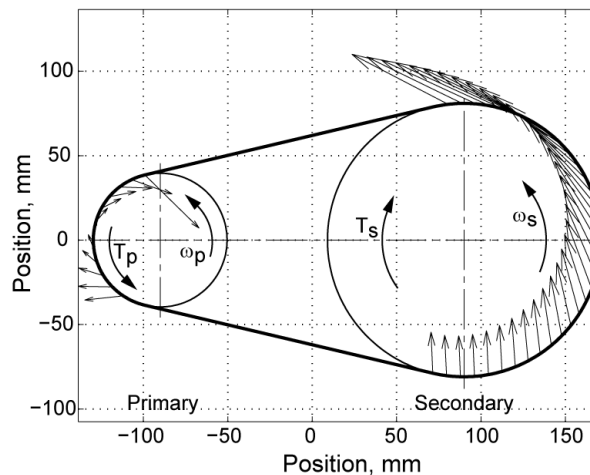
This section depicts some few results obtained by the low level model presented in this chapter. Other results as the traction curve and slip simulation can also be found in *Chapter 6* and *Appendix C* for the pulley radius deformations.

## 4.8.1 Chain forces and slip

Figure 4.15 depicts a simulation results in underdrive ratio with an input torque  $T_p$  equivalent to  $50Nm$ . The maximum and minimum chain forces,  $F_{max}$  and  $F_{min}$  respectively, and the chain force distribution when the chain is clamped into the pulley are shown in Figure 4.15(a). The slip behavior between the pulley sheaves and the chain (Figure 4.15(b)) shows a position where the radial slip is null and changes the sign. This angular position corresponds to the maximum of the pulley radius deformation and equivalent to the center of edge expansion.



(a) Chain force distribution



(b) Slip vector from the pulley sheave to the chain

Figure 4.15: Low level model simulation results in underdrive ratio for a input torque equal to  $50Nm$

### 4.8.2 Variator matrix

Clamping forces, slips and traction coefficients can be calculated for each working point. A complete matrix of the variator characteristics is then obtained. The inputs of this matrix are the slip of each pulley  $s_x$ , the secondary clamping force  $F_s$ , the load factor  $L_f$  and the geometrical ratio  $r_{cvt,g}$ . The outputs are the chain efficiency  $\eta_{ch}$ , the primary clamping force  $F_s$  and the traction coefficient  $\mu_x$ . Figure 4.16 depicts one example for a geometrical ratio equal to 0.83.

### 4.8.3 Shifting

This low model also predicts the evolution of the geometrical ratio during shifting. Figure 4.17 shows an example of the rate of change of the ratio for a geometrical ratio 1:1. Two modes are observed: the creep mode (usual mode of the CVT) and the slip mode (Ide et al. (1996), Carbone et al. (2001, 2005)). It was discussed in *Section 4.3* that the radial slip is composed by the slip due to pulley deformation and the slip due to shifting. During slip mode, the slip due to shifting is predominant. During the creep mode, pulley deformations take an important part of the shifting process (Ide et al. (1996), Carbone et al. (2001, 2005)).

## 4.9 Summary

The low level model of the variator was derived in this chapter. A simple geometrical model without considering any deformations was presented. Then, considering elastic deformations of the pulleys and the elongation of the chain, kinematics equations were found. On the basis of equilibrium considerations, the forces involved in the system were calculated.

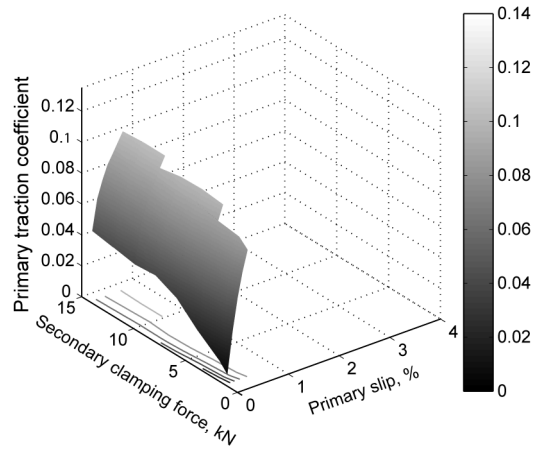
Elastic deformations due to the forces acting on the pulley sheaves, the clearance between the pulley and the shaft, the chain elongation and the pin compression constitute the elastic deformations of the system. These deformations play an important part for the calculation of the slip between the pulley sheaves and the pin chain.

The contact point deformation between the pulley sheaves and the pin is described by the Hertz contact theory. Friction forces and torques at the contact points are calculated and losses for each contact point estimated to determine the power loss due to each contact point and finally a model of the chain efficiency is derived.

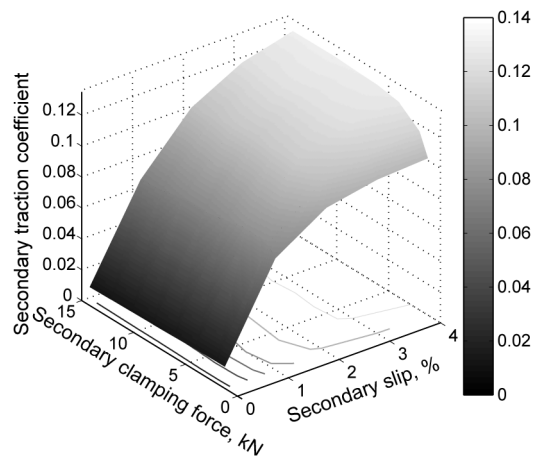
The creep mode and the slip mode during shifting can be described by this model. The creep mode is defined by the slip due to the shifting and the slip due to elastic deformations. During the slip mode, the radial slip due to the shifting is predominant and the elastic deformations can be neglected.

The main results of this low level model presented in this chapter are pulley forces, pulley torques, traction curves and slip for each pulley. They will be integrate in the high level model described in the next chapter.

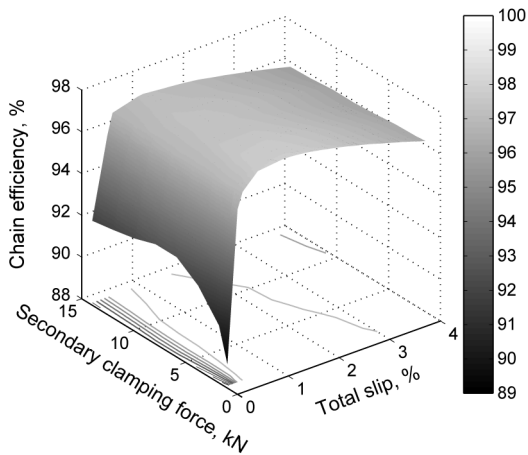




(a) Primary traction curve as a function of the primary slip and the secondary clamping force



(b) Secondary traction curve as a function of the secondary slip and the secondary clamping force



(c) Chain efficiency as a function of the total slip and the secondary clamping force

Figure 4.16: Simulation results of the primary, secondary traction curve and variator efficiency as a function of slip and secondary clamping force for a geometrical equal to 0.83

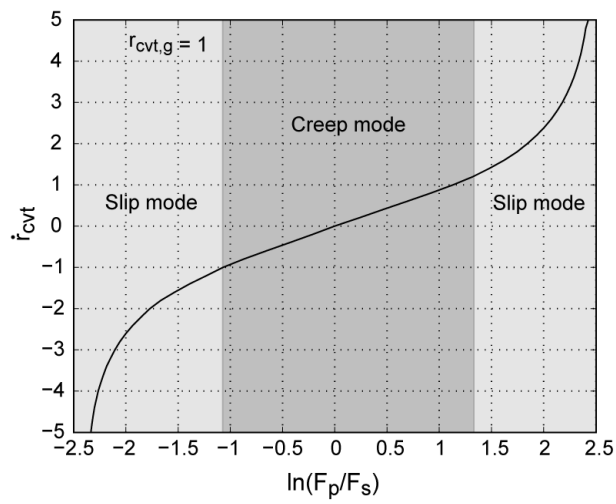


Figure 4.17: Rate of change of the ratio as a function of the logarithm of the primary to secondary clamping force ratio

## Chapter 5

# High level model

The model described in the previous chapter gives complete characteristics of the variator as for example the pulley clamping forces and the traction curve. These results are integrated in a larger model to describe the dynamic of the variator. This high level model does not only consider the variator dynamics but also the hydraulic and the actuator dynamics, elements important to consider for the variator control.

This chapter is structured as follows. Firstly, the state of the art is presented following by the description of the interactions of the system. Thirdly, the actuator model and the hydraulic model are defined. Then the differential equations of the variator and of the slip are derived. The complete variator dynamics are summarized in the last section.

### 5.1 State of the art

#### 5.1.1 Variator dynamics

Essentially three models can be found in the literature to describe the shifting behavior of the variator: The Shafai model (Shafai et al. (1995)), the Ide model (Ide et al. (1994, 1996)) and the CMM model (Carbone et al. (2001, 2006)). The Shafai and Ide models use a number of linear fits to arrive at a gray-box model. They are differentiated by the fact that Shafai describes the velocity of the pulley displacement whereas Ide describes the rate of change of the ratio. The CMM model gives a linear relation between the rate of the ratio change and the logarithm of the primary and the secondary clamping force ratio. Additionally, the parameters of the CMM can be calculated by the low level model (*Chapter 4*) for example.

As far as the author knows, the Shafai or Ide model are the most widely used to describe the variator dynamics and only few authors used the CMM model (Simons et al. (2006), Bonsen (2006), Carbone et al. (2006)). The last authors pointed out that for a ratio of the clamping force smaller than one the Ide model shows some divergence. They explain that the Ide model is a first order approximation of the logarithm of the clamping force ratio used in

the CMM model. It can be concluded that the CMM model gives the most accurate results.

### 5.1.2 Servo pumps modelling

The hydraulic system used in this thesis is using two servo pumps to set the primary and the secondary pulley pressure (*Section 2.2*). As far as the author knows, only few authors describe the servo pump model. Cools & Veenhuizen (2004) and Metsenaere et al. (2005) give a model of the needed torque to drive the pump. They control the shifting pump in speed and the secondary pump in torque. Cools & Veenhuizen (2004) claim that more stable control is achieved, since the primary pressure acts independently of the secondary pressure. Oudijk (2005) uses the two servo pumps controlled in torque. He also models the power consumption of the servo hydraulic system.

*Appendix D* gives a complete model of the actuator dynamics. The servo motor is described by taking into account the electric and mechanical characteristics of the motor.

## 5.2 System interactions

Before entering in the details of the modeling, the system interactions are described. They can be divided into two groups: actuators interactions, hydraulic and variator interactions.

### 5.2.1 Actuators interactions

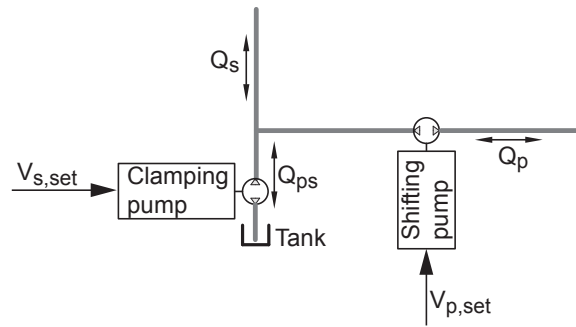
Figure 5.1(a) depicts the actuators system used in this work, where  $V_{x,set}$  is the command set point of the servo pump. A variation of the command  $V_{p,set}$  modifies the flow  $Q_p$  and perturbs the secondary flow  $Q_s$ . If the system is perfect, the command  $V_{s,set}$  acts only on the secondary flow  $Q_s$  (Figure 5.1(b)).

### 5.2.2 Hydraulic and variator interactions

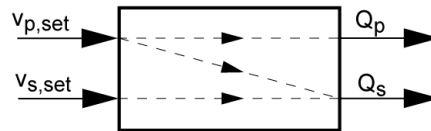
Let us consider that the system is in steady state, i.e. the primary and the secondary clamping forces equilibrium the system. Now, when the primary pressure (the primary clamping force) changes, the equilibrium between the primary and the secondary clamping forces is broken and the two movable sheaves move. These axial mechanical movements vary the hydraulic volumes and then affect the two pressures. Figure 5.2 describes this loop-interaction between the hydraulic and the mechanical parts i.e the variator.

## 5.3 Actuator models

The actuator models describe the dynamic behavior of the servo pump or more precisely the flow going out of the pump. The servo pump is composed of



(a) Servo pump hydraulic system without the variator



(b) Representation of the interactions between the shifting pump and the clamping pump

Figure 5.1: Servo pump hydraulic system and the interactions between each pump

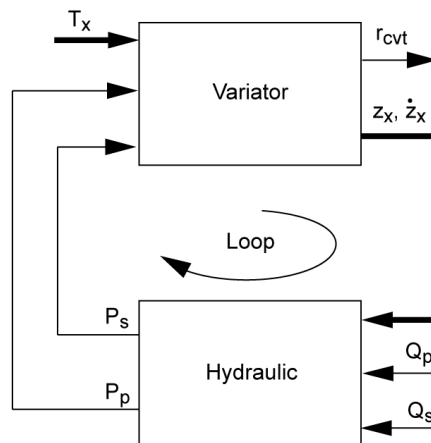


Figure 5.2: Representation of the variator and the hydraulic interactions

three elements: the servo amplifier, the servo motor and the hydraulic pump. The servo amplifier generates a signal to the servo motor that corresponds to the desired torque or rotation speed depending on the control mode (torque or speed control mode)

### 5.3.1 Control mode of the servo pump

The servo pump produces a flow going to the hydraulic volume of the variator and generates a pressure. This pressure creates a resistive torque on the servo motor. The servo motor can be used either in torque control, or in speed control.

The servo pump generates a flow proportional to the rotation speed and as it will be seen in *Section 7.3* the flow could be used to control the pressure. Then it is proposed to use the two servo pumps in speed mode. The input vector is the voltage to set the rotation speed  $\mathbf{U}_{act} = [ V_{p,set} \ V_{s,set} ]^T$  and the output vector is the flow going in or out of the pulleys  $\mathbf{Y}_{act} = [ Q_p \ Q_s ]$ .

### 5.3.2 Servo pump model

The servo motor and the hydraulic pump can be modeled using the electric and mechanical equations of the motor and the pump characteristics. *Appendix D* shows this model.

This kind of model is somehow complicated and simpler models are desired for control purposes. If the servo pump is controlled in speed, it was found experimentally that the flow generated by the servo pump is equivalent to a second order transfer function.

$$Q_{sp} = \frac{G_{sp}\eta_{sp}}{a_{sp}s^2 + b_{sp}s + 1}V_{s,set} \quad (5.1)$$

$$Q_p = \frac{G_p\eta_p}{a_p s^2 + b_p s + 1}V_{p,set} \quad (5.2)$$

where  $G_x$  is the gain,  $\eta_x$  the hydraulic efficiency of the pump and  $V_{x,set}$  is the servo amplifier input voltage to set the servo motor speed.

The secondary flow  $Q_s$  is equal to the difference between the flow provided by the clamping pump  $Q_{sp}$  and the shifting pump  $Q_p$

$$Q_s = Q_{sp} - Q_p \quad (5.3)$$

Using the state space notation, the primary flow  $Q_p$  and the secondary flow  $Q_s$  can be written as

$$\begin{aligned}
\dot{\mathbf{X}}_{\text{act}} &= \begin{bmatrix} 0 & 1 & 0 & 0 \\ -\frac{1}{a_p} & -\frac{b_p}{a_p} & 0 & 0 \\ 0 & 0 & 0 & 1 \\ 0 & 0 & -\frac{1}{a_{sp}} & -\frac{b_{sp}}{a_{sp}} \end{bmatrix} \mathbf{X}_{\text{act}} + \begin{bmatrix} 0 & 0 \\ \frac{G_p \cdot \eta_p}{a_p} & 0 \\ 0 & 0 \\ 0 & \frac{G_{sp} \cdot \eta_{sp}}{a_{sp}} \end{bmatrix} \mathbf{U}_{\text{act}} \\
\mathbf{Y}_{\text{act}} &= \begin{bmatrix} 1 & 0 & 0 & 0 \\ -1 & 0 & 1 & 0 \end{bmatrix} \mathbf{X}_{\text{act}}
\end{aligned} \tag{5.4}$$

Where  $\mathbf{X}_{\text{act}} = [ Q_p \quad \dot{Q}_p \quad Q_{sp} \quad \dot{Q}_{sp} ]^T$  is the state vector,  $\mathbf{U}_{\text{act}} = [ V_{p,set} \quad V_{s,set} ]^T$  is the input vector and  $\mathbf{Y}_{\text{act}} = [ Q_p \quad Q_s ]^T$  is the output vector.

## 5.4 Hydraulic model

Basically a hydraulic circuit is a succession of volumes and restriction passages called orifices. For the volume, the continuity condition (5.5) yields that the difference between flow coming in  $Q_i$  and out  $Q_o$  of a volume  $V$ , also called the consumed flow, is due to the volume expansion and/or to the compressibility flow resulting from a pressure change. This equation was obtained with the assumption that isothermal conditions exist in the liquid flow. For practical use, it is important to define accurately the effective bulk modulus  $\beta_e$ . This parameter can be substantially lowered by trapped air and/or mechanical compliance of the considered volume. The continuity equation is reviewed with a detailed relation of the effective bulk modulus (Gruber (1988), Merritt (2001)):

$$\sum Q_i - \sum Q_o = \frac{dV}{dt} + \frac{V}{\beta_e} \frac{dP}{dt} \tag{5.5}$$

Figure 5.3 shows the hydraulic system of the variator.  $V_x$  is the piston volume,  $z_x$  is the pulley position,  $P_x$  is the pulley pressure and  $Q_x$  is the flow that enters or exits the pulley. The leakages are neglected as the pulley leakages used in this work are small.

The volume of the pulley  $V_x$  is equal to the initial volume  $V_{x,0}$ , for example at ratio 1:1, and the variation of the volume due to movable sheave displacement:

$$V_x = V_{x,0} + A_x z_x \tag{5.6}$$

$$\frac{dV}{dt} = A_x \frac{dz_x}{dt} = A_x \dot{z}_x \tag{5.7}$$

where  $\dot{z}_x$  is the axial velocity of the movable sheave (4.8),  $A_x$  is hydraulic area of the piston.

Introducing (5.6) and (5.7) into (5.5) and rearranging the terms, we express the rate of change of the pressure as:

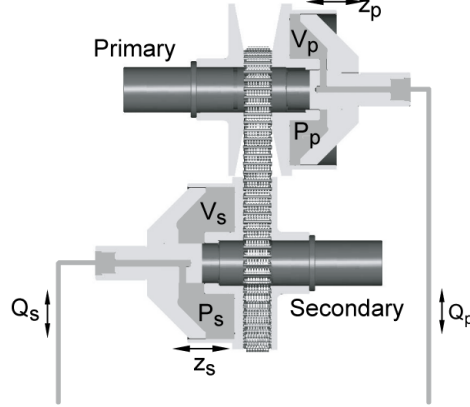


Figure 5.3: Representation of the variator without the actuators

$$\dot{P}_x = \frac{\beta_s}{V_{x,0} + A_x z_x} Q_x - \frac{A_x \dot{z}_x \beta_s}{V_{x,0} + A_x z_x} \quad (5.8)$$

## 5.5 Shifting model

The shifting model (transient variator model) depicts the relation between the variator shifting speed and the clamping forces. Based on the *Section 5.1.1* the CMM model is chosen (Carbone et al. (2006)). The shifting behavior can be described by:

$$\dot{r}_{cvt,g} = \omega_p G(r_{cvt,g}, F_s, L_f) \left[ \ln \left( \frac{F_p}{F_s} \right) - \ln \left( \frac{F_p}{F_s} \Big|_{eq} \right) \right] \quad (5.9)$$

where  $\frac{F_p}{F_s} \Big|_{eq}$  is the primary and the secondary clamping force ratio at the equilibrium,  $G$  is a function that depends on the geometrical ratio  $r_{cvt,g}$ , the secondary clamping forces  $F_s$  and the load factor  $L_f$ . The two parameters  $G$  and  $\frac{F_p}{F_s} \Big|_{eq}$  are calculated with the low level model described in *Chapter 4*

## 5.6 Slip model

The shifting model described in the previous section does not give any information on the variator slip and the model is only sufficient for ratio control. For slip control, the slip in the variator should be defined. As it was seen in *Section 3.2*, the slip of each pulley is a function of the pulley speed  $\omega_x$ , the geometrical radius of the pulley  $R_x$  and the chain speed  $v_{ch}$ .



$$v_p = \omega_p R_p - v_{ch} \quad (5.10)$$

$$v_s = v_{ch} - \omega_s R_s \quad (5.11)$$

$$(5.12)$$

Using the speed loss terminology, the dimensionless relative slip  $s_x$  is defined to describe the relative motion between each pulley and the intermediate element (Yamaguchi et al. (2006)).

$$s_p = \frac{v_p}{\omega_p R_p} = 1 - \frac{v_{ch}}{\omega_p R_p} \quad (5.13)$$

$$s_s = \frac{v_s}{\omega_s R_s} = \frac{v_{ch}}{\omega_s R_s} - 1 \quad (5.14)$$

The slip of each pulley determines the total slip of the variator as the summation of the primary and the secondary slip (*Section 3.2 and 3.3.1*).

$$\begin{aligned} s_{tot} &= s_p + s_s \\ &= v_{ch} \left( \frac{1}{\omega_s R_s} - \frac{1}{\omega_p R_p} \right) \end{aligned} \quad (5.15)$$

## 5.7 Mechanical model

The mechanical model of the variator consists of two pulleys and an intermediate element as represented in Figure 5.4. The primary inertia is lumped as inertia  $J_p$ ,  $J_s$  represents the secondary inertia and  $M_{ch}$  is the chain weight. Due to the tangential speed difference between pulleys and the intermediate element, a slip exists which results in a friction torque  $T_{x,fr}$  and a friction force  $F_{x,fr}$ . These torques and forces lead to the primary, the secondary and the chain speed according to:

$$J_p \dot{\omega}_p = T_p - T_{p,fr} \quad (5.16)$$

$$J_s \dot{\omega}_s = T_{s,fr} - T_s \quad (5.17)$$

$$M_{ch} \dot{v}_{ch} = 2F_{p,fr} - 2F_{s,fr} \quad (5.18)$$

The friction torque  $T_{x,fr}$  depends on the clamping force  $F_x$ , the pulley radius  $R_x$  that depends on the geometrical ratio  $r_{cvt,g}$ , the traction coefficient  $\mu_x$  that depends on the pulley slip  $s_x$  and the geometrical ratio  $r_{cvt,g}$ . The friction force  $F_{x,fr}$  depends on the traction coefficient  $\mu_x$  and the normal forces due to the clamping force  $F_x$ .

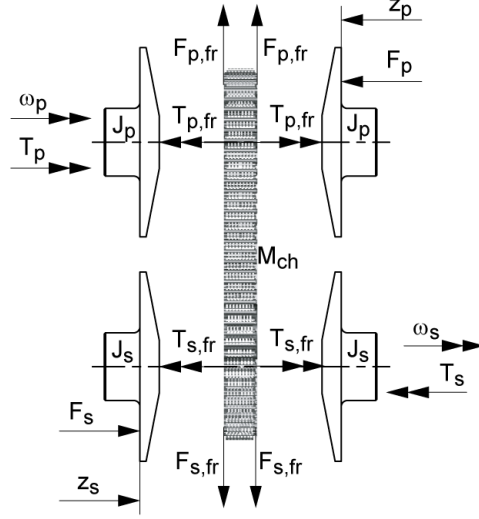


Figure 5.4: Forces and torques acting on the chain, the primary and secondary pulley

$$T_{x,fr} = \frac{2\mu_x(s_x, r_{cvt,g})}{\cos \beta_0} R_x(r_{cvt,g}) F_x \quad (5.19)$$

$$F_{x,fr} = \frac{2\mu_x(s_x, r_{cvt,g})}{\cos \beta_0} F_x \quad (5.20)$$

The traction coefficient  $\mu_x$  is obtained by the matrix traction curve for each pulley given by the low level model described in *Chapter 4*.

Introducing (5.19) and (5.20) into (5.16) to (5.18), the speeds of the two pulleys and the intermediate element become:

$$\dot{\omega}_p = \frac{1}{J_p} \left( T_p - \frac{2\mu_p}{\cos \beta_0} R_p F_p \right) \quad (5.21)$$

$$\dot{\omega}_s = \frac{1}{J_s} \left( \frac{2\mu_s}{\cos \beta_0} R_s F_s - T_s \right) \quad (5.22)$$

$$\dot{v}_{ch} = \frac{1}{M_{ch}} \left( \frac{2\mu_p}{\cos \beta_0} F_p - \frac{2\mu_s}{\cos \beta_0} F_s \right) \quad (5.23)$$

The ratio of the secondary and the primary pulley speeds,  $\omega_s$  and  $\omega_p$ , defines the speed ratio  $r_{cvt}$ .

$$r_{cvt} = \frac{\omega_s}{\omega_p} \quad (5.24)$$

## 5.8 Variator dynamics with slip

The variator dynamics with slip are obtained by assembling the different models defined in the previous sections; the total mechanical dynamics that consider the slip of each pulley is then summarized by:

$$\dot{\omega}_p = \frac{1}{J_p} \left( T_p - \frac{2\mu_p}{\cos \beta_0} R_p F_p \right) \quad (5.25)$$

$$\dot{\omega}_s = \frac{1}{J_s} \left( \frac{2\mu_s}{\cos \beta_0} R_s F_s - T_s \right) \quad (5.26)$$

$$\dot{r}_{cvt,g} = \omega_p G \left[ \ln \left( \frac{F_p}{F_s} \right) - \ln \left( \frac{F_p}{F_s} \Big|_{eq} \right) \right] \quad (5.27)$$

$$\begin{aligned} \dot{s}_p = & \frac{1-s_p}{\omega_p} \frac{1}{J_p} \left( T_p - \frac{2\mu_p}{\cos \beta_0} R_p F_p \right) - \frac{1}{\omega_p R_p} \frac{1}{M_{ch}} \left( \frac{2\mu_p}{\cos \beta_0} F_p - \frac{2\mu_s}{\cos \beta_0} F_s \right) \\ & + \frac{1-s_p}{R_p} \frac{dR_p}{dr_{cvt,g}} \omega_p G \left[ \ln \left( \frac{F_p}{F_s} \right) - \ln \left( \frac{F_p}{F_s} \Big|_{eq} \right) \right] \end{aligned} \quad (5.28)$$

$$\begin{aligned} \dot{s}_s = & -\frac{1+s_s}{\omega_s} \frac{1}{J_s} \left( \frac{2\mu_s}{\cos \beta_0} R_s F_s - T_s \right) + \frac{1}{\omega_s R_s} \frac{1}{M_{ch}} \left( \frac{2\mu_p}{\cos \beta_0} F_p - \frac{2\mu_s}{\cos \beta_0} F_s \right) \\ & - \frac{1+s_s}{R_s} \frac{dR_s}{dr_{cvt,g}} \omega_p G \left[ \ln \left( \frac{F_p}{F_s} \right) - \ln \left( \frac{F_p}{F_s} \Big|_{eq} \right) \right] \end{aligned} \quad (5.29)$$

$$r_{cvt} = \frac{\omega_s}{\omega_p} \quad (5.30)$$

$$s_{tot} = s_s + s_p \quad (5.31)$$

### 5.8.1 Linearized model

Defining the state vector  $\mathbf{X} = [ \omega_p \ \omega_s \ r_{cvt,g} \ s_p \ s_s ]^T$ , the input vector  $\mathbf{U} = [ F_p \ F_s \ T_p \ T_s ]^T$  and the output vector  $\mathbf{Y} = [ r_{cvt} \ s_{tot} ]^T$ , the non linear state-space formulation of the variator dynamics yield to:

$$\begin{aligned} \dot{\mathbf{X}} &= \begin{bmatrix} f_1(\mathbf{X}, \mathbf{U}) \\ f_2(\mathbf{X}, \mathbf{U}) \\ f_3(\mathbf{X}, \mathbf{U}) \\ f_4(\mathbf{X}, \mathbf{U}) \\ f_5(\mathbf{X}, \mathbf{U}) \end{bmatrix} \\ \mathbf{Y} &= \begin{bmatrix} g_1(\mathbf{X}, \mathbf{U}) \\ g_2(\mathbf{X}, \mathbf{U}) \end{bmatrix} \end{aligned} \quad (5.32)$$

When linearized around a working point  $\mathbf{X} = [ \omega_{p,0} \ \omega_{s,0} \ r_{cvt,g,0} \ s_{p,0} \ s_{s,0} ]^T$ , the linear state-space formulation of the variator dynamics becomes (*Appendix F*):

$$\dot{\mathbf{X}} = \mathbf{A}\mathbf{X} + \mathbf{B}\mathbf{U} \quad (5.33)$$

$$\mathbf{Y} = \mathbf{C}\mathbf{X} \quad (5.34)$$

where

$$\mathbf{A} = \begin{bmatrix} 0 & 0 & a_{13} & a_{14} & 0 \\ 0 & 0 & a_{23} & 0 & a_{25} \\ 0 & 0 & a_{33} & 0 & 0 \\ 0 & 0 & a_{43} & a_{44} & a_{45} \\ 0 & 0 & a_{53} & a_{54} & a_{55} \end{bmatrix} \quad (5.35)$$

$$\mathbf{B} = \begin{bmatrix} b_{11} & 0 & b_{13} & 0 \\ 0 & b_{22} & 0 & b_{14} \\ b_{31} & b_{32} & b_{33} & 0 \\ b_{41} & b_{42} & b_{43} & 0 \\ b_{51} & b_{52} & b_{53} & b_{54} \end{bmatrix} \quad (5.36)$$

$$\mathbf{C} = \begin{bmatrix} c_{11} & c_{12} & 0 & 0 & 0 \\ 0 & 0 & 0 & 1 & 1 \end{bmatrix} \quad (5.37)$$

## 5.9 Summary

The CVT variator shows a lot of interactions between mechanical parts and hydraulics parts. For example, a variation of the primary pressure changes the primary clamping force. The equilibrium between the primary and the secondary clamping forces is affected. The primary and the secondary movable sheaves move slightly. These mechanical movements vary the hydraulic volumes and then affect the two pressures. Using the hydraulic continuity equation, the rate of change of the pressure was defined.

It was found experimentally that the two servo pumps can be modeled by a second order transfer function if the servo motor is used in speed control mode. Then, the dynamics of the primary and the secondary flows were derived.

The shifting behavior of the variator is described by a linear relation between the rate of change of the ratio and the logarithm of the primary and the secondary clamping force (pressure) ratio.

The variator dynamics were defined by the dynamics of three bodies: the intermediate element, the primary and the secondary pulleys. The dynamics of the pulleys are defined by the torque difference that acts on each pulley, the intermediate element dynamics is given by the friction forces involved in the system.

Using the new slip synthesis developed in *Section 3.2*, a complete model of the variator was derived and linearized around a working point.

## Chapter 6

# Simulation and experiment comparisons

In order to verify the low and high level models described in the two previous chapter (*Chapter 4* and *5* respectively), the simulations results are compared with experimental data. The validation indicates the level of reliability and the limitations of these models. Experiments were performed on a test bench composed of an electric motor, a CVT variator with an involute chain and a dynamo to simulate the load.

The first section briefly describes the test bench used for measuring the primary pulley position and the chain speed. The second section compares results of simulations with the low level model and experimental results. Finally, the third section compares some dynamic simulations with experimental data.

### 6.1 Test bench

The test bench (Figure 6.1) is composed of an  $55kW$  electric motor, a CVT variator, a  $30mm$  involute chain, a  $91kW$  dynamo and two servo pumps composed of a  $400W$  servo motor and a  $0.88cc$  bidirectional external gear pump .

Additional sensors are placed to measure the pulley speeds  $\omega_x$  (max speed  $6000rpm$ ) and torques  $T_x$  (max torque  $100Nm$ ), the pressures  $P_x$ , the flows that enter or exist the pulley  $Q_x$ , the primary pulley position  $z_p$  and finally the chain speed  $v_{ch}$ .

All sensors are connected to a dSPACE system to control the test rig (pulley pressures, speed ratio, input torque, electric motor rotation speed and safety software). A computer is used as a human interface for an easy use of the test bench.

Further descriptions of the testing equipment is given in *Appendix G*.

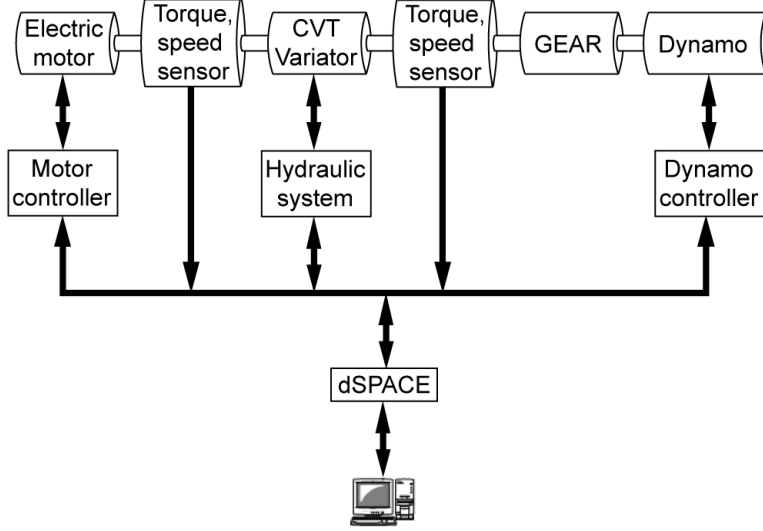


Figure 6.1: Test bench layout with a 55kW electric motor , torque and speed sensors, a variator with an involute chain and a 91kW dynamo

### 6.1.1 Pulley radius measurement

The pulley radius can easily be measured if it is assumed that pulleys or chain deformations are negligible. In reality, elastic deformations could be important. To accurately estimate the pulley radius, the measurement of the pulley radius has to be compensated for temperature changes and for changing clamping force levels (Bonsen (2006)). The part of the variator will expand with the temperature and then influence the pulley radius measurement. The clamping forces have an effect on the pulley, chain and housing elastic deformations.

The pulley radius  $R_x$  is measured at zero-load ratio at different primary pulley position  $z_p$ , temperature  $T$  and secondary clamping force  $F_s$ .

$$R_x = f(z_p, F_s, T) \quad (6.1)$$

The zero-load ratio is equivalent to the speed ratio without load. It is considered that the intermediate element does not slip and the primary and the secondary radius,  $R_p$  and  $R_s$  respectively, are calculated using the chain speed  $v_{ch}$  and the pulley rotation speed  $\omega_x$ .

$$R_p = \frac{v_{ch}}{\omega_p} \quad (6.2)$$

$$R_s = \frac{v_{ch}}{\omega_s} \quad (6.3)$$

### 6.1.2 Chain speed measurement

The chain speed is measured via the frequency detection of the pins. The chain speed is a function of the frequency detection  $f_{det}$  and the pitch of the chain  $pitch$ :

$$v_{ch} = f_{det} pitch \quad (6.4)$$

In this work, the detection of the frequency uses a proximity sensor. In order to keep a constant gap between the sensor and the pin, a sensor holder following the chain movement was developed and is shown in Figure 6.2.

Figure 6.2(a) shows all the movements needed to follow the chain. The measurement system is free in rotation and along the Z axis, (I) and (II) respectively. To take into account the misalignment, the rotation around the Y axis is integrated into the system (III). The chain vibrations in Y direction are also taken into account (IV). The chain is in contact with the support and pulls the system (Figure 6.2(b)).

## 6.2 Low level model

In order to verify the predictions of the low level model described in *Chapter 4*, the simulation results are compared with experimental data. This validation is decomposed in two steps. The first step is the prediction of the primary clamping force, and the second step is the simulation of pulley slip and traction coefficient.

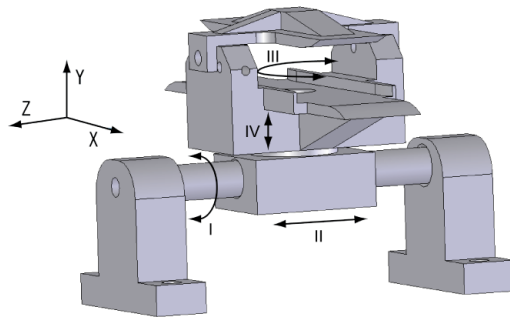
### 6.2.1 Clamping force

Figure 6.3 presents a comparison of the simulated and measured primary clamping force for an input torque  $T_p$  equal to  $20Nm$  and for different speed ratio. The inputs of the model are the geometrical ratio, the input torque and the secondary clamping force. The secondary clamping force is calculated with the standard clamping force strategy. The prediction of the primary clamping force is almost always within 5%.

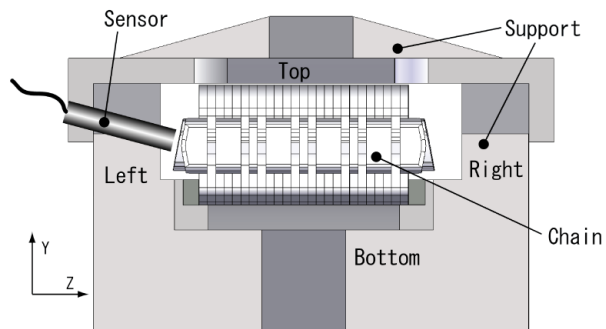
A general offset is observed between simulations and experiments. Losses, as for example bearing losses, losses due to the miss-alignment and due the friction between each element of the chain are not considered in the model. The tolerance between the pulleys and the shaft are including in the pulley deformation but as a rigid deformation. In reality, the contact point between the pulley and the shaft is deformed and depends on the clamping forces. Also, the pin bending is not included in the model.

### 6.2.2 Slip and traction coefficient

During the slip and traction coefficient experiments, the secondary clamping force is constant at  $F_s = 2kN$ , the geometrical ratio is fixed in UD ratio



(a) Degrees of freedom of the chain speed measure system



(b) Proximity sensor and chain guides of the chain speed measurement system

*Figure 6.2: Chain speed measurement system*



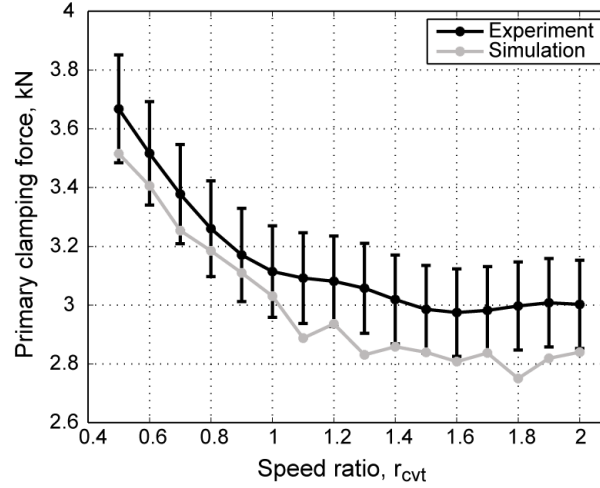


Figure 6.3: Simulation of the primary clamping force and experimental data at different speed ratio for an input torque  $T_p = 20Nm$

and the primary torque is slowly increased. Figure 6.4 shows these experimental measurements in comparison with the simulation data obtained by the low level model. The inputs of the model are the secondary clamping force  $F_s$ , the primary torque  $T_p$  and the two pulleys radius  $R_x$ . Figure 6.5 shows similar experiments in OD ratio.

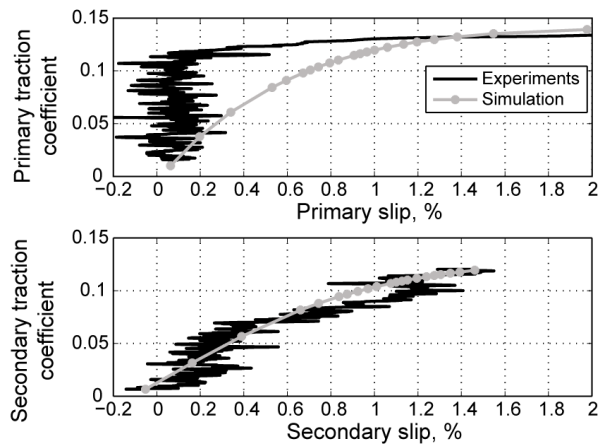
The model shows good correlation with experiments, except for the traction curve of the primary pulley. The experiment shows a steeper slope at the start of the curve. The model uses an exponential law to define the friction coefficient <sup>1</sup>. More precise models may be needed to obtain better results for the traction curve. The contact point between the pins of the chain and the pulley sheaves may be a mixed EHL/Metal-Metal contact point (Carbone et al. (2008)). Also, it was observed that the clearance model between the shaft and the pulleys plays an important role in the traction curve.

The low level model only models the chain efficiency (Figure 6.4(b)) and does not consider other losses in the system. These differences may explain the offset between the experimental data and the simulation results of the variator efficiency.

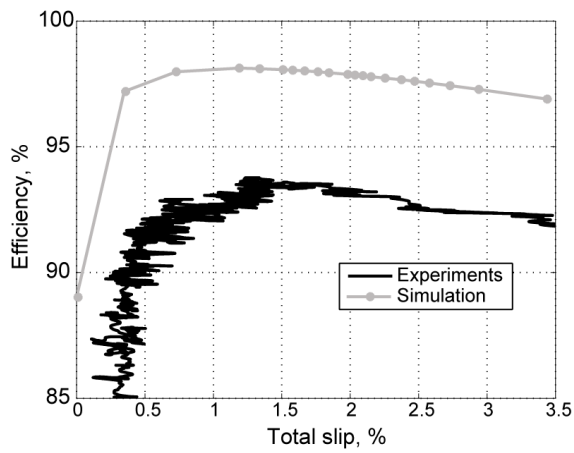
### 6.3 High level model

The validation of the high level model presented in *Chapter 5* is decomposed in two steps: firstly the geometrical ratio, hydraulics and servo pump models validation, and second the slip dynamics validation.

<sup>1</sup>The two parameters  $\mu_0$  and  $v_0$  of the friction exponential law (4.25) were chosen to match the experiments as closely as possible. These values depend on the speed ratio and on the secondary clamping force



(a) Primary and secondary traction coefficient as a function of the primary and secondary slip respectively



(b) Variator efficiency as a function of the total slip

Figure 6.4: Comparison of traction curve and efficiency between experiments and simulations with the low level model, UD,  $F_s = 2kN$

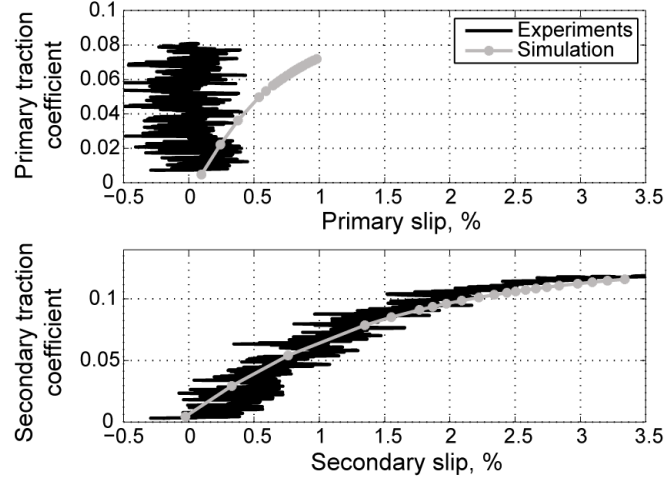


Figure 6.5: Primary and secondary traction curve as a function of the primary and secondary slip respectively in OD, with a secondary clamping force  $F_s = 3.7kN$

### 6.3.1 Geometrical model validation

For these experiments, a decentralized controller that neglects the coupling was design to control the speed ratio and the secondary clamping force. (Figure 6.6, Appendix H).

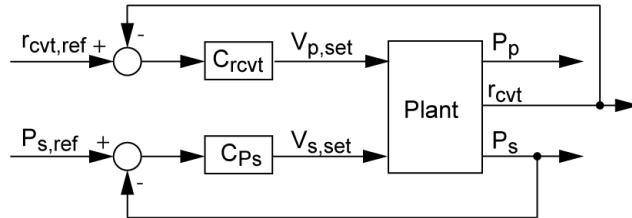


Figure 6.6: For the validation of the geometrical ratio, the pressure and actuator dynamics, the speed ratio and the secondary pressure are controlled with a decentralized controller neglecting coupling effects

During step ratio demand, the primary speed is fixed at  $1000rpm$ , the secondary clamping force is controlled at  $1MPa$ .

Figure 6.7 depicts the good correlation between simulations and experiments. The ratio starts from 1; then a shift down to a ratio equal to 0.6 is followed by a shift up to a ratio 1.5 and finally finished down to a ratio equal to 1 (Figure 6.7(a)).

Figure 6.7(b) shows the primary and the secondary pressures. During the shift down, the primary pressure decreases, which disturbs the equilibrium of the pulley forces and causing the variator to shift down. When the ratio reaches the set value, the primary pressure is constant. The same behavior is observed for up shifting, but this time the primary pressure rises. The

secondary pressure remains constant in these experiments, but some perturbations due to the ratio change can be observed (interactions, *Section 5.2*).

Figure 6.7(c) shows the primary and the secondary pulley flows. A negative flow means that the flow is going out of the pulley, whereas a positive sign means that the flow is going into the pulley. During down shifting, the primary flow is transferred from the primary pulley to the secondary pulley which results in a rising of the secondary flow. The opposite behavior can be seen during up shifting.

### 6.3.2 Variator model

During the validation of the mechanical model of the variator (*Section 5.8*), the variator is controlled using the strategy described in *Chapter 7*.

Figure 6.8 depicts experimental and simulation results for a constant speed ratio  $r_{cvt} = 0.5$  during a change in torque. In general, simulations and experiments give good correlations.

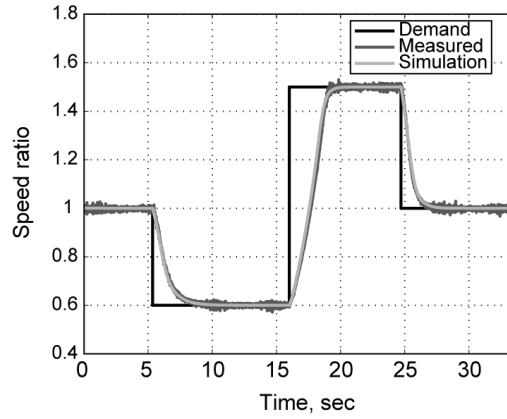
For a variation of the torque, the secondary clamping force strategy adapts the set point of the secondary clamping force to avoid slip of the chain (Figure 6.8(b)). The standard secondary clamping force strategy is used (30% over clamp). These changes of torque and secondary clamping force perturb the speed ratio, the chain speed (Figure 6.8(a)), the primary and the secondary slip as depict in Figure 6.8(c). The speed ratio controller reacts by modifying the primary clamping force in order to keep the speed ratio constant (Figure 6.8(b)).

The simulation of the pulley radius (or pulley sheave displacement) may slightly differ from the experiments and a small offset is present between the experiment and the simulation of the chain speed (Figure 6.8(a)).

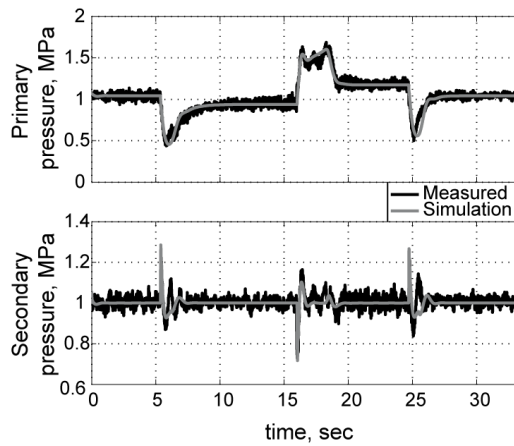
*Section 6.2.2* discussed that in low ratio, the simulation of the primary traction curve had a lower slope than the measured one. This observation explains the offset between the simulation and the experiments for the primary slip and also the dynamic differences for the primary and secondary slips (Figure 6.8(c)). To account for these discrepancies, the traction curves can be replaced by an approximation of the experimental data and very good results are obtained as shown in Figure B.5. During this experiment, the secondary clamping force and the primary movable pulley are constant while the load is increasing. Slip rises with load until instability is reached.

## 6.4 Summary

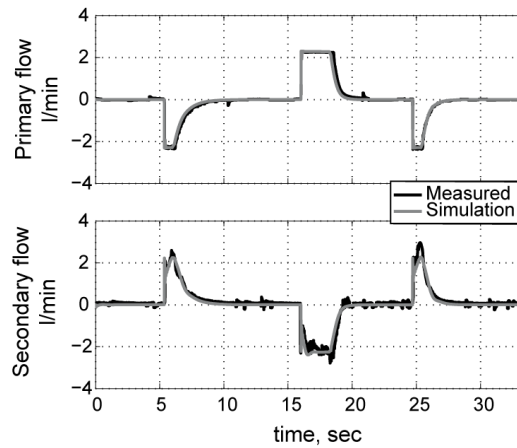
A test bench with an electric motor, a variator with an involute chain, a dynamo and a hydraulic system which two servo pumps were used for the validation of the low and high level models, *Chapter 4* and *Chapter 5* respectively. This test rig was supplemented by a displacement sensor to measure the position of the primary movable pulley sheave and by a system to measure the chain speed.



(a) Measurement and simulation of the speed ratio during a speed ratio step reference



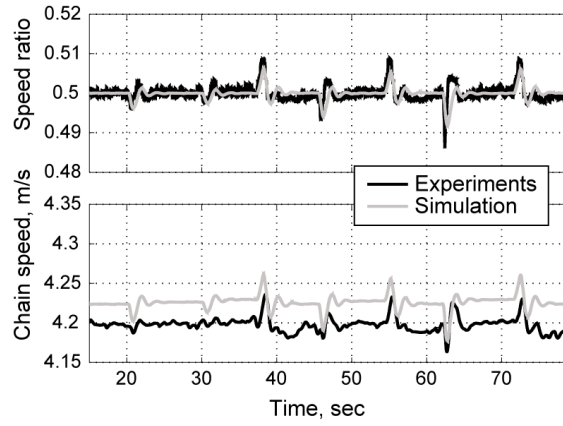
(b) Primary and secondary pulley pressures during a speed ratio step reference



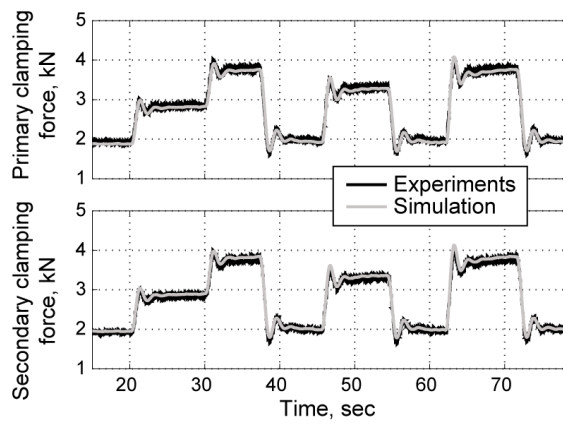
(c) Primary and secondary pulley flow during a speed ratio step reference

Figure 6.7: Validation of the geometrical ratio and hydraulic models

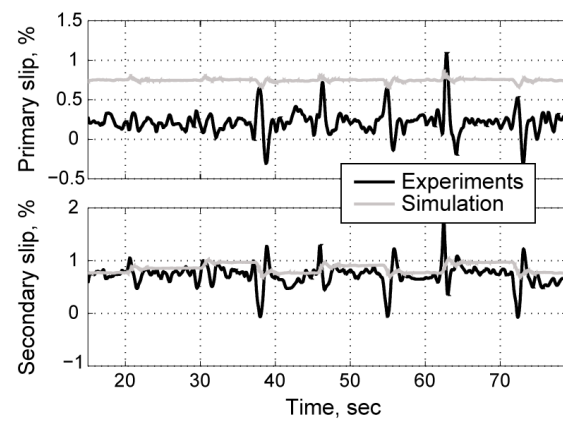
## CHAPTER 6. SIMULATION AND EXPERIMENT COMPARISONS



(a) Speed ratio and chain speed



(b) Primary and secondary clamping force



(c) Primary and secondary slip

Figure 6.8: Validation of the variator model considering the slip of each pulley and the chain dynamics during a torque disturbance

In general, good correlations between the low model predictions and experiments were observed. The prediction of the clamping force shows good results, but a general offset between simulation results and experiments is observed. The low model does not consider all the losses in the system as for examples: bearing losses, losses due the miss-alignment or losses between each part of the chain. Also pin bending is not considered. It is believed that neglect of these effects is responsible for the observed differences. The predictions of the primary slip and traction coefficient for low ratio diverge from the experiments. A more precise model of the traction coefficient is needed to obtain better results. Also, the taction curve coefficient are strongly modified by the clearance model between the pulleys and the shaft. Significant model improvements are therefore required in order to predict the traction / slip behaviors at the primary and secondary pulleys correctly.

The high level gives very good dynamic predictions for the hydraulic pressure, the hydraulic flow, the chain speed, the clamping forces, the slip and speed ratio. The absolute value of the primary slip diverges from the experiments. The high level model is affected by the divergence of the traction curve prediction from the low level model. If the real traction curves is used, the high level model shows really good agreement with experimental data.





## Chapter 7

# Variator control

The control of the CVT variator is important. For example, let's consider that the variator is in equilibrium. An increase of the resisting torque level affects the equilibrium and the variator shifts down if the actual ratio of the primary and the secondary clamping forces remains the same. The variator stabilizes at a lower speed ratio. To keep the ratio constant, the primary clamping force should increase. On the other hand, if secondary clamping force is too small, macro-slip occurs and damages the variator. This chapter describes a control strategy for the variator based on controlling the pulley flows with a pole placement method and the pulley pressure with an input-output feedback linearization.

The chapter is structured as follows. Firstly the state of the art is presented. Secondly, the actuator flow control is discussed followed by the pressure control using a input-output feedback linearization. The fourth section defines the speed ratio and the secondary clamping force control. Finally, the last section gives some results obtained with the proposed controller.

### 7.1 State of the art

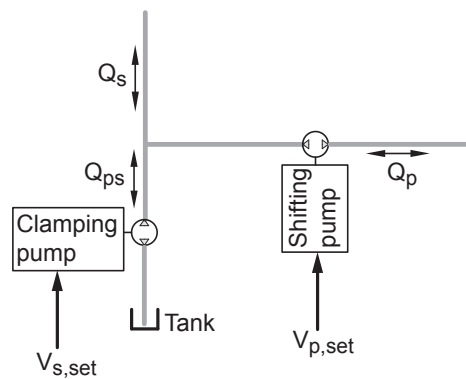
In current control strategies, the primary clamping force controls the speed ratio while the secondary clamping force is set to avoid slip of the intermediate element.

Abromeit & Wilkinson (1983) control the secondary clamping force with the secondary pressure and control the speed ratio by controlling the oil flow into the primary pulley. Wade (1984) controls the variator by controlling the two pressures simultaneously. The primary pressure controller is augmented by a ratio controller to achieve the desired ratio response. Spijker (1994) implemented an adaptive control to control both the secondary clamping force and the speed ratio. The latter is controlled through the velocity of the primary sheave. Sato et al. (1996) control the secondary pressure with PI algorithm synthesis and a feedforward. The secondary clamping force reference is set to avoid slip of the belt. The primary pressure is directly controlled to obtain the desired speed ratio. For both pressures, he implemented a PID law

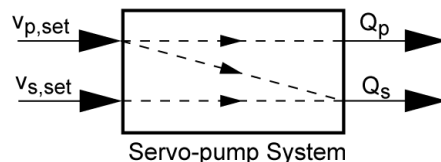
with feedforward. Kim et al. (1996) study the speed ratio control response for sinusoidal input of the speed ratio in case of PID, LQG/LTR and fuzzy control algorithms. PID and fuzzy controllers showed better responses than LQG/LTR. The poor response of this last controller is explained by the fact that the transfer functions obtained do not represent the system characteristics accurately due to the inherent strong nonlinearities of the CVT system. Kim et al. (1996) and Kim & Vachtsevanos (2000) introduce a fuzzy synthesis to control the speed ratio. Additionally, Adachi et al. (1999) propose a robust control, van der Laan & Luh (1999) use a feedback linearization with PID to control the speed ratio and a PID for the secondary clamping force. Vroemen et al. (2000) present a ratio control which includes a PI controller for the primary pressure set point, and a proportional action plus feedforward for the secondary set point pressure.

## 7.2 Actuator flow control

The flow that enters or exists the two pulley volumes are two of the inputs available to modify the pressure (5.8 in *Section 5.4*). The flow is considered to be proportional to the servo motor speed (*Section 5.3*) and it is proposed to use the shifting pump and the clamping pump to control directly the primary flow  $Q_p$  and the secondary flow  $Q_s$  respectively (Figure 7.1(a)).



(a) Servo pump hydraulic system without the variator



(b) Coupling between the shifting pump and the clamping pump

Figure 7.1: Servo pump actuator interactions

### 7.2.1 Control problem

With refer once to *Section 5.3.1*, the two servo pumps are controlled in speed. The two signal  $V_{p,set}$  and  $V_{s,set}$  are the voltage to set the desired rotation speed of the servo motors. If no leakage is considered, a change of the second input  $V_{s,set}$  affects only the secondary flow  $Q_s$ . A variation of the voltage input  $V_{p,set}$  influences the shifting pump speed, influences the primary flow  $Q_p$  and finally disturbs the secondary flow (Figure 7.1(b)). This interaction is not suitable and the system should be decoupled (first constraint).

The actuators have a certain dynamics. These dynamics can become a disadvantage especially if the dynamics are slow compared to the entire system. It can be of interest to increase the bandwidth of the two servo pumps in order to obtain a response fast enough compared to the entire system and then the actuator dynamics can be neglected (second constraint).

In order to fulfil these two constraints, a pole placement synthesis is proposed.

### 7.2.2 Flow control design with pole placement

The pole placement method is a simple but powerful technique for solving the control problem. The poles of the closed-loop system can be placed in arbitrary locations using a constant linear combination of the state variables (Vaccaro (1995), Chen (2004)).

The pole placement needs the knowledge of the states. With reference to *Section 5.3.2* the states are  $\mathbf{X}_{act} = [ Q_p \ \dot{Q}_p \ Q_{ps} \ \dot{Q}_{ps} ]^T$ . In a car, flows are not measured; furthermore their time rates of change are difficult to measure. An observer is needed to estimate them. Basically, the observer is identical to the state-space model of the the servo-pump model (5.4). The description of the observer is outlined of this section.

Figure 7.2 depicts the block diagram of the servo pump flow control. The vector  $\mathbf{U}_{act} = [ V_{p,set} \ V_{s,set} ]^T$  is the input voltage of the servo amplifier used to set the rotation speed of the servo pumps; the vector  $\mathbf{W}_{act} = [ \omega_{p,p} \ \omega_{p,s} ]$  is the measured rotation speed of the motors given by the servo amplifier (no additional sensors are used); the vector  $\mathbf{X}_{act}$  is the state vector, the output vector  $\mathbf{Y}_{act} = [ Q_p \ Q_s ]^T$  consists of the primary and the secondary flows, finally  $\mathbf{Y}_{act,ref} = [ Q_{p,ref} \ Q_{s,ref} ]^T$  is the reference vector for the primary and secondary flows.

The placement of the closed-loop poles determines the two vector gains  $L_2$  and  $l_1$  (Figure 7.2). The poles were chosen so that the dynamics of the actuators are fast enough compared to the rest of the system.

Figure 7.3 shows the Bode diagram of each input to each output of the servo pump actuators in open loop and flow control mode. As explained at the beginning of the section, the primary flow affects the secondary flow. This effect is represented in the bode diagram open loop from  $Q_{p,ref}$  to  $Q_s$  (Figure 7.3, lower left plot). As can be seen in the same Bode diagram, the pole placement decouples the system and increases the bandwidth by almost a factor 10. With

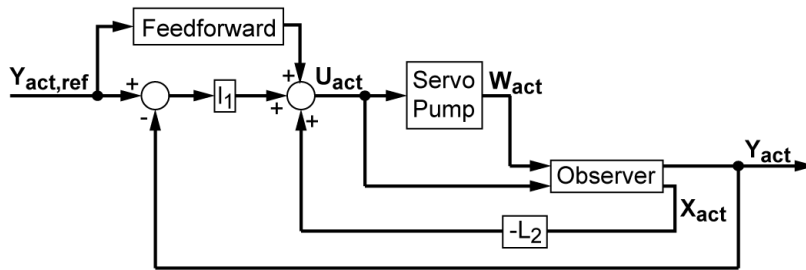


Figure 7.2: Bloc diagram of the servo pump flow control design with pole placement

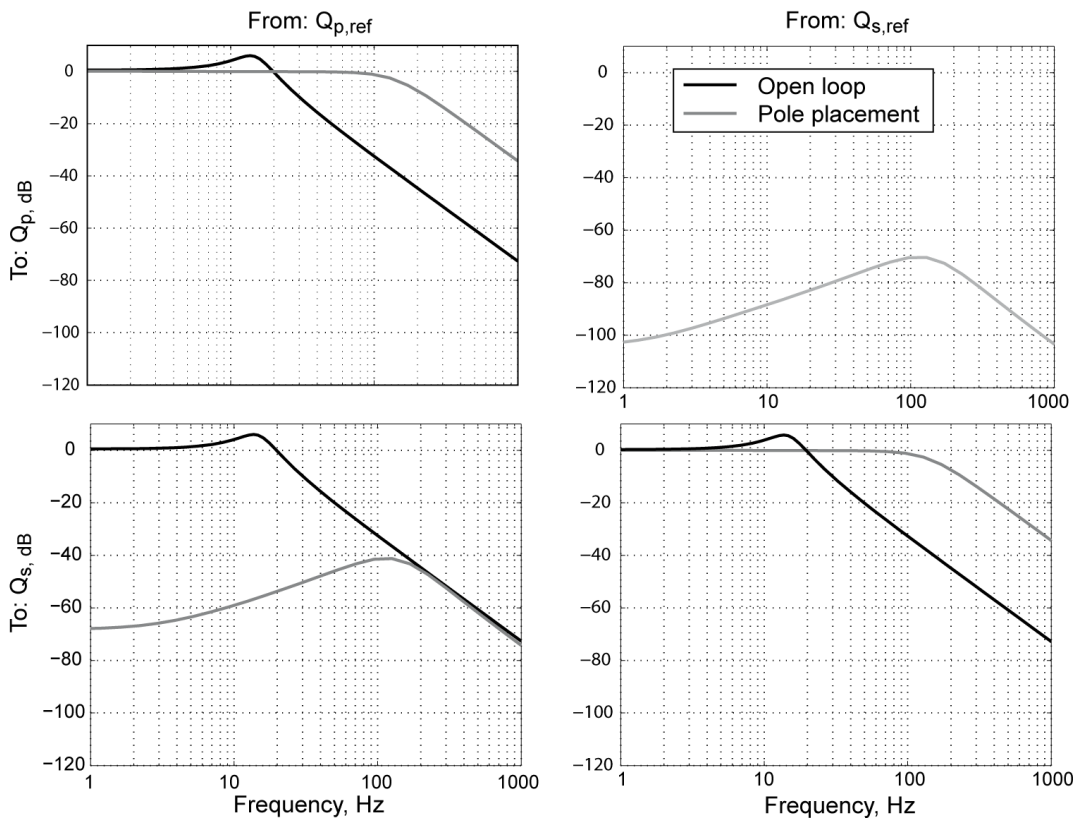


Figure 7.3: Bode diagram of the flow control without flow control and with flow control

this flow control algorithm the actuator dynamics are fast enough compared to the entire system and can be neglected.

### 7.2.3 Design validation of the flow control

Figure 7.4 shows experimental response of the actuator flow control during primary flow step excitation while the secondary flow reference is constant. When the primary flow reference goes up, the shifting pump speed rises to follow the reference and decreases the secondary flow due the coupling of the system (*Section 5.2.1*). As the secondary flow reference is constant, the clamping pump accelerates (Figure 7.4(b)) to keep the secondary flow at the reference value and the system is decoupled. When the primary flow reference is going down, the opposite effect explains the decrease of the motor rotational speed.

The flow control presented in this section increases the bandwidth and decouples the actuators and so that because of its significantly higher dynamics, can then be neglected. Now, the flow that enters or exits each pulley can be considered as input to control the primary and the secondary pressure.

## 7.3 Pressure control

The correct control of the primary and the secondary pressures is important. The primary pressure is used to control the speed ratio and the secondary pressure gives a line pressure to avoid lip of the intermediate element.

### 7.3.1 Pressure control constraint

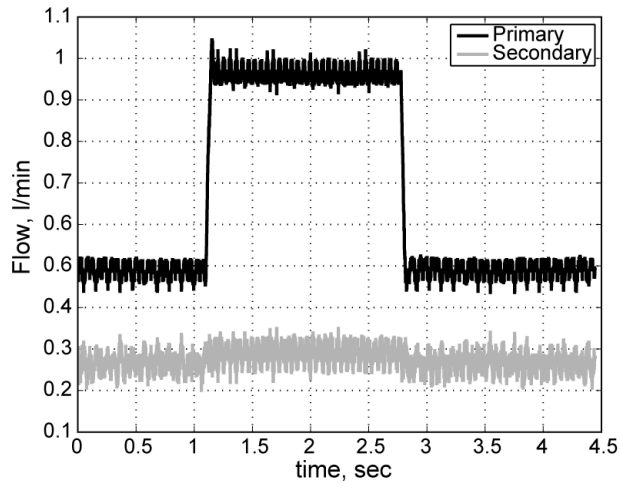
Refer to the actuator control presented in *Section 7.2*, the actuators are neglected and the flow that enters or exists the two pulleys  $Q_x$  are considered as the inputs of a new plant. The position and the velocity of the pulley sheaves,  $z_x$  and  $\dot{z}_x$  respectively, are considered as perturbations and the outputs are the pulley pressures  $P_x$  (Figure 7.5).

The pressure control should achieve a decoupling of pressures and pulley sheaves positions/speeds; furthermore it should linearize the plant.

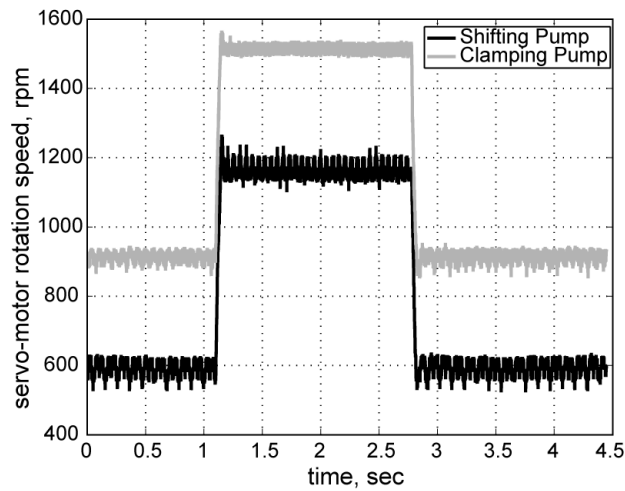
It is proposed to used an input-output feedback linearization to both linearize the two pressures and to decouple the MIMO system. Then a linear control is used to control the two pressures.

### 7.3.2 Input-Output feedback linearization design

The input-output feedback linearization (IOFL) consists in finding a direct relation between the output and the control input. Each output is differentiated until a direct relation is found (Slotine & Li (1991)). The input vector is the primary and the secondary flow  $\mathbf{U}_{\text{CVT}} = [ Q_p \quad Q_s ]^T$ , the state and the output vectors are the two pulleys pressures  $\mathbf{X}_{\text{CVT}} = \mathbf{Y}_{\text{CVT}} = [ P_p \quad P_s ]^T$ .



(a) Primary and secondary flows



(b) Shifting and clamping pump rotation speeds

Figure 7.4: Experimental data showing the decoupling of the primary and the secondary flows during step response of the primary flow while the secondary flow reference is constant

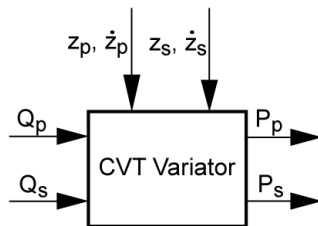


Figure 7.5: Coupling of the pulley pressure with the pulley flow and the speed ratio

The method is applied to both, the primary and the secondary pressures  $P_p$  and  $P_s$  respectively. The first derivative of the output  $Y_{CVT,x}$  corresponds to the pressure dynamics and a direct relation with the input  $U_{CVT,x} = Q_x$  appears.

$$\begin{aligned} Y_{CVT,x} &= P_x \\ \dot{Y}_{CVT,x} &= \dot{P}_x = \frac{\beta_e}{V_{x,0} + A_x z_x} Q_x - \frac{A_x \dot{z}_x \beta_e}{V_{x,0} + A_x z_x} \end{aligned} \quad (7.1)$$

If the input  $Q_x$  is chosen as the inverse of (7.1) then,

$$Q_x = \frac{V_{x,0} + A_x z_s}{\beta_e} \nu_x + A_x \dot{z}_x \quad (7.2)$$

where  $\nu_x$  is an input to be specified. The resulting dynamics is linear.

$$\dot{P}_x = \nu_x \quad (7.3)$$

The control law for the primary and secondary pulleys (7.2) has two effects: the decoupling and the linearization of the plant. The input to output relation is equivalent to an integrator (Figure 7.6). The inputs  $\nu_1$  and  $\nu_2$  control the two outputs, the primary pressure and the secondary pressure  $P_p$  and  $P_s$  respectively.

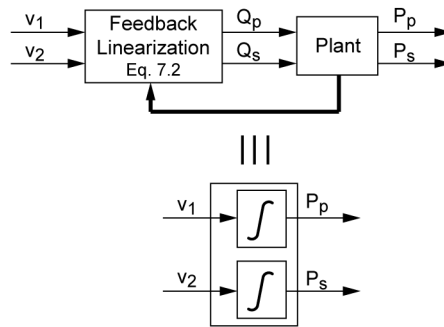


Figure 7.6: With the input-output feedback linearization, the relation between the input and the output becomes, theoretically, equivalent to an integrator and also decouples the plant

### 7.3.3 Pressure linear control design

The input-output feedback linearization defines a new MIMO system with the input vector  $\mathbf{U} = [\nu_1 \ \nu_2]^T$  and the two pulley pressures as outputs  $\mathbf{Y} = [P_p \ P_s]^T$ . The relation between the inputs and the outputs are linear and theoretically, a proportional gain is sufficient and the input law  $\nu_x$  can be written

$$\nu_x = K_{Px} \tilde{P}_{x,e} \quad (7.4)$$

with  $\tilde{P}_{x,e} = P_{x,ref} - P_x$  the pressure error and  $K_{Px}$  a strictly positive constant. The resulting closed-loop dynamics become

$$\dot{\tilde{P}}_{x,e} + K_{Px} \tilde{P}_{x,e} = 0 \quad (7.5)$$

When  $t \rightarrow \infty$ , the tracking error  $\tilde{P}_{x,e} \rightarrow 0$ . Considering (7.2) and (7.4), the actual pulley flow is given by the following nonlinear equation:

$$Q_x = \frac{v_{x,0} + A_x z_s}{\beta_e} K_{Px} \tilde{P}_{x,e} + A_x \dot{z}_x \quad (7.6)$$

The second term compensates the variation of the volume during shifting; the first term is used to raise the pressure according to the desired linear dynamics (7.5).

Figure 7.7 summarizes the control structure of the primary and the secondary pressure.  $P_{x,ref}$  is the pressure reference and  $P_x$  is the measured pressure. If the model contains all the dynamics of the plant, a proportional gain is sufficient to guaranty stability and good tracking. Usually, models are simplified and modeling errors always exists. Therefore in practice, the control law  $C_x$  should include an integral term.

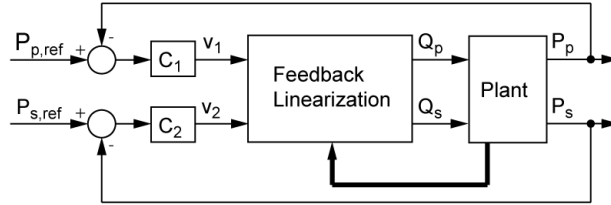


Figure 7.7: Primary and secondary pressure control design with a feedback linearization and linear control design

The pressure control defines a new MIMO system as shown in Figure 7.8. The inputs are the primary and the secondary pulley reference pressures  $P_{p,ref}$  and  $P_{s,ref}$  respectively, the output is the speed ratio  $r_{cvt}$ .

Now the primary and the secondary pressures (or primary and secondary clamping forces) can be correctly chosen to control the variator.

## 7.4 Ratio and secondary clamping force control

With the control law of the two pulley pressures presented in *Section 7.3*, the two pressures are considered to be correctly controlled.

In usual CVT control, the control of the variator consists of controlling the speed ratio and setting the correct secondary clamping force to avoid slip of the intermediate element (Figure 7.9).



## 7.4. RATIO AND SECONDARY CLAMPING FORCE CONTROL

89

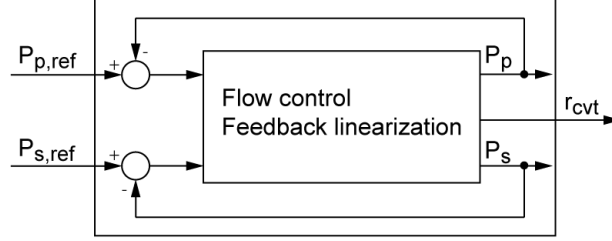


Figure 7.8: The feedback linearization and the linear control of the pulley pressures define a new plant

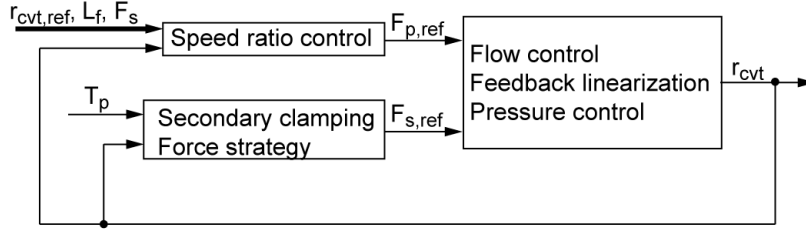


Figure 7.9: Speed ratio and secondary clamping force control design

### 7.4.1 Secondary clamping force control

The secondary clamping force depends on the speed ratio and on the primary torque. To avoid slip due to unknown perturbations, the intermediate element is usually 30% over clamped. This over clamp is called safety factor  $S_f$ . The secondary clamping force is usually given by:

$$F_{s,ref} = \frac{\cos \beta}{2\mu_0} \frac{T_p}{R_p} S_f \quad (7.7)$$

Where  $\mu_0$  is the friction coefficient,  $T_p$  is the primary torque and  $R_p$  is the primary radius that depends on the geometrical ratio. In a car, the primary torque is not measured but estimated using the throttle angle and the engine map. The primary radius is estimated using the speed ratio and the length of the intermediate element (4.5).

### 7.4.2 Speed ratio control design

The speed ratio controller aims of controlling the speed ratio of the variator with the primary clamping force. Despite the non-linearity of the plant, a PI controller with feedforward is proposed.

$$F_{p,ref} = \left( K_{p,Fp} + \frac{K_{i,Fp}}{s} \right) \tilde{r}_{cvt} + K_{pKs} (r_{cvt}, F_s, L_f) \quad (7.8)$$

where  $\tilde{r}_{cvt} = r_{cvt,ref} - r_{cvt}$  is the error between the speed ratio reference  $r_{cvt,ref}$  and the measured speed ratio  $r_{cvt}$ . The first term consist of a PI controller, and the second term is a feedforward. This feedforward is defined by the ratio of the primary and the secondary clamping force. It depends on the speed ratio  $r_{cvt}$ , on the secondary clamping force  $F_s$  and on the load factor  $L_f$ . The load factor is defined by the primary torque  $T_p$  and the maximum theoretical torque  $T_{max}$  possible to transmit ( $S_f = 1$ ).

$$L_f = \frac{T_p}{T_{max}} \quad (7.9)$$

$$T_{max} = \frac{2\mu}{\cos \beta} R_p F_s \quad (7.10)$$

Figure 7.10 summarizes the speed ratio control law. The secondary clamping force  $F_s$ , the primary torque  $T_p$  and the secondary torque  $T_s$  are considered as perturbations of the system.

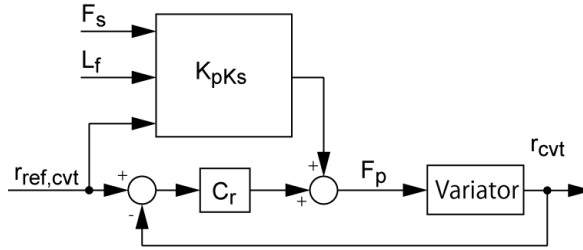


Figure 7.10: Linear control design of the speed ratio

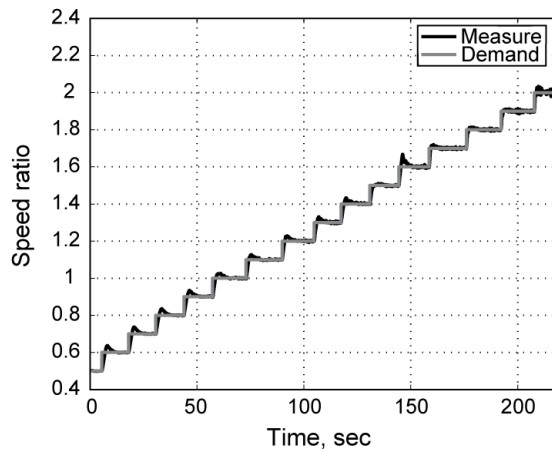
## 7.5 Validation of the variator control design

To prove the control concept, the controllers presented in the previous sections were implemented in simulations and in a test bench

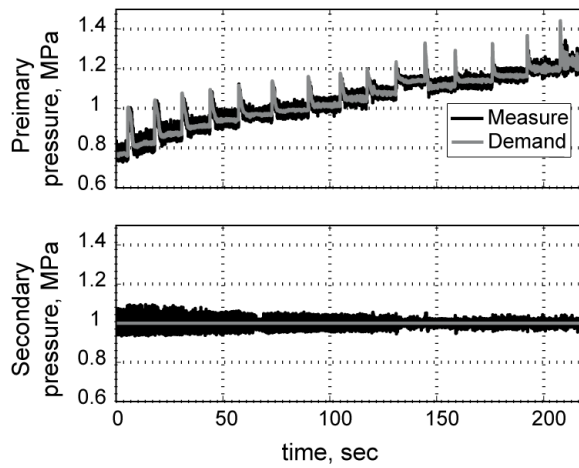
Figure 7.11 depicts experimental response of the speed ratio and pulley pressure during step response of the speed ratio. The secondary clamping force strategy is chosen to be constant to demonstrate the decoupling of the plant i.e the secondary pressure is not perturbed by both the primary clamping force and the speed ratio (Figure 7.11(b)). Also, in spite of the non-linearity of the speed ratio, the system is stable over the all span of the CVT.

Figure 7.12 depicts the variations of the speed ratio against torque perturbations. The secondary clamping force is set by the standard clamping force strategy (7.7) with a safety factor  $S_f = 1.3$  and the speed ratio is controlled at 1 : 1. When the primary torque increases, the secondary clamping force is adapted to avoid slip of the chain and the speed ratio has a tendency to shift down. The speed ratio control has to raise the primary clamping force to keep the speed ratio constant. In contrast, if the torque falls, the secondary

## 7.5. VALIDATION OF THE VARIATOR CONTROL DESIGN 91



(a) Experimentation of the speed ratio during step response



(b) Measured pressures during the speed ratio step response, the secondary clamping force is maintain constant at 1 MPa

*Figure 7.11: Speed ratio and pulley pressures during a step response of the speed ratio; the secondary clamping force is maintain constant*

clamping force is decreased and the speed ratio has the tendencies to shift up. The speed ratio controller then drops the primary clamping force to keep the speed ratio constant.

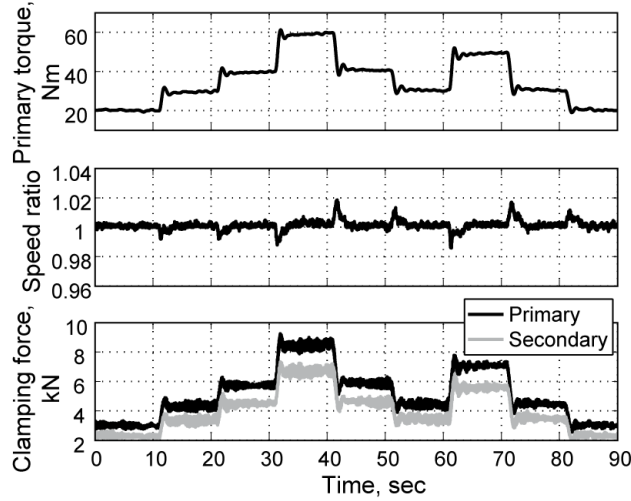


Figure 7.12: Speed ratio robustness again torque perturbations, the speed ratio is maintain constant at  $r_{cut} = 1$

## 7.6 Summary

The variator control was presented in this chapter. The controller aims at controlling the secondary clamping force to avoid slip of the intermediate element and to control the speed ratio with the primary clamping force.

It was proposed to control the actuators (the two servo pumps) in flow control. The clamping pump controls the secondary flow while the shifting pump controls the flow of the primary pulley. The MIMO system defined by the two servo pumps is coupled. It was suggested to decouple them and to increase the bandwidth of the actuators with a pole placement law.

With the flow control, the actuator dynamics can be neglected and the primary and the secondary pressures are directly controlled by the flow that enters or exists the pulleys. Here also, the MIMO system is coupled and furthermore non-linear. It was proposed to use an input-output feedback linearization to both linearize the plant and decouple the plant. As the plant is linear, a PI control is used to control the primary and the secondary pressure.

It was proposed to control the speed ratio with a PI law supplemented by a feedforward. The secondary pressure reference was defined by the standard clamping force strategy to avoid slip of the intermediate element. Despite the non-linearity of the plant, the structure proposed to control speed ratio is stable over whole speed range of the variator and rejects perturbations.

## Chapter 8

# Slip control

The variator control proposed in *Chapter 7* uses a standard secondary clamping force strategy i.e. the intermediate element is over clamped by a minimum of 30%. As it was discussed previously in *Section 2.4*, the reduction of the clamping forces is a solution to improve the efficiency of the variator. To reduce the clamping forces with safety, slip should be controlled. The new total slip synthesis introduced in *Chapter 3* is now applied to slip control.

First of all, the state of the art is presented. Secondly, the slip control problems is defined and then two control syntheses are proposed: a PI controller and a model reference adaptive control. Then the two controllers performances are compared and discussed.

### 8.1 State of the art

The primary clamping force controls the speed ratio while the secondary clamping force is adjusted to control the total slip of the variator.

The references about the slip control are limited. Pulles (2004) used a robust PI controller synthesis. Bonsen (2006) proposes a PI with gain scheduling. He only takes the speed ratio dynamics into consideration. Simons et al. (2006) improve the dynamics of the system by considering not only the speed ratio, but also the geometrical ratio dynamics. They use a LQG (Linear-Quadratic-Gaussian) feedback control synthesis to control slip. All the authors do control the geometrical ratio instead of the speed ratio and estimate the geometrical ratio through the measurement of the axial pulley sheave position (van der Meulen (2006)).

### 8.2 Slip control problem

In contrast to the different authors in this investigation, the speed ratio is controlled. The same controller that was described in the *Chapter 7* is used and it is assumed that the speed ratio is correctly controlled.

Based on the new total slip synthesis given in *Section 3.2*, the speed of the pulleys  $\omega_x$ , the chain speed  $v_{ch}$  and the pulley radiuses  $R_x$  have to be

measured to estimate slip. Figure 8.1 represents the synthesis of the control.

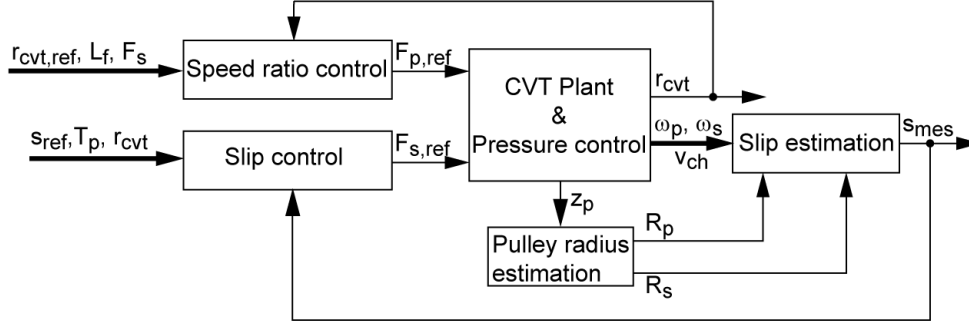


Figure 8.1: Bloc diagram of the slip and speed ratio control

The plant is nonlinear and the slip control should be stable for all the working points of the variator; it has also to reject disturbances such as those on the pulley torques and the speed ratio.

### 8.2.1 Slip control strategy

To improve the efficiency of the variator by slip control, the slip value that determines the maximum efficiency should be defined. Refer to *Section 3.5*, the peak value slightly depends on the pulley pressure and on the rotation speed. On the other hand, the maximum value of the efficiency depends on the speed ratio. The position of the peak efficiency could vary from a slip value of 1.5% in UD to a value of 2.5% in OD. The efficiency as a function of the slip is relatively flat around the peak efficiency. Therefore the same slip reference value, chosen at 2%, can be used for the all working points without affecting too much the efficiency.

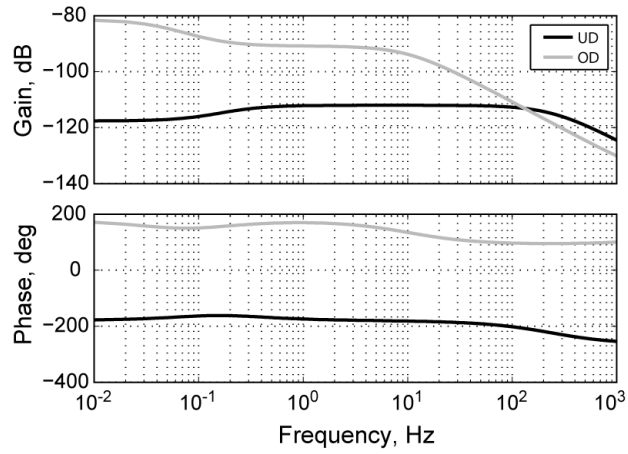
### 8.2.2 Frequency response

The slip control is controlled by the secondary clamping force  $F_s$ . The primary clamping force  $F_p$  and the pulley torques  $T_x$  are considered as disturbances. At a certain working point, the state space model of the total slip (5.33 - 5.37) can be transformed in the frequency domain to yield:

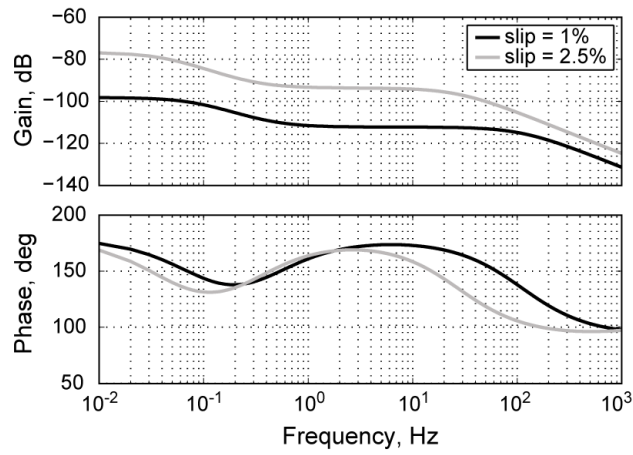
$$s_{tot} = G_s \frac{N_s(s)}{D_s(s)} F_s \quad (8.1)$$

where  $G_s$  is the gain,  $N_s(s)$  is a function of degree  $p = 2$  and  $D_s(s)$  is a function of degree  $q = 3$ .

Figure 8.2(a) depicts the frequency response of the secondary clamping force  $F_s$  to total slip  $s_{tot}$  for an input torque equal to  $T_p = 40Nm$  and a total slip  $s_{tot} = 2\%$ . Figure 8.2(b) shows the same frequency response for a speed



(a) Plant transfer function for underdrive and overdrive, with total slip  $s_{tot} = 2\%$  and total input torque  $T_p = 40Nm$



(b) Plant transfer function for different slip values, at ratio 1 : 1 and input torque  $T_p = 40Nm$

Figure 8.2: Plant transfer function of the secondary clamping force  $F_s$  to total slip  $s_{tot}$  for different working points

ratio  $r_{cvt} = 1$ , an input torque  $T_p = 40Nm$  and a total slip value of  $s_{tot} = 1\%$  and  $2.5\%$ .

Firstly a proportional-integrator (PI) is proposed. Secondly, to deal with the time variation of the plant due to the friction coefficient variations (time, temperature) a Model Reference Adaptive Control (MRAC) is proposed.

### 8.3 Slip control with PI

With reference to the transfer function of the variator slip, (8.1), the following control law is proposed:

$$F_s = \underbrace{\left( K_{p,F_s} + \frac{K_{i,F_s}}{s} \right)}_{C_s \text{ in Figure 8.3}} \tilde{s}_{tot} + F_F \quad (8.2)$$

Where  $\tilde{s}_{tot} = s_{ref} - s_{tot}$  is the slip error, the first term corresponds to the PI law and the second term is a feedforward term (Figure 8.3). The idea of the feedforward is to set the good secondary clamping force for a certain slip reference at a certain speed ratio and input torque. Two approaches are proposed for the feedforward: simple feedforward (*SFF*), mapping feedforward, (*MFF*).

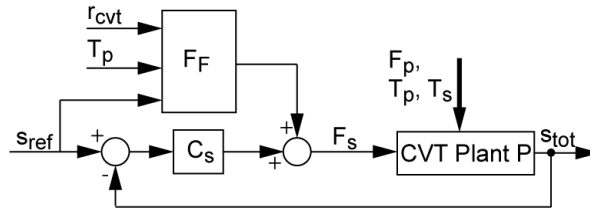


Figure 8.3: Bloc diagram for the PI law with feedforward to control slip

#### 8.3.1 Simple feedforward design

The simple feedforward considers that the needed secondary clamping force to obtain the desired slip is unknown. The standard secondary clamping force strategy described in *Section 7.4.1* is considered with a safety factor  $S_f$  equal to one. This feedforward does not need the slip reference  $s_{ref}$  as input.

$$F_F = \frac{\cos \beta_0}{2\mu_0} \frac{T_p}{R_p} \quad (8.3)$$



### 8.3.2 Mapping feedforward design

The single feedforward described in the previous section is a simple solution but not optimum as it will be seen in *Section 8.5.4*. To improve it, the mapping feedforward is proposed. The idea is to have a mapping of the secondary clamping force reference for different speed ratios, input torques and if needed different slip references. This mapping could be either based on measured data, or obtained by simulation. The low level model described in *Chapter 4* can be used to obtain this mapping. To do this, an additional loop has to be added by changing the secondary clamping force until the desired total slip is obtained. In this case, the feedforward is a function of the slip reference  $s_{ref}$ , the speed ratio  $r_{cvt}$  and the primary torque  $T_p$ .

$$F_F = f(s_{ref}, r_{cvt}, T_p) \quad (8.4)$$

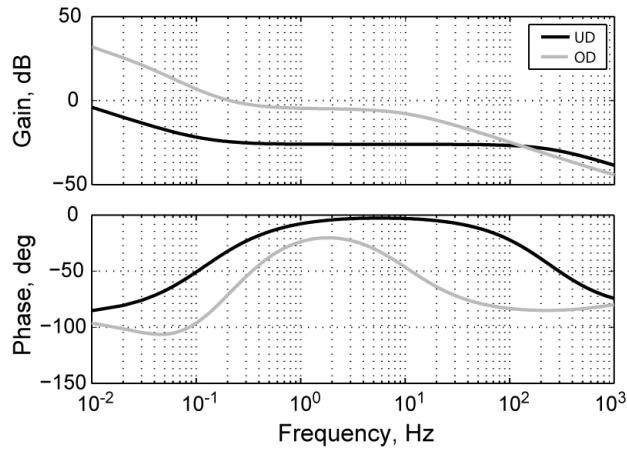
### 8.3.3 Bode diagram for the PI control

As indicated in *Section 8.2.2*, the plant is non-linear. In certain cases, a gain scheduling is required to be able to stabilize the system for all the working points. To simplify the controller synthesis, a PI controller without gain scheduling is proposed. Figure 8.4 shows the open loop frequency of the variator at different working points. The working points in underdrive and overdrive with an input torque  $T_p$  equal to  $40Nm$  and a total slip  $s_{tot}$  of 2% are represented in Figure 8.4(a) whereas Figure 8.4(b) shows the working points at a speed ratio 1 : 1, an input torque  $T_p$  equal to  $40Nm$  and total slip value  $s_{tot}$  equivalent to 1% and 2.5%.

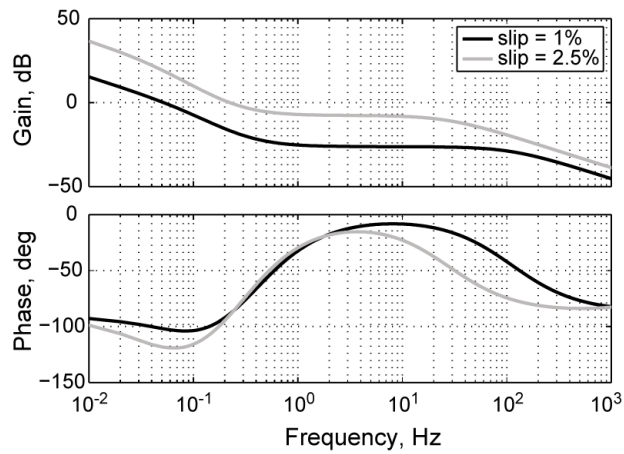
The gain margin is equivalent to  $\infty$ , the phase margin is higher than  $30deg$  these values justify the PI controller without gain scheduling from the stability point of view. After simulations and tests on the test rig, it was proven that the PI control without gain scheduling shows good stability and good perturbation rejection capabilities (*Section 8.5.2* to *Section 8.5.4*).

## 8.4 Slip control with model reference adaptive control

The basic idea of the adaptive control is to estimate the uncertain plant parameters on-line based on the signals of the measurement system, and use these estimated parameters in the control law (Sastry & Bodson (1989), Slotine & Li (1991) Ioannou & Jun (1996)). The design of autopilots for aircraft was motivation for research on adaptive control in the early 1950s. Aircraft operate over different speed and altitudes, and their dynamics are nonlinear and furthermore time varying. The nonlinear system can be controlled with a feedback control structure on which adaptive control is based. The controller structure consists of a feedback loop and a controller with adjustable gains as shown in Figure 8.5.



(a) Open loop transfer function for underdrive and overdrive, with a total slip  $s_{tot} = 2\%$  and an total input torque  $T_p = 40Nm$



(b) Open loop transfer function for different slip values, at ratio 1 : 1 and input torque  $T_p = 40Nm$

Figure 8.4: Open loop transfer function from the slip reference  $s_{ref}$  to the total slip  $s_{tot}$  for different working points

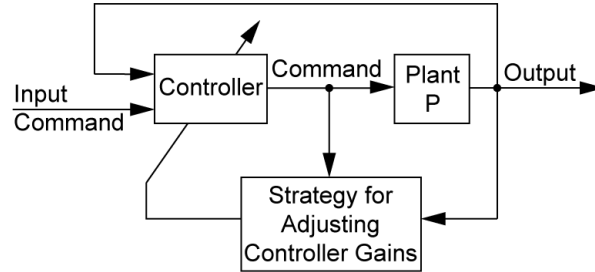


Figure 8.5: Controller structure with adjustable controller gains

Model reference adaptive control (MRAC) is the main approach to adaptive control (Figure 8.6). It is composed of four parts: a plant with unknown parameters, a reference model for specifying the desired output dynamics, a feedback control law containing adjustable parameters and finally an adaptation law for adjusting the parameters.

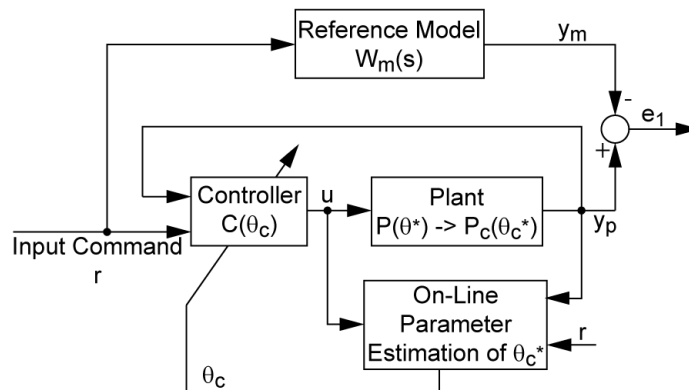


Figure 8.6: Direct model reference adaptive control

The plant is assumed to have a known structure with unknown parameters. For linear plants, this means that the number of poles and zeros are assumed to be known, but the locations are not. In the case of nonlinear plants, this implies that the structure of the dynamic equations is known, but that some parameters are not (Ioannou & Jun (1996)). A reference model is used to specify the wanted response of the adaptive control system to the external command. The controller is parameterized by a number of adjustable parameters. The controller should have perfect tracking capacity in order to allow the possibility of tracking convergence. The controller parameters should make the plant output identical to the reference model. When the parameters are not known, the adaptation mechanism will adjust the controller parameters so that perfect tracking is asymptotically achieved. The adaptation law is used to adjust the parameters in the control law. The objective of the adaptation is to make the tracking error converge to zero. The adaptation law has to guar-

antee that the control system remains stable and the tracking error converges to zero as the parameters are varied.

An adaptive control of a linear system with output feedback will be considered for the slip control with adaptive control i.e. only output measurement is used. The linear time-invariant system can be represented by the transfer function

$$W(s) = k_p \frac{N(s)}{D(s)} \quad (8.5)$$

where

$$D(s) = a_0 + a_1s + \dots + a_{q-1}s^{q-1} + s^q \quad (8.6)$$

$$N(s) = b_0 + b_1s + \dots + b_{p-1}s^{p-1} + s^p \quad (8.7)$$

The relative degree  $n^*$  of the system is  $n^* = q - p$ . The coefficient  $a_i$ ,  $b_j$  ( $i = 0, 1, \dots, q - 1$ ;  $j = 0, 1, \dots, p - 1$ ) and the gain  $k_p$  are assumed to be unknown.

The objective of the design is to determine a control law, and an associated adaptation law, so that the plant output  $y_p$  approaches asymptotically the plant reference output  $y_m$ . The output  $y_p$  is considered to be measured, but no differentiation of the output is allowed<sup>1</sup>. To achieve this design the following assumptions should be satisfied by the plant:

- The plant order  $q$  is known
- The relative degree  $q - p$  is known
- The sign of the gain  $k_p$  is known
- The plant is minimum-phase<sup>2</sup>

With reference to the slip transfer function for different working points, (8.1), the degree of the numerator  $p = 2$ , the degree of the denominator  $q = 3$ , the relative degree  $n^* = 1$ , the gain  $k_p$  is strictly negative,  $k_p < 0$ , furthermore, the plant is minimum-phase. The slip plant satisfies the assumption and the MRAC could be used.

#### 8.4.1 Slip control with MRAC

Sastry & Bodson (1989), Slotine & Li (1991), Ioannou & Jun (1996) give a control and adaptive law for linear systems with relative degree one  $n^* = 1$ . This algorithm will be applied to the slip control.

<sup>1</sup>To avoid the noise amplifications associated with numerical differentiation

<sup>2</sup>The minimum-phase plant requires that the transfer function has no zeros in the right half-plane of the complex plane

Let's define the desired performance of the plant by the following reference model

$$s_m = \frac{1}{s + a_m} s_{ref} \quad (8.8)$$

where  $a_m$  can be chosen arbitrarily but should be positive to guarantee stability. The control law is designed as (Figure 8.7)

$$\dot{\omega}_1 = F\omega_1 + gF_s, \quad \omega_1(0) = 0 \quad (8.9)$$

$$\dot{\omega}_2 = F\omega_2 + g s_{tot}, \quad \omega_2(0) = 0 \quad (8.10)$$

$$F_s = \hat{\theta}_1 \omega_1 + \hat{\theta}_2 \omega_2 + \hat{\theta}_3 s_{tot} + \hat{\theta}_4 s_{ref} + F_F \quad (8.11)$$

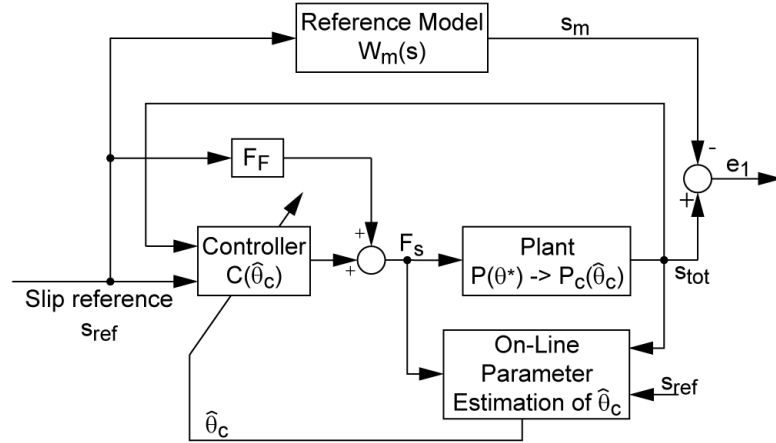


Figure 8.7: Bloc diagram of the slip control with a direct model reference adaptive control with feedforward

where  $F$  and  $g$  are constants,  $F_F$  is the SFF (Section 8.3.1) or the MFF (Section 8.3.2). The adaptive law is given by:

$$\dot{\hat{\theta}} = -\Gamma \tilde{e}_s \omega, \quad \hat{\theta}(0) = \theta_0 \quad (8.12)$$

where  $\tilde{e}_s = s_{tot} - s_m$  is the difference between the plant and the model reference,  $\hat{\theta} = [\hat{\theta}_1 \hat{\theta}_2 \hat{\theta}_3 \hat{\theta}_4]^T$  and  $\omega = [\omega_1 \omega_2 s_{tot} s_{ref}]^T$ . We can choose  $\Gamma = \text{diag}(\gamma_i)$ ,  $\gamma_i > 0$  and one obtains the adaptive law

$$\dot{\hat{\theta}}_i = -\gamma_i \tilde{e}_s \omega_i, \quad i = 1, \dots, 4 \quad (8.13)$$

The defined MRAC was implemented in simulations and in the test rig. The performances of the two controllers (PI and MRAC) are discussed in the next section.

## 8.5 Slip control performances

Evaluation of the performances of the slip control consists at first of comparing the efficiency of the slip control with the standard clamping force strategy with an over clamping of 30%. Then, we observe the slip control performances during step response of the torque and the speed ratio.

### 8.5.1 Efficiency gain

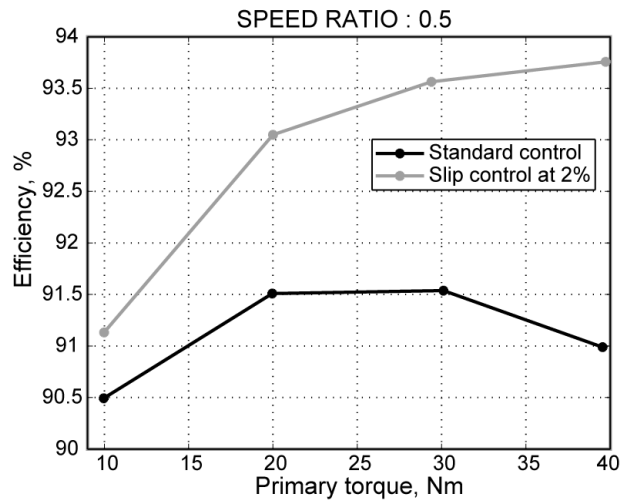
Figure 8.8 and Figure 8.9 show the variator efficiency at different speed ratios and input torques with the standard clamping force strategy and the slip control at 2%. For low torques, the slip control does not show an efficiency improvement. The lower clamping force or hydraulic pressure is limited by the hydraulic system and the slip value of 2% cannot be achieved. In general, the slip control increases the efficiency by more than 2%. These experiments consider only the mechanical efficiency. Also, the clamping forces are reduced by about 30% or even more (Figure B.6 and Figure B.7). This reduction of clamping forces will also have an influence on the hydraulic efficiency and the reduction of power of the hydraulic pump or the servo pumps is also possible.

### 8.5.2 Torque perturbations

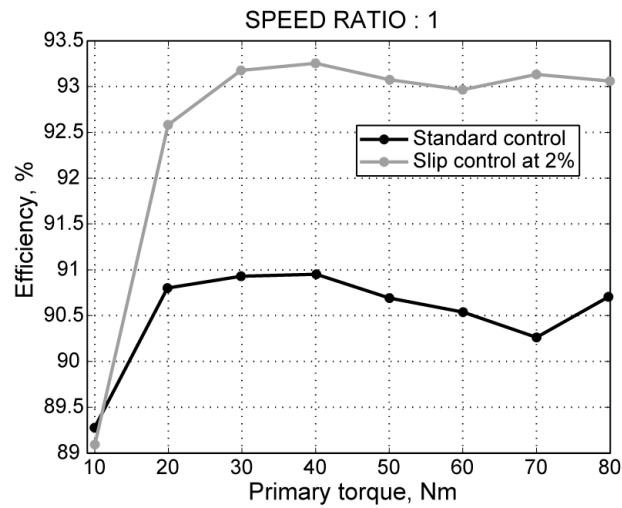
During these experiments, the speed ratio is constant while the load changes. The performances of these experiments are limited by the bandwidth of the load disturbances.

These experiments were performed with the PI and the MRAC control law with simple feedforward and mapping feedforward for a speed ratio  $r_{cvt} = 1$  and a slip reference  $s_{ref} = 2\%$  (Figure 8.10). The upper plot represents the load torque or the secondary torque, the middle plot depicts the speed ratio, the lower left plot shows the slip with the PI controller and the lower right plot represents the slip with the MRAC controller. During the load changes, the slip is perturbed and the slip control should adapt the secondary clamping force to keep the slip constant. The speed ratio is also perturbed and the control should react by changing the primary clamping force.

The two lower plots of Figure 8.10 show the slip for the PI (with SFF and MFF) controller and the MRAC (with SFF and MFF) controller. During load change, all the controllers show some slip perturbation but the controllers are stable. It can be observed that the peak is lower for PI and MRAC with mapping feedforward. The feedforward improves the system performance by anticipating and precompensating for errors. It is an open-loop anticipation of commands needed to attain a specified output. As the MFF sets the desired clamping force, the performances are improved compare to the SFF. The MRAC with MFF shows the same or slightly better performances compared to the PI with MFF. It was shown that the system is non-linear (*Section 8.5.4*) and the PI controller was designed for only one working point to avoid gain scheduling. Therefore, the performances of the PI controller are changing with the working point. In the case of the MRAC, the parameters of the control

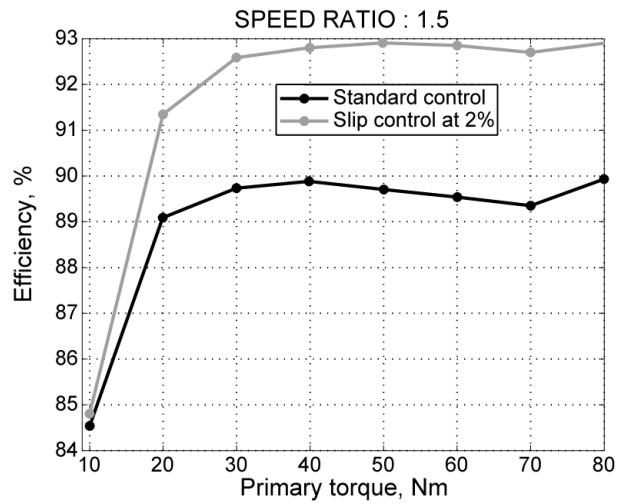


(a) Variator efficiency for a speed ratio equal to 0.5

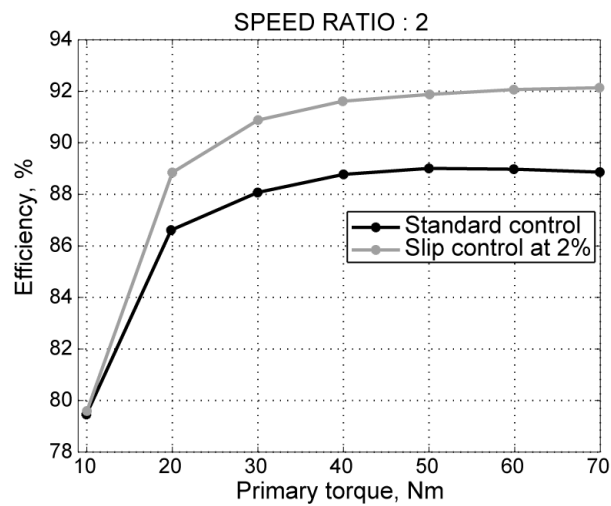


(b) Variator efficiency for a speed ratio equal to 1.0

Figure 8.8: Comparison of the variator efficiency for the standard secondary clamping force strategy and for the slip control at 2 % for underdrive and ratio 1:1 and for different input torques



(a) Variator efficiency for a speed ratio equal to 1.5



(b) Variator efficiency for a speed ratio equal to 2.0

Figure 8.9: Comparison of the variator efficiency for the standard secondary clamping force strategy and the slip control at 2 % for speed ratio 1.5 and overdrive and for different input torque



law are always modified by the adaptive law to follow the reference model and thus can increase the performances of the controller.

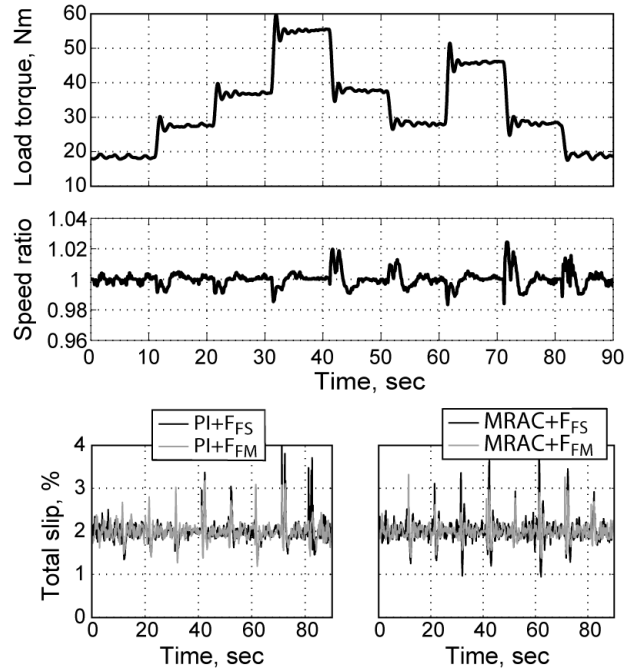


Figure 8.10: Robustness of the slip and speed ratio control during torque perturbations at ratio 1 : 1 and total slip  $s_{tot} = 2\%$

### 8.5.3 Speed ratio perturbations

The primary clamping force controls the speed ratio, but it is considered a perturbation for slip control. During shifting, radial slip due to shifting is added to the tangential slip. In the slip synthesis proposed either in this work or by different authors, only tangential slip is considered. The slip during shifting should be studied in more details (this topic is outside the scope of this thesis).

Figure 8.11 depicts an example of experiments during shifting. The same experiments were performed with the PI and MRAC controllers with both SFF and MFF. The primary torque is constant at  $40Nm$ . The total slip  $s_{tot}$  is controlled at 2%. The performances achieved in these experiments are limited by the bandwidth of the speed ratio.

The change of the ratio destabilizes the equilibrium and perturbs the slip. The slip control reacts to keep the reference slip value. All the controllers are stable over the whole span of the variator. Feedforward does not seem to play an important role in the slip performances during the shifting of the variator. The MRAC controller shows better performances compared to the PI controller. The PI controller was designed for only one working point and the performances are lost due to the non linearity of the system. The parameters

of the MRAC are always modified and then increase the slip performances compare to the PI controller. If better performances are needed with a PI controller, a gain scheduling approach is recommended.

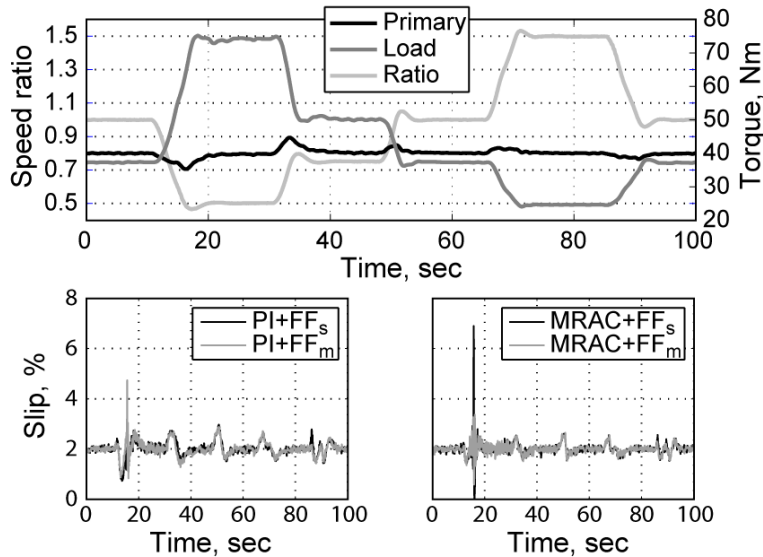


Figure 8.11: Robustness of the slip control during speed ratio perturbations with an input torque maintained at 40 Nm

#### 8.5.4 Frequency response

Slip is non-linear and it is an interest to see the response of the different controller laws for different slip references while the primary torque and the speed ratio are constant. A sinus is chosen as the slip reference. Figure 8.12 and Figure 8.13 show the experiments for "low" frequency ( $0.06Hz$ ) and "high" frequency ( $2Hz$ ) respectively.

Already at "low" frequency (Figure 8.12), the PI with SFF does not show good results. *Section 2.4.1* discussed that for small values of slip, high variations of the secondary clamping force are needed to change slip. In contrast, for high slip values, small secondary clamping force variations are needed. The PI controller was designed for a slip reference equal to 2%. Also, *Section 8.3.3* depicts that PI control bandwidth is smaller with a slip value of 1% than 2.5%. To be able to keep the same performance for different slip values, gain scheduling is needed. In line with these remarks, the PI with MFF or the MRAC shows good results.

If the frequency of the reference signal is increased (Figure 8.13), the two controllers laws PI and MRAC with SFF do not show good results. The two controllers with MFF can follow the reference with a difference of phase. In the case of the SFF, the needed clamping force is considered to be unknown and the standard secondary clamping force with a safety factor equal to one is used as feedforward (*Section 8.3.1*), the feedforward is constant and is not

optimum for this case. On the contrary, the MFF changes with the reference slip. In this case the needed secondary clamping force is known for any speed ratio, any input torque and any slip reference.

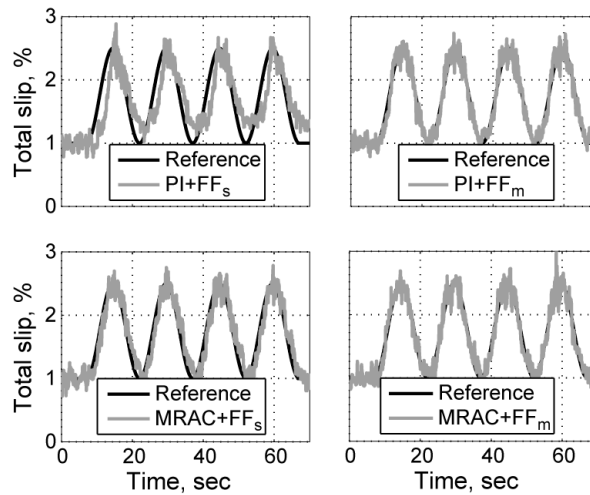


Figure 8.12: Robustness of the slip control during sinus slip reference at a frequency  $f = 0.06Hz$

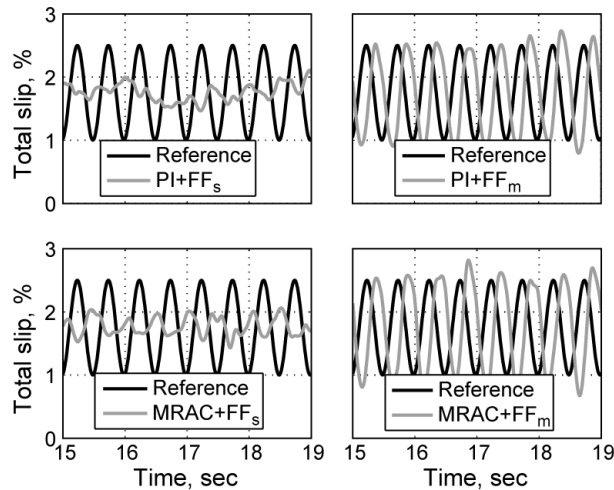


Figure 8.13: Robustness of the slip control during sinus slip reference at a frequency  $f = 2Hz$

Let's assume that the plant is linear (Figure 8.14). If the feedforward is optimum, the PI controller rejects the perturbations and the PI work is small, i.e: the output of the PI  $F_{PI}$  is small compared to the feedforward output  $F_{FF}$ . The total slip  $s_{tot}$  is equal in amplitude and phase to the reference slip  $s_{ref}$ . Due to modeling errors, the feedforward is not optimum and the PI is strongly solicited to maintain at zero the error between the reference slip  $s_{ref}$  and the measured total slip  $s_{tot}$ . The output signal of the PI  $F_{PI}$  perturbs the plant and a phase difference, due to the closed loop, can be observed.

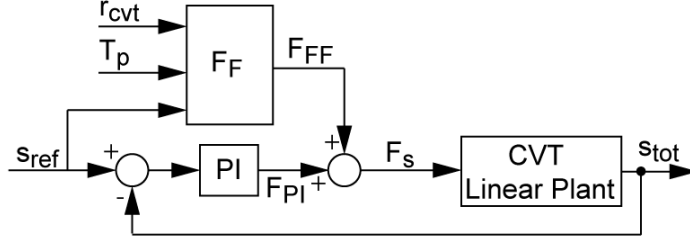


Figure 8.14: Bloc diagram for the PI slip control with feedforward. The CVT plant is considered to be linear

## 8.6 MRAC parameters

The parameters  $\hat{\theta}_i$  of the MRAC control (8.9) to (8.11) are always modified to minimize the error between the model reference and the real measured value. As discussed in *Section 8.2.2*, the system is non-linear and the parameters will vary as a function of the working point.

The next two figures depict the parameter estimation  $\hat{\theta}_i$  of the MRAC at different working points: Figure 8.15 displays these parameters during ratio change, while the input torque  $T_p$  and the total slip  $s_{tot}$  are constant at  $40Nm$  and 2% respectively, Figure 8.16 represents the parameters during torque disturbance when the speed ratio  $r_{cvt}$  is maintained constant at 1 : 1 and the total slip  $s_{tot}$  start from 1% and rises to 2%.

The two parameters  $\hat{\theta}_3$  and  $\hat{\theta}_4$  seem to be correlated together and drift as shown in Figure 8.16. Based on (8.11), the parameter  $\hat{\theta}_3$  is associated with the total slip  $s_{tot}$  and the parameter  $\hat{\theta}_4$  with the slip reference  $r_{ref}$ . If the slip control fulfills it's function, the slip reference is equal to the total slip  $s_{ref} = s_{tot}$ . It can be concluded that the parameters estimation law (8.11) optimizes more parameters than needed. Thus, a new law is proposed by fixing the parameter  $\hat{\theta}_4$  at 1.

$$\dot{\omega}_1 = F\omega_1 + gF_s, \quad \omega_1(0) = 0 \quad (8.14)$$

$$\dot{\omega}_2 = F\omega_2 + gs_{tot}, \quad \omega_2(0) = 0 \quad (8.15)$$

$$F_s = \hat{\theta}_1\omega_1 + \hat{\theta}_2\omega_2 + \hat{\theta}_3s_{tot} + s_{ref} + F_F \quad (8.16)$$

## 8.7 Summary

Slip control consists of controlling the slip of the variator using the secondary clamping force, while the primary clamping force controls the speed ratio by keeping the force balance between the primary and the secondary pulley for a constant speed ratio or by changing this equilibrium for shifting.

The slip of each pulley is estimated by the pulley rotation speed, the chain speed and the pulley radiuses. The slip of each pulley is then added to determine the total slip of the variator. The PI is the simplest controller and

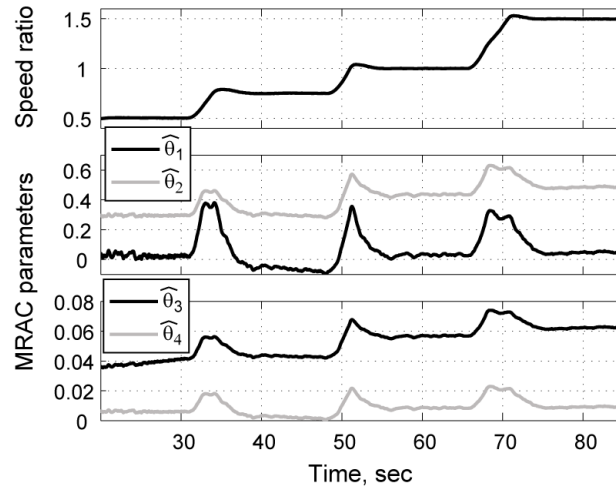


Figure 8.15: MRAC parameters during speed ratio change with a primary input torque control at 40Nm

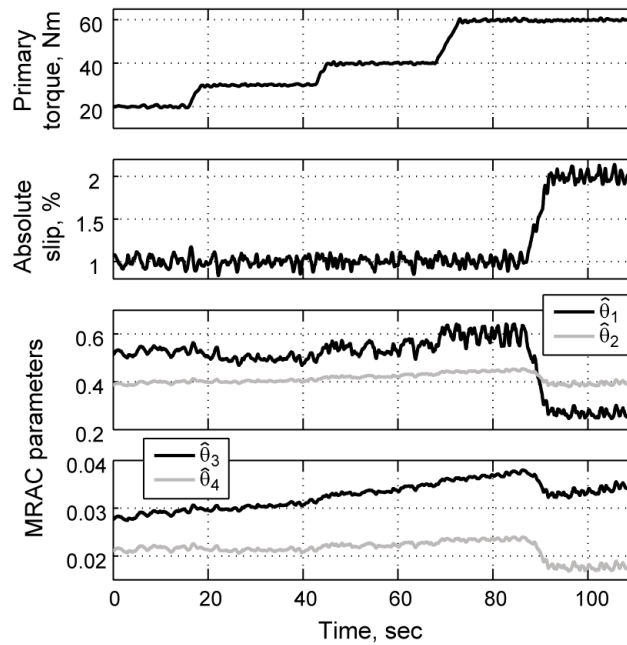


Figure 8.16: MRAC parameters during torque and slip perturbations, the speed ratio is controlled at 2%

can shown good performances but it neglects the plant non-linearity and time dependence. The friction coefficient or the traction curve can also be time varying. To deal with this time dependence, a model reference adaptive control (MRAC) was proposed.

For both PI synthesis and MRAC synthesis, two different feedforward schemes were used and discussed: the single feedforward (SFF) and the mapping feedforward (MFF). The SFF considers that the secondary clamping force needed is unknown and the standard clamping force strategy with a safety factor equal to 1 is used. The MFF considers that the needed clamping force is known and depends on the reference slip, the speed ratio and the load factor.

Even with the non-linearity of the plant, a simple PI controller without gain scheduling and the SFF guarantee the stability of the system; however it was shown that the performances are different especially for different slip reference values. The achievements of the PI controller with SFF are improved by using the MFF.

The MRAC controller with SFF showed better performances compared to the PI controller with SFF, but it still does not satisfy for reference slip variation, especially at "high" frequency. As for the PI controller, the MRAC performances are good with the MFF.

The performances of the controllers were tested for different configuration: torque perturbations, ratio speed perturbations and reference slip changes. The MRAC synthesis, especially with MFF shows the best performances. The parameters are modified, with time and working point, to follow the model reference. The model reference control is an attractive solution.

## Chapter 9

# Conclusions and recommendations

Today's car makers have to find new technologies to be able to reach the restriction of gas emissions. Hybrid electric vehicle (HEV) or continuously variable transmission (CVT) are some solutions.

The CVT for the use in automotive powertrains is motivated by the added ability of optimizing the engine operation point. This ability means that for the same power, the engine of a vehicle containing a CVT can operate at lower regime. A significant reduction in fuel consumption can then be achieved. Further improvements are still required, notably the fuel consumption reduction obtained by the improvement of the CVT efficiency. The control of the slip is one of the solution to improve the efficiency of the variator by decreasing the clamping forces. Some works on the VDT-Belt demonstrated the advantages of the slip control compare to the standard clamping force strategy.

This thesis also focused on the slip control and the contributions were:

- Introducing of a new slip synthesis by measuring the two pulley speeds and the intermediate element speed. This definition can be used for every type of CVT or IVT
- This new synthesis introduces an additional dynamics i.e. the intermediate element dynamics. A more precise dynamics model is obtain and the controller performances can be increased
- An others originality is to increase the bandwidth of the actuators to neglect them. This were simplified the plant modeling and the control of the variator
- Another originality is to propose a theoretical approach of the CVT modeling and controlling the slip with a model reference adaptive control (MRAC). This controller deals with the unknown parameters of the plant and the modeling errors

This new slip synthesis and the theoretical approach for CVT control were applied to the involute chain using two servo-pumps to generate the needed

## 112 CHAPTER 9. CONCLUSIONS AND RECOMMENDATIONS

pressure. By measuring the two pulley speeds and the chain speed, a slip on each pulley was defined to estimate the total slip of the variator. The new synthesis was applied to the total slip control at 2%. The efficiency of the variator was increased by more than 2% and the clamping force were decreased by more than 30% compare to the standard clamping force strategy.

To control the slip, a MRAC law was proposed. The idea of the MRAC is to estimate the uncertain plant parameters on-lined based on the measurement system signals and use these estimated parameters in the control law to follow a model reference. The plant is assumed to have known structure with unknown parameters. The known structure implicates that modeling should be needed to known it.

A high level model was developed to describe the dynamic of the servo-pump system, the pressure, the shifting model, the mechanical model. It was found experimentally that the flow out of the servo-pump can be estimated by a second order transfer function. The mechanical model considered the two pulleys and the chain as free bodies and therefore includes the chain dynamics. This model needs the primary and secondary clamping force ratio, traction curves. For this purpose, a more details model was presented.

This low level model take into account the elastic deformations of the pulleys, the clearance between pulley sheaves and shaft, the pin compression and the deformation of the contact point between the chain and the pulley sheaves. Indeed, the contact point deformation can be same order than the pulley sheave. Based on the elastic deformations and the force equilibrium, a complete matrix of the CVT characteristics is then available i.e. axial forces, pulley torques, traction curves and slip.

The results of the low and high level are then used to control the variator. One of the originality was to use the pole placement to control the actuator in flow i.e. control the flow that enters or exists the pulley. It was possible to increase the bandwidth and neglect the actuators dynamics. The two pulley pressures are linearized and decoupled with an input-output feedback linearization. Then the primary clamping force is used to control the speed ratio and the secondary pressure to avoid the slip of the chain or to control the slip.

To control the slip, a proportional-integrator law and a model reference adaptive control (MRAC) with a feedforward were simulated and implemented in a test rig. Two feedforward were proposed: a simple feedforward (SFF) and a mapping feedforward (MFF). SFF considered that the needed secondary clamping force is unknown and the standard secondary clamping force strategy is used with a safety factor of one. MFF considered that the needed clamping force is known for a certain slip reference, a certain speed ratio and load factor. Because the MFF known at priory the needed clamping force, it increases the performances of the slip control compare to the SFF. Finally, the greatest advantage of the MRAC, compare to the PI, is that it can deal with the change of the plant dynamic during the time and deals with the modeling errors.



## 9.1 Recommendations

For further researches, some suggestions are outlined to extend the knowledge gained in this dissertation.

**Friction coefficient of the chain** is not well known. Different parameters can affect it, but the most important is the life time i.e. wear. Further research is needed to study the friction coefficient during the life time and see how it changes the transfer function.

**Durability** test of the variator under slip control were not performed in this work. It will be of interest to know how the life time of the pulley sheaves and the chain evolve under slip control. As it is expected that the friction coefficient will change with time, the durability test will also inform about the PI or MRAC stability and performances.

**Angular position sensor** instead of the position sensor to measure the pulley radius. The speed chain measurement system had a certain angular position dependence on the geometrical ratio. By measuring this angular position instead of the primary pulley position, the geometrical ratio could be measured and a reduction of cost achieved.

**Chain forces measurements** could be of interest for the model validation. This measurement can be effected by transforming the link's elongation in force. It is not a direct measurement and a calibration is needed. A data logger could be useful to take the measurements during service.



## Appendix A

# Differential equations of the pulley slip

### A.1 Primary slip

The primary slip  $s_p$  is given by:

$$s_p = 1 - \frac{v_{ch}}{\omega_p R_p} \quad (\text{A.1})$$

By means of a logarithmic derivation with respect to time it follows

$$\frac{\dot{\omega}_p}{\omega_p} + \frac{\dot{R}_p}{R_p} + \frac{\dot{s}_p}{s_p} = \frac{\omega_p \dot{R}_p + \dot{\omega}_p R_p}{\omega_p R_p - v_{ch}} - \frac{\dot{v}_{ch}}{\omega_p R_p - v_{ch}} \quad (\text{A.2})$$

The primary radius can be approximated by a third order function depends on the geometrical ratio:

$$R_p = a_{R_p} r_{cvt,g}^3 + b_{R_p} r_{cvt,g}^2 + c_{R_p} r_{cvt,g} + d_{R_p} \quad (\text{A.3})$$

The time derivate of this equation becomes:

$$\dot{R}_p = \frac{dR_p}{dt} = \frac{\partial R_p}{\partial r_{cvt,g}} \frac{dr_{cvt,g}}{dt} = \frac{\partial R_p}{\partial r_{cvt,g}} \dot{r}_{cvt,g} = \partial f_{R_p} \dot{r}_{cvt,g} \quad (\text{A.4})$$

Rearranging the terms and considering (A.4), (A.2) can be written as follow:

$$\begin{aligned} \frac{\dot{s}_p}{s_p} = & \left( \frac{R_p}{\omega_p R_p - v_{ch}} - \frac{1}{\omega_p} \right) \dot{\omega}_p - \frac{1}{\omega_p R_p - v_{ch}} \dot{v}_{ch} \\ & + \left( \frac{\omega_p}{\omega_p R_p - v_{ch}} - \frac{1}{R_p} \right) \partial f_{R_p} \dot{r}_{cvt,g} \end{aligned} \quad (\text{A.5})$$

From (A.1):

$$\frac{\omega_p R_p - v_{ch}}{R_p} = \omega_p s_p \quad (\text{A.6})$$

$$\omega_p R_p - v_{ch} = \omega_p R_p s_p \quad (\text{A.7})$$

$$\frac{\omega_p R_p - v_{ch}}{\omega_p} = R_p s_p \quad (\text{A.8})$$

Considering these three equations, (A.5) can be simplified:

$$\dot{s}_p = \frac{1 - s_p}{\omega_p} \dot{\omega}_p - \frac{s_p}{\omega_p R_p - v_{ch}} \dot{v}_{ch} + \frac{1 - s_p}{R_p} \partial f_{R_p} \dot{r}_{cvt,g} \quad (\text{A.9})$$

Finally, considering the primary pulley and the chain speed dynamics (5.21) and (5.23) respectively, the transient behavior of the variator (5.9), (A.9) becomes

$$\begin{aligned} \dot{s}_p = & \frac{1 - s_p}{\omega_p} \frac{1}{J_p} \left( T_p - \frac{2\mu_p(s_p)}{\cos \beta} R_p F_p \right) \\ & - \frac{s_p}{\omega_p R_p - v_{ch}} \frac{1}{M_{ch}} \left( \frac{2\mu_p(s_p)}{\cos \beta} F_p - \frac{2\mu_s(s_s)}{\cos \beta} F_s \right) \\ & \frac{1 - s_p}{R_p (r_{cvt,g})} \partial f_{R_p} G(r_{cvt,g}) \left[ \ln \left( \frac{F_p}{F_s} \right) - \ln \left( \frac{F_p}{F_s} \Big|_{eq} \right) \right] \end{aligned} \quad (\text{A.10})$$

## A.2 Secondary slip

The secondary slip  $s_s$  is given by:

$$s_s = \frac{v_{ch}}{\omega_s R_s} - 1 \quad (\text{A.11})$$

By means of a logarithmic derivation with respect to time it follows

$$\frac{\dot{\omega}_s}{\omega_s} + \frac{\dot{R}_s}{R_s} + \frac{\dot{s}_s}{s_s} = \frac{\dot{v}_{ch}}{v_{ch} - \omega_s R_s} - \frac{\omega_s \dot{R}_s + \dot{\omega}_s R_s}{v_{ch} - \omega_s R_s} \quad (\text{A.12})$$

The secondary radius can be approximated by a third order function depends on the geometrical ratio:

$$R_s = a_{R_s} r_{cvt,g}^3 + b_{R_s} r_{cvt,g}^2 + c_{R_s} r_{cvt,g} + d_{R_s} \quad (\text{A.13})$$

The time derivate of this equation becomes:

$$\dot{R}_s = \frac{dR_s}{dt} = \frac{\partial R_s}{\partial r_{cvt,g}} \frac{dr_{cvt,g}}{dt} = \frac{\partial R_s}{\partial r_{cvt,g}} \dot{r}_{cvt,g} = \partial f_{R_s} \dot{r}_{cvt,g} \quad (\text{A.14})$$

Rearranging the terms and considering (A.14), (A.12) can be written as follow:

$$\begin{aligned} \frac{\dot{s}_s}{s_s} &= \frac{1}{v_{ch} - \omega_s R_s} \dot{v}_{ch} - \left( \frac{R_s}{v_{ch} - \omega_s R_s} + \frac{1}{\omega_s} \right) \dot{\omega}_s \\ &\quad - \left( \frac{\omega_s}{v_{ch} - \omega_s R_s} + \frac{1}{R_s} \right) \dot{R}_s \end{aligned} \quad (\text{A.15})$$

From (A.11):

$$\omega_s R_s s_s = v_{ch} - \omega_s R_s \quad (\text{A.16})$$

$$\omega_s s_s = \frac{v_{ch} - \omega_s R_s}{R_s} \quad (\text{A.17})$$

$$R_s s_s = \frac{v_{ch} - \omega_s R_s}{\omega_s} \quad (\text{A.18})$$

$$(\text{A.19})$$

Considering these three equations, (A.15) can be simplified:

$$\dot{s}_s = -\frac{1+s_s}{\omega_s} \dot{\omega}_s + \frac{s_s}{\omega_s R_s - v_{ch}} \dot{v}_{ch} - \frac{1+s_s}{R_s} \partial f_{R_s} \dot{r}_{cvt,g} \quad (\text{A.20})$$

Finally, considering the primary pulley and the chain speed dynamics (5.22) and (5.23) respectively, the transient behavior of the variator (5.9), (A.20) becomes

$$\begin{aligned} \dot{s}_s &= -\frac{1+s_s}{\omega_s} \frac{1}{J_s} \left( \frac{2\mu_s(s_s)}{\cos \beta} R_s F_s - T_s \right) \\ &\quad + \frac{s_s}{v_{ch} - \omega_s R_s} \frac{1}{M_{ch}} \left( \frac{2\mu_p(s_p)}{\cos \beta} F_p - \frac{2\mu_s(s_s)}{\cos \beta} F_s \right) \\ &\quad - \frac{1+s_s}{R_s (r_{cvt,g})} \partial f_{R_s} G(r_{cvt,g}) \left[ \ln \left( \frac{F_p}{F_s} \right) - \ln \left( \frac{F_p}{F_s} \Big|_{eq} \right) \right] \end{aligned} \quad (\text{A.21})$$



# Appendix B

## Other figures

This appendix contains additional figures

### B.1 Traction coefficient

Different experimental results for the primary and secondary traction curves are shown in Figure B.1 and Figure B.2 as a function of slip in underdrive, respectively overdrive ratio, for different secondary clamping forces. Figure B.3 represents the primary and secondary traction coefficient as a function of slip for different primary speeds in underdrive ratio.

### B.2 Pulley radiuses and traction coefficients

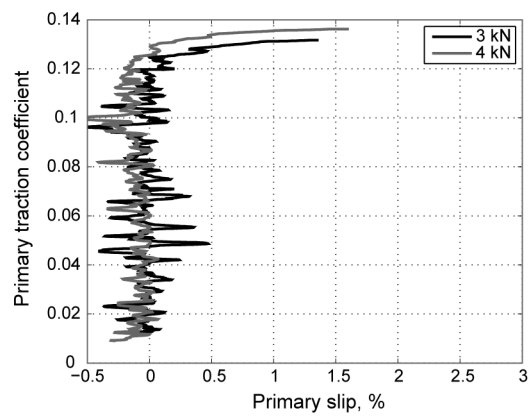
This section shows the pulley radiuses and traction coefficients for different working points and for different slip values. Figure B.4(a) and Figure B.4(b) depict the primary and the secondary pulley radius, the primary and secondary traction coefficient in underdrive and ratio 1:1 respectively.

### B.3 Experiments and simulation

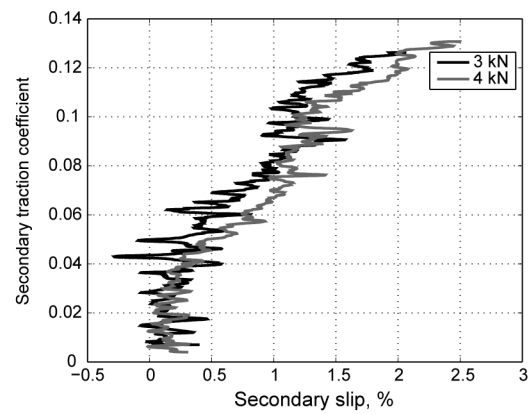
Figure B.5 show experimental data and simulations comparison when the load is increasing, the secondary clamping force and geometrical ratio are constant. For this simulation, an estimation of the measured primary and secondary traction coefficient are used.

### B.4 Clamping force comparison

This section shows the measurement of the primary and secondary clamping forces during standard clamping force strategy and during a slip control at 2%. With this slip control, the clamping forces are reduce by more than 30%. The minimum pressure is limited and for low torque, the clamping force improvement is small.



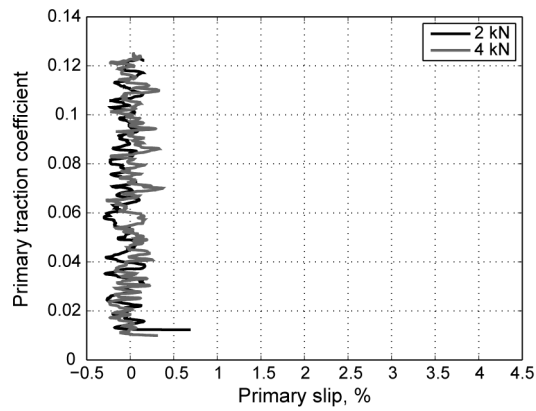
(a) Primary traction coefficient



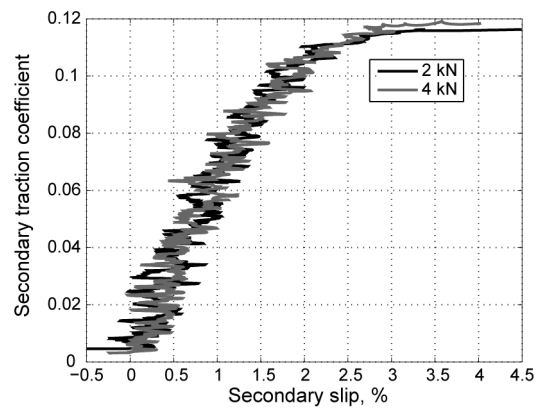
(b) Secondary traction coefficient

Figure B.1: Primary (a) and secondary (b) traction coefficients as a function of slip for different secondary clamping forces in underdrive ratio



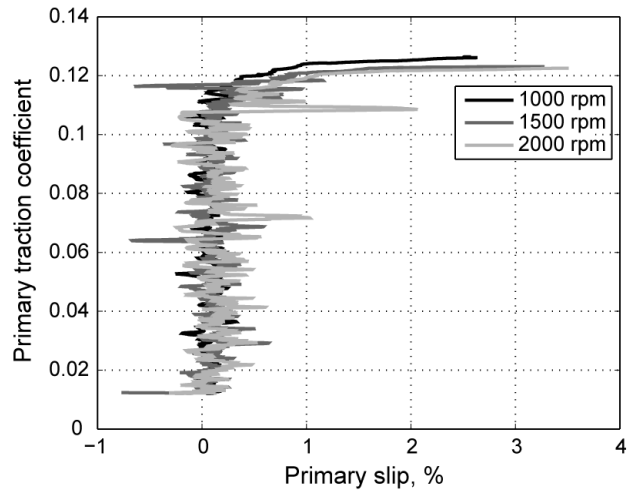


(a) Primary traction coefficient

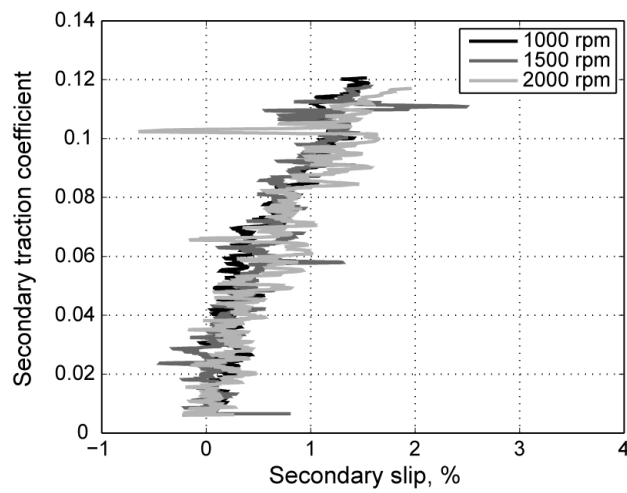


(b) Secondary traction coefficient

Figure B.2: Primary (a) and secondary (b) traction coefficients as a function of slip for different secondary clamping forces in overdrive ratio

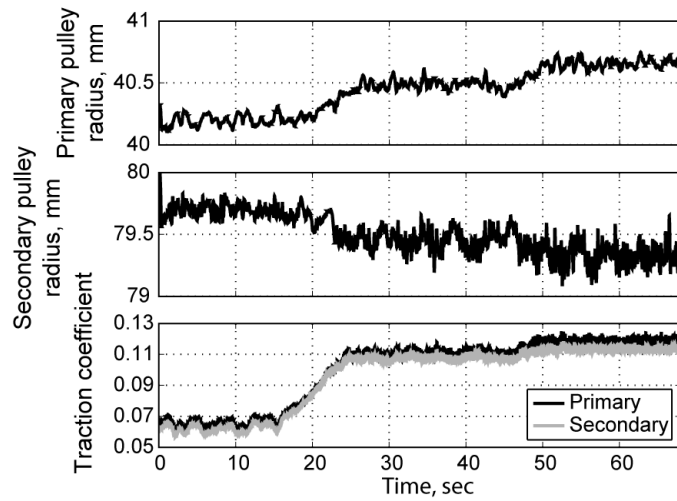


(a) Primary traction coefficient

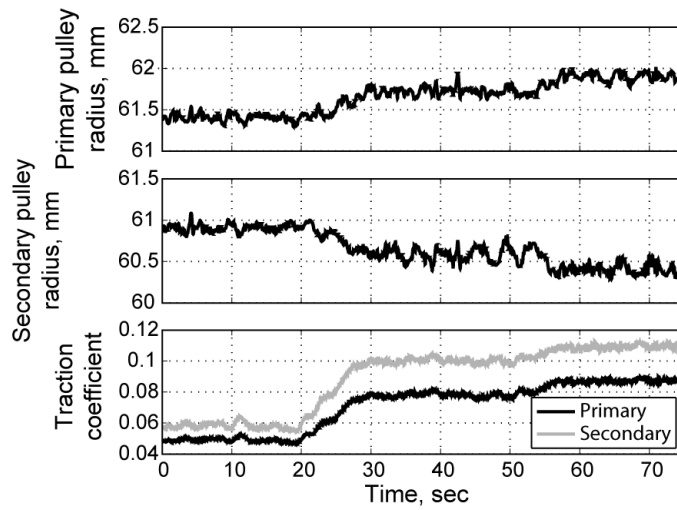


(b) Secondary traction traction

Figure B.3: Primary (a) and secondary (b) traction coefficient as a function of slip for different primary speeds in underdrive ratio

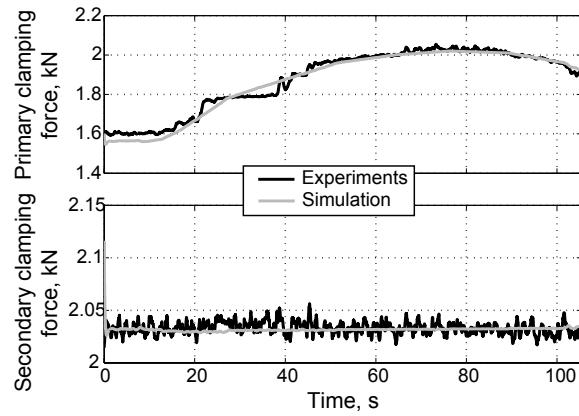


(a) Pulley radius and traction coefficient in underdrive

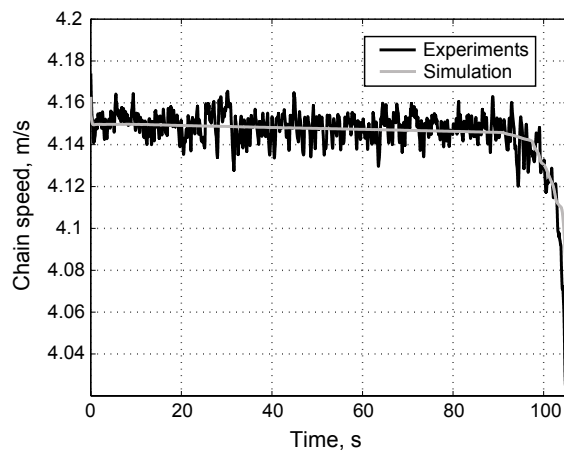


(b) Pulley radius and traction coefficient in ratio 1:1

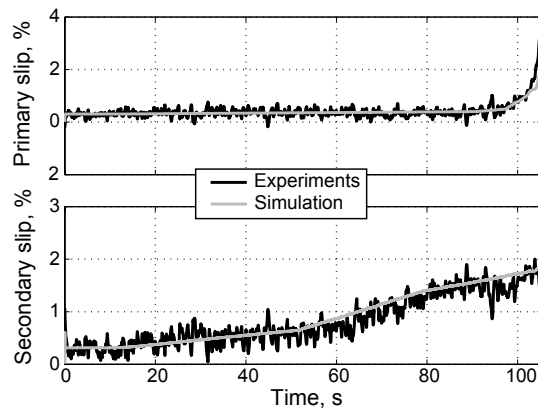
Figure B.4: Pulley radiuses and traction coefficient in underdrive and middle ratio for different values of slip with an input torque equal at 30Nm



(a) Primary and secondary clamping force

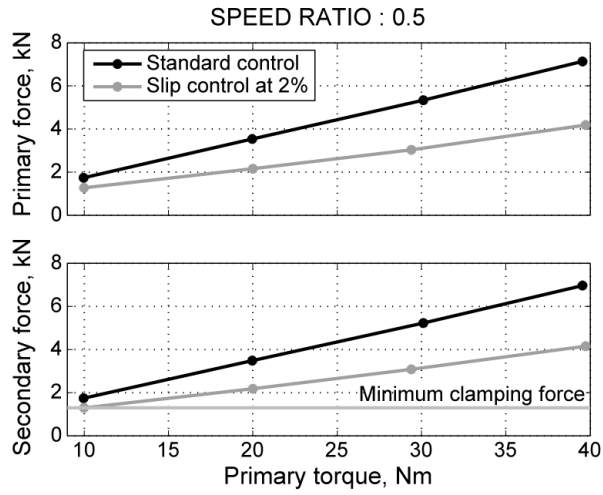


(b) Chain speed

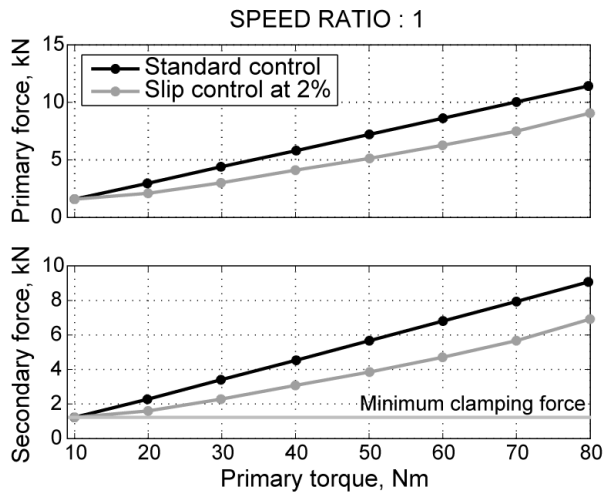


(c) Primary and secondary slip

*Figure B.5: Comparison between experiments and simulation during slip measurement*

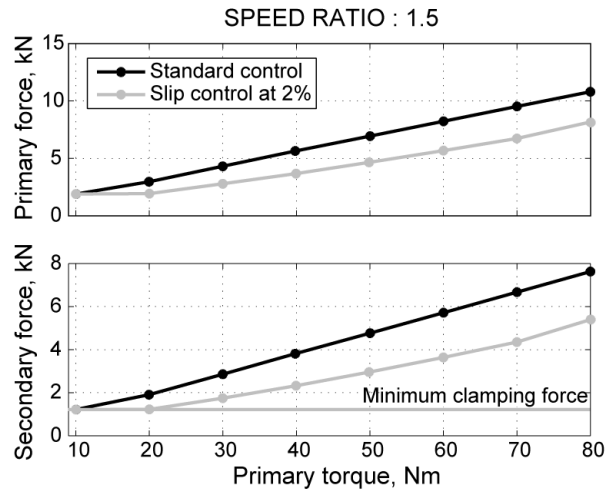


(a) Underdrive ratio

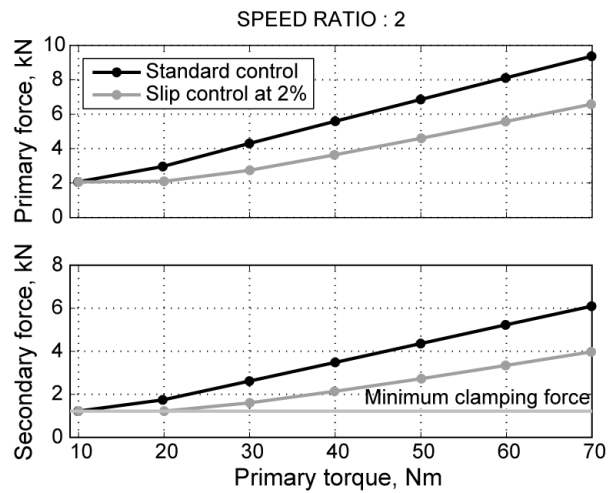


(b) Ratio 1:1

Figure B.6: Comparison of the primary and the secondary clamping force between the standard secondary clamping force strategy and the slip control at 2% for underdrive and ratio 1:1 and for different input torque



(a) Speed ratio equal at 1.5



(b) Over drive ratio

Figure B.7: Comparison of the primary and the secondary clamping force between the standard secondary clamping force strategy and the slip control at 2% for ratio 1.5 and overdrive and for different input torque

# Appendix C

## Pulley deformation comparison

This appendix compares the Sattler model (Sattler (1999)) with the model described in *Section 4.4*.

### C.1 Sattler model

Sattler uses trigonometric relations to describe the variation of the pulley half angle  $\beta$  and the axial displacement of the pulley  $D_{def}$  due to elastic deformations.

$$\beta = \beta_0 + \frac{\Delta}{2} \sin\left(\theta - \theta_c + \frac{\pi}{2}\right) \quad (\text{C.1})$$

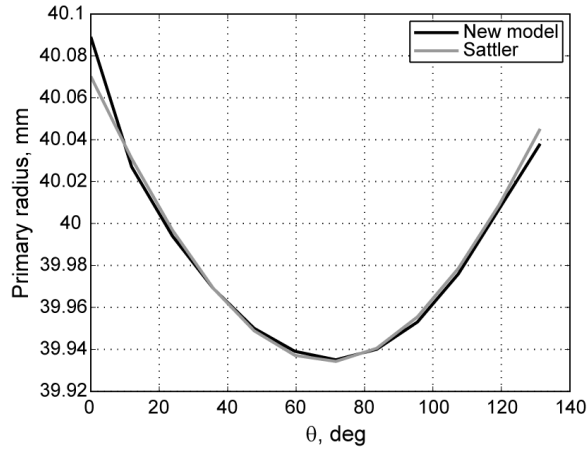
$$D_{def} = 2R_0 \tan(\beta - \beta_0) \quad (\text{C.2})$$

Where  $\beta_0$  is the non deformed pulley half angle,  $\theta_c$  is the center wedge expansion,  $R_0$  is the non deformed pulley radius and  $\Delta$  is a parameter equivalent to the pulley stiffness.  $\Delta$  is a parameter that depends on the pulley radius and clamping force (Sferra et al. (2002)). Using the same geometry as that depicted in Figure 4.10, the deformed pulley radius  $r$  is given by

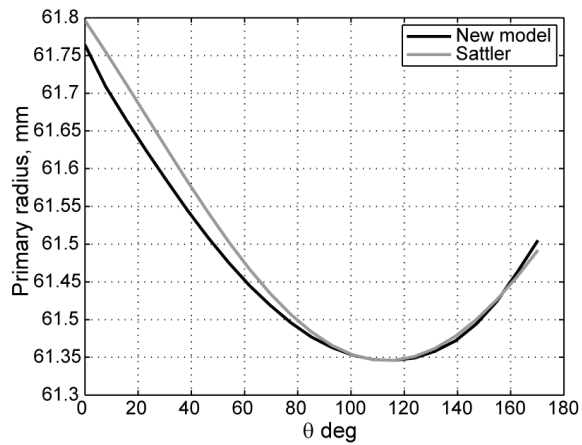
$$r = R_0 \frac{\tan \beta_0}{\tan \beta} - \frac{D_{def}}{2 \tan \beta} \quad (\text{C.3})$$

### C.2 Deformation comparison

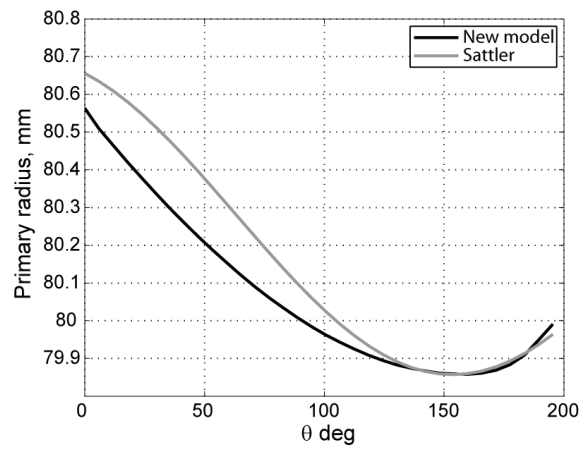
Figure C.1 and Figure C.2 compare the deformation of the pulley radius of the primary and secondary pulleys estimated with the Sattler model and the model developed in this work for different ratio. Some differences can be seen between the two models and justify the development of the new model.



(a) Primary pulley radius deformation in underdrive ratio



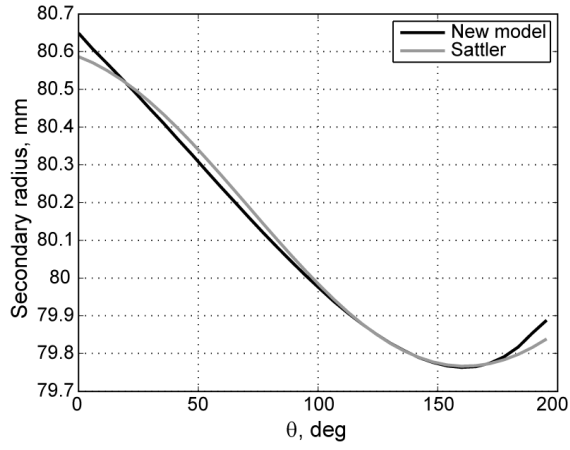
(b) Primary pulley radius deformation in middle ratio



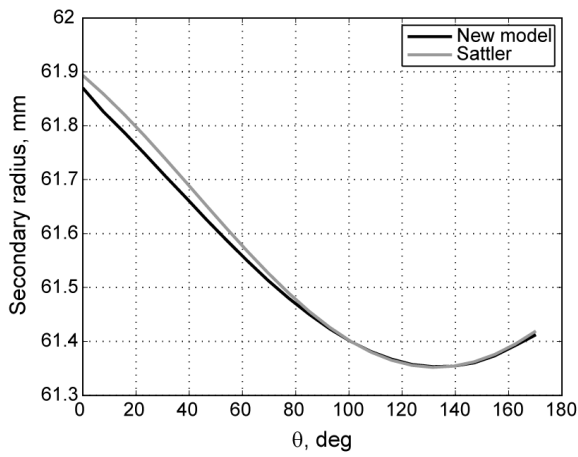
(c) Primary pulley radius deformation in ratio overdrive ratio

Figure C.1: Primary pulley radius deformations for different ratio. Comparison between the Sattler model and the new model

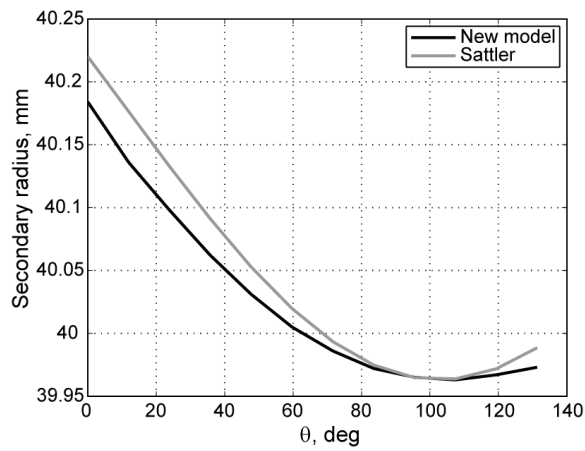




(a) Secondary pulley radius deformation in underdrive ratio



(b) Secondary pulley radius deformation in 1:1 ratio



(c) Secondary pulley radius deformation in overdrive ratio

Figure C.2: Secondary pulley radius deformations for different ratio. Comparison between the Sattler model and the new model



## Appendix D

# Servo pump: detailed model

This appendix gives a detailed model of the servo pump. This model could be used for more studies of the servo pump system.

The servo pump is basically composed of two sub-systems: a servo motor and a pump (Figure D.1). In this work, an external gear pump is used.

A electric signal  $V_m$  is supplied to the motor to drive it. The servo motor and the pump rotate at the same speed  $\omega_m$ . The pump generates an output flow  $Q_o$ . If no leakage is considered, the input flow  $Q_i$  is equal at the output flow  $Q_o$ . Through the hydraulic circuit, a pressure  $P_o$  is generated. The output pressure is higher or smaller than the input pressure  $P_i$  and generates a load on the motor.

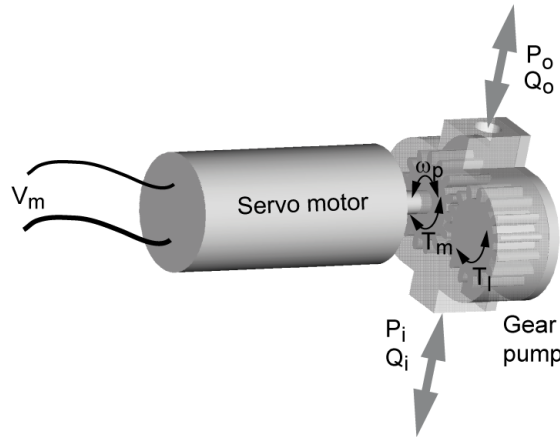


Figure D.1: Servo motor and hydraulic pump that constitute the servo pump

### D.1 Motor model

A brushless DC motor with permanent magnets is utilized to drive the hydraulic pump. Brushless DC motors are typically characterized by a trape-

zoidal back electromotive force <sup>1</sup> (EMF) and are typically driven by rectangular current pulses. PM synchronous motors differ from brushless DC motors in that they typically have a sinusoidal back EMF and are driven by sinusoidal currents.

The motor can be modeled in details by considering the mechanical design, the inductance, the losses etc.. (Ohm (1997), Wallmark (2002), Hanselman (2003)). This kind of models are useful for the motor design. The motor model used in the servo pump is needed for control purpose only and a simpler model is appropriate.

Figure D.2 depicts the electric circuit of the armature and the free body diagram of the rotor (Longchamp (1995)).

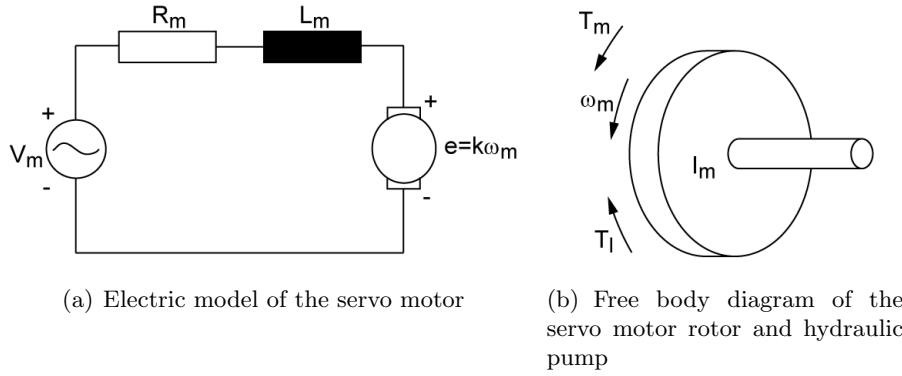


Figure D.2: Electric circuit of the servo motor armature and the free body diagram of the rotor

Where  $I_m$  is the moment of inertia of the rotor and the hydraulic pump <sup>2</sup>,  $k$  is the electromotive force or constant of the motor,  $R_m$  is the terminal resistance phase to phase,  $L_m$  is the terminal inductance phase to phase,  $\omega_m$  is the rotation speed,  $V_m$  is the source voltage,  $T_m$  is the motor torque and  $T_l$  is the load applied to the motor.

The motor torque  $T_m$  is related to the armature current  $i$  by the constant of the motor  $k$ . The back electromotrice force  $e$  is related to the rotational velocity by the following equations :

$$T_m = ki \quad (D.1)$$

$$e = k\omega_m \quad (D.2)$$

From Figure D.2, the following equations based on Newton's law for the mechanical model and Kirchoff's law for the electric model.

<sup>1</sup>Force which produces, or tends to produce, electricity, or and electric current

<sup>2</sup>The rotor and the hydraulic pump can be considered as one element

$$I_m \dot{\omega}_m = T_m - T_i \quad (\text{D.3})$$

$$U_m = R_m i - L_m \frac{di}{dt} + e \quad (\text{D.4})$$

Using (D.1) and (D.2), the under equations yields:

$$I_m \dot{\omega}_m = k i - T_l \quad (\text{D.5})$$

$$U_m = R_m i - L_m \frac{di}{dt} + k \omega_m \quad (\text{D.6})$$

The torque load comes from the difference pressure at the output and the input of the pump. The pump used in this work is an external gear pump

## D.2 Pump model

The gear pump have just two moving parts. Each gear move at constant speed and experience a uniform force. Internal construction, shown in Figure D.3, consists of just two close meshing gear wheels which rotate as shown.

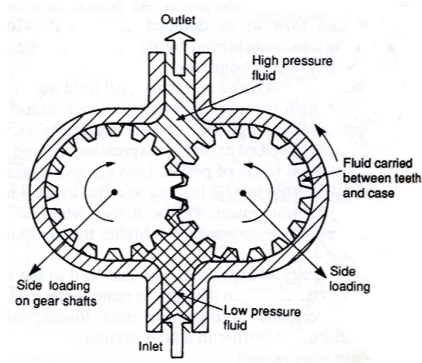


Figure D.3: Internal design of a gear pump (Merritt (2001))

As the teeth come out of mesh at the center, a partial vacuum is formed which draws fluid into the inlet chamber. Fluid is trapped between the outer teeth and the pump housing, causing a continual transfer of fluid from inlet chamber to outlet chamber where it is discharged to the system.

Pump displacement is determined by the volume of fluid between each pair of teeth, the number of teeth and the rotation speed.

### D.2.1 Hydraulic model

An ideal pump is defined as having no power losses due the friction and leakage (Merritt (2001)). The mechanical power output is

$$hp|_{out} = T_l \dot{\theta}_{gp} \quad (D.7)$$

where  $T_l$  is torque generated by the motor and delivered to the load,  $\dot{\theta}_{gp}$ , the gear speed. The hydraulic power supplied to the pump is

$$hp|_{out} = \frac{P_l Q_l}{(P_2 - P_1) Q_l} \quad (D.8)$$

where  $P_l$  is the pressure difference across the pump,  $Q_l$  is the flow through the pump. Because no power losses is assumed, these expressions can be equated to yield

$$T_l = \frac{Q_l}{\dot{\theta}_{gp}} P_l \quad (D.9)$$

The volumetric displacement of the pump  $D_m$  is defined by:

$$D_m = \frac{Q_l}{\dot{\theta}_{gp}} \quad (D.10)$$

Combining the equations, the torque load yields:

$$T_l = \frac{D_m P_l}{D_m (P_o - P_i)} \quad (D.11)$$

(D.10) and (D.11) are the fundamental relations for an ideal pump. Only one parameter,  $D_m$  is required to define the ideal pump, and this quantity is also the single most important parameter for practical machines.

## Appendix E

# Standard slip

The standard slip synthesis  $s_{sd}$  described in Section 3.4.1 is given by:

$$s_{sd} = 1 - \frac{r_{cvt}}{r_{cvt,g}} \quad (\text{E.1})$$

where  $r_{cvt}$  is the speed ratio and  $r_{cvt,g}$  is the geometrical ratio of the variator.

The derivate with respect to time of the slip  $s_{sd}$  yield to:

$$\dot{s}_{sd} = \frac{r_{cvt}\dot{r}_{cvt,g} - \dot{r}_{cvt}r_{cvt,g}}{r_{cvt,g}^2} \quad (\text{E.2})$$

Rearranging the terms it follows:

$$\dot{s}_{sd} = \frac{1 - s_{sd}}{r_{cvt,g}}\dot{r}_{cvt,g} - \frac{1}{r_{cvt,g}}\dot{r}_{cvt} \quad (\text{E.3})$$

The speed ratio  $r_{cvt}$  and its derivate with respect to time  $\dot{r}_{cvt}$  are given by

$$r_{cvt} = \frac{\omega_s}{\omega_p} \quad (\text{E.4})$$

$$\dot{r}_{cvt} = \frac{1}{\omega_p}\dot{\omega}_s - \frac{r_{cvt}}{\omega_p}\dot{\omega}_p \quad (\text{E.5})$$

The geometrical ratio  $r_{cvt,g}$  and its derivative with respect to time  $\dot{r}_{cvt,g}$  yield to

$$r_{cvt,g} = \frac{R_p}{R_s} \quad (\text{E.6})$$

$$\dot{r}_{cvt,g} = \frac{1}{R_s}\dot{R}_p - \frac{r_{cvt,g}}{R_s}\dot{R}_s \quad (\text{E.7})$$

Introducing (E.4) to (E.7) into (E.2), the differential equation of the slip become:

$$\dot{s}_{sd} = \frac{1 - s_{sd}}{\omega_p} \dot{\omega}_p - \frac{1 - s_{sd}}{\omega_s} \dot{\omega}_s + \frac{1 - s_{sd}}{R_p} \dot{R}_p - \frac{1 - s_{sd}}{R_s} \dot{R}_s \quad (\text{E.8})$$

The two first terms are the contribution of the primary and the secondary pulley dynamics, the two last terms are the contribution of the geometrical ratio dynamics.



# Appendix F

## Linearization

The model of the variator dynamic was derived in *Chapter 5* and is summarized here after:

$$\dot{\omega}_p = \frac{1}{J_p} \left( T_p - \frac{2\mu_p}{\cos \beta_0} R_p F_p \right) \quad (\text{F.1})$$

$$\dot{\omega}_s = \frac{1}{J_s} \left( \frac{2\mu_s}{\cos \beta_0} R_s F_s - T_s \right) \quad (\text{F.2})$$

$$\dot{r}_{cvt,g} = \omega_p G(r_{cvt,g}) \left[ \ln \left( \frac{F_p}{F_s} \right) - \ln \left( \frac{F_p}{F_s} \Big|_{eq} \right) \right] \quad (\text{F.3})$$

$$\begin{aligned} \dot{s}_p &= \frac{1-s_p}{\omega_p} \frac{1}{J_p} \left( T_p - \frac{2\mu_p}{\cos \beta_0} R_p F_p \right) - \frac{1}{\omega_p R_p} \frac{1}{M_{ch}} \left( \frac{2\mu_p}{\cos \beta_0} F_p - \frac{2\mu_s}{\cos \beta_0} F_s \right) \\ &\quad + \frac{1-s_p}{R_p} \frac{dR_p}{dr_{cvt,g}} \omega_p G(r_{cvt,g}) \left[ \ln \left( \frac{F_p}{F_s} \right) - \ln \left( \frac{F_p}{F_s} \Big|_{eq} \right) \right] \end{aligned} \quad (\text{F.4})$$

$$\begin{aligned} \dot{s}_s &= -\frac{1+s_s}{\omega_s} \frac{1}{J_s} \left( \frac{2\mu_s}{\cos \beta_0} R_s F_s - T_s \right) + \frac{1}{\omega_s R_s} \frac{1}{M_{ch}} \left( \frac{2\mu_p}{\cos \beta_0} F_p - \frac{2\mu_s}{\cos \beta_0} F_s \right) \\ &\quad - \frac{1-s_s}{R_s} \frac{dR_s}{dr_{cvt,g}} \omega_p G(r_{cvt,g}) \left[ \ln \left( \frac{F_p}{F_s} \right) - \ln \left( \frac{F_p}{F_s} \Big|_{eq} \right) \right] \end{aligned} \quad (\text{F.5})$$

$$r_{cvt} = \frac{\omega_s}{\omega_p} \quad (\text{F.6})$$

$$s_{tot} = s_s + s_p \quad (\text{F.7})$$

Defining the state vector  $\mathbf{X} = [ \omega_p \ \omega_s \ r_{cvt,g} \ s_p \ s_s ]^T$ , the input vector  $\mathbf{U} = [ F_p \ F_s \ T_p \ T_s ]^T$ , the output vector  $\mathbf{Y} = [ r_{cvt} \ s_{tot} ]$ , and when linearized around a working point  $\mathbf{X} = [ \omega_{p,0} \ \omega_{s,0} \ r_{cvt,g,0} \ s_{p,0} \ s_{s,0} ]^T$ , yields to a form like:

$$\dot{\mathbf{X}} = \mathbf{A}\mathbf{X} + \mathbf{B}\mathbf{U} \quad (\text{F.8})$$

$$\mathbf{Y} = \mathbf{C}\mathbf{X} \quad (\text{F.9})$$

The matrix  $A$ ,  $B$  and  $C$  are defined by (Chen (2004)):

$$\mathbf{A} = \begin{bmatrix} \partial f_1/\partial\omega_p & \partial f_1/\partial\omega_s & \partial f_1/\partial r_{cvt,g} & \partial f_1/\partial s_p & \partial f_1/\partial s_s \\ \partial f_2/\partial\omega_p & \partial f_2/\partial\omega_s & \partial f_2/\partial r_{cvt,g} & \partial f_2/\partial s_p & \partial f_2/\partial s_s \\ \partial f_3/\partial\omega_p & \partial f_3/\partial\omega_s & \partial f_3/\partial r_{cvt,g} & \partial f_3/\partial s_p & \partial f_3/\partial s_s \\ \partial f_4/\partial\omega_p & \partial f_4/\partial\omega_s & \partial f_4/\partial r_{cvt,g} & \partial f_4/\partial s_p & \partial f_4/\partial s_s \\ \partial f_5/\partial\omega_p & \partial f_5/\partial\omega_s & \partial f_5/\partial r_{cvt,g} & \partial f_5/\partial s_p & \partial f_5/\partial s_s \end{bmatrix} \quad (\text{F.10})$$

$$\mathbf{B} = \begin{bmatrix} \partial f_1/\partial F_p & \partial f_1/\partial F_s & \partial f_1/\partial T_p & \partial f_1/\partial T_s \\ \partial f_2/\partial F_p & \partial f_2/\partial F_s & \partial f_2/\partial T_p & \partial f_2/\partial T_s \\ \partial f_3/\partial F_p & \partial f_3/\partial F_s & \partial f_3/\partial T_p & \partial f_3/\partial T_s \\ \partial f_4/\partial F_p & \partial f_4/\partial F_s & \partial f_4/\partial T_p & \partial f_4/\partial T_s \\ \partial f_5/\partial F_p & \partial f_5/\partial F_s & \partial f_5/\partial T_p & \partial f_5/\partial T_s \end{bmatrix} \quad (\text{F.11})$$

$$\mathbf{C} = \begin{bmatrix} \partial g_1/\partial\omega_p & \partial g_1/\partial\omega_s & \partial g_1/\partial r_{cvt,g} & \partial g_1/\partial s_p & \partial g_1/\partial s_s \\ \partial g_2/\partial\omega_p & \partial g_2/\partial\omega_s & \partial g_2/\partial r_{cvt,g} & \partial g_2/\partial s_p & \partial g_2/\partial s_s \end{bmatrix} \quad (\text{F.12})$$

After the partial derivatives and simplifications, the three matrix  $A$ ,  $B$  and  $C$  become:

$$\mathbf{A} = \begin{bmatrix} 0 & 0 & a_{13} & a_{14} & 0 \\ 0 & 0 & a_{23} & 0 & a_{25} \\ 0 & 0 & a_{33} & 0 & 0 \\ 0 & 0 & a_{43} & a_{44} & a_{45} \\ 0 & 0 & a_{53} & a_{54} & a_{55} \end{bmatrix} \quad (\text{F.13})$$

$$\mathbf{B} = \begin{bmatrix} b_{11} & 0 & b_{13} & 0 \\ 0 & b_{22} & 0 & b_{14} \\ b_{31} & b_{32} & b_{33} & 0 \\ b_{41} & b_{42} & b_{43} & 0 \\ b_{51} & b_{52} & b_{53} & b_{54} \end{bmatrix} \quad (\text{F.14})$$

$$\mathbf{C} = \begin{bmatrix} c_{11} & c_{12} & 0 & 0 & 0 \\ 0 & 0 & 0 & 1 & 1 \end{bmatrix} \quad (\text{F.15})$$

with

$$a_{13} = -\frac{2F_p}{J_p \cos \beta_0} \left( \frac{\partial \mu_p}{\partial r_{cvt,g}} R_p + \mu_p \frac{dR_p}{dr_{cvt,g}} \right) \quad (\text{F.16})$$

$$a_{14} = -\frac{2}{J_p \cos \beta_0} \frac{\partial \mu_p}{\partial s_p} R_p F_p \quad (\text{F.17})$$

$$a_{23} = \frac{2F_s}{J_s \cos \beta_0} \left( \frac{\partial \mu_s}{\partial r_{cvt,g}} R_s + \mu_s \frac{dR_s}{dr_{cvt,g}} \right) \quad (\text{F.18})$$

$$a_{25} = \frac{2}{J_s \cos \beta_0} \frac{\partial \mu_s}{\partial s_s} R_s F_s \quad (\text{F.19})$$

$$a_{33} = -\frac{\omega_p G}{K_{st}} \frac{\partial K_{st}}{\partial r_{cvt,g}} \quad (\text{F.20})$$

$$\begin{aligned} a_{43} &= -\frac{2}{J_p \omega_p \cos \beta_0} (1 - s_p) F_p \left( \frac{\partial \mu_p}{\partial r_{cvt,g}} R_p + \mu_p \frac{dR_p}{dr_{cvt,g}} \right) - \\ &= \frac{2}{\omega_p R_p M_{ch} \cos \beta_0} \left( \frac{\partial \mu_p}{\partial r_{cvt,g}} F_p - \frac{\partial \mu_s}{\partial r_{cvt,g}} F_s \right) - \\ &\quad \frac{1 - s_p}{R_p K_{st}} \frac{dR_p}{dr_{cvt,g}} \omega_p G \frac{\partial K_{st}}{\partial r_{cvt,g}} \end{aligned} \quad (\text{F.21})$$

$$a_{44} = -2F_p \frac{\partial \mu_s}{\partial s_p} \left( \frac{(1 - s_p) R_p}{J_p \omega_p \cos \beta_0} + \frac{1}{\omega_p R_p M_{ch} \cos \beta_0} \right) \quad (\text{F.22})$$

$$a_{45} = \frac{2F_s}{\omega_p R_p M_{ch} \cos \beta_0} \frac{\partial \mu_s}{\partial s_s} \quad (\text{F.23})$$

$$\begin{aligned} a_{53} &= -\frac{2}{\omega_s J_s \cos \beta_0} (1 + s_s) F_s \left( \frac{\partial \mu_s}{\partial r_{cvt,g}} R_s + \mu_s \frac{dR_s}{dr_{cvt,g}} \right) \\ &\quad + \frac{2}{\omega_s R_s M_{ch} \cos \beta_0} \left( \frac{\partial \mu_p}{\partial r_{cvt,g}} F_p - \frac{\partial \mu_s}{\partial r_{cvt,g}} F_s \right) \\ &\quad + \frac{1}{R_s K_{st}} (1 + s_s) \frac{dR_s}{dr_{cvt,g}} \omega_p G \frac{\partial K_{st}}{\partial r_{cvt,g}} \end{aligned} \quad (\text{F.24})$$

$$a_{54} = \frac{2}{\omega_s R_s M_{ch} \cos \beta_0} F_p \frac{\partial \mu_p}{\partial s_p} \quad (\text{F.25})$$

$$a_{55} = -\left( \frac{2(1 + s_s) R_s}{\omega_s J_s \cos \beta_0} + \frac{2}{\omega_s R_s M_{ch} \cos \beta_0} \right) \frac{\partial \mu_s}{\partial s_s} F_s \quad (\text{F.26})$$

$$b_{11} = -\frac{2\mu_p R_p}{J_p \cos \beta_0} \quad (\text{F.27})$$

$$b_{13} = \frac{1}{J_p} \quad (\text{F.28})$$

$$b_{22} = \frac{2\mu_s R_s}{J_s \cos \beta_0} \quad (\text{F.29})$$

$$b_{24} = -\frac{1}{J_s} \quad (\text{F.30})$$

$$b_{31} = \frac{\omega_p G}{F_p} \quad (\text{F.31})$$

$$b_{32} = -\omega_p G \left( \frac{1}{F_s} + \frac{1}{K_{st}} \frac{\partial K_{st}}{\partial F_s} \right) \quad (\text{F.32})$$

$$b_{33} = -\frac{\omega_p G}{K_{st}} \frac{\partial K_{st}}{\partial T_p} \quad (\text{F.33})$$

$$b_{41} = -\frac{2(1-s_p)\mu_p R_p}{\omega_p J_p \cos \beta_0} - \frac{2\mu_p}{\omega_p R_p M_{ch} \cos \beta_0} + \frac{(1-s_p)\omega_p G}{R_p F_p} \omega_p G \quad (\text{F.34})$$

$$b_{42} = \frac{2\mu_s}{\omega_p R_p M_{ch} \cos \beta_0} - \frac{\omega_p G}{R_p} (1-s_p) \frac{dR_p}{dr_{cvt,g}} \left( \frac{1}{F_s} + \frac{1}{K_{st}} \frac{\partial K_{st}}{\partial F_s} \right) \quad (\text{F.35})$$

$$b_{43} = \frac{1-s_p}{\omega_p J_p} - \frac{(1-s_p)\omega_p G}{R_p K_{st}} \frac{dR_p}{dr_{cvt,g}} \frac{\partial K_{st}}{\partial T_p} \quad (\text{F.36})$$

$$b_{51} = \frac{2\mu_p}{\omega_s R_s M_{ch} \cos \beta_0} - \frac{\omega_p G}{R_s F_p} \frac{dR_s}{dr_{cvt,g}} (1+s_s) \quad (\text{F.37})$$

$$b_{52} = -\frac{2\mu_s R_s}{\omega_s J_s \cos \beta_0} (1+s_s) - \frac{2\mu_s}{\omega_s R_s M_{ch} \cos \beta_0} + \frac{(1+s_s)\omega_p G}{R_s} \frac{dR_s}{dr_{cvt,g}} \left( \frac{1}{F_s} + \frac{1}{K_{st}} \frac{\partial K_{st}}{\partial F_s} \right) \quad (\text{F.38})$$

$$b_{53} = \frac{1+s_s \omega_p G}{R_s K_{st}} \frac{dR_s}{dr_{cvt,g}} \frac{\partial K_{st}}{\partial T_p} \quad (\text{F.39})$$

$$b_{54} = \frac{1+s_s}{\omega_s J_s} \quad (\text{F.40})$$

$$c_{11} = -\frac{\omega_s}{\omega_p^2} \quad (\text{F.41})$$

$$c_{12} = \frac{1}{\omega_p} \quad (\text{F.42})$$

# Appendix G

## Testing facilities

An overview of the test bench (Figure G.1) used to validate the models and the controllers strategies is given in this appendix. It is composed of an electric motor of  $55kW$ , a CVT variator with an  $30mm$  involute chain, a dynamo of  $91kW$  and finally the servo pumps system set up with a servo motor of  $400W$  and a bi-rotational external gear pump of  $0.88cc$ .

Additional sensors are placed to measure the pulleys speed  $\omega_x$  (max speed  $6000 rpm$ ) and torque  $T_x$  (max torque  $100 Nm$ ), the pressure  $P_x$ , the flow that enter or exist the pulley  $Q_x$ , the primary pulley position  $z_p$  and finally the chain speed  $v_{ch}$ .

The all sensors are collected to a dSPACE system to control the test rig as the pulleys pressure, the speed ratio, the input torque, the rotation speed and safety software. An additional computer is used for a human interface to allow an easy use of the test bench.

### G.1 Electric motor

The electric motor is composed of an AC  $55kW$ . The speed range is from 0 to  $4500rpm$ . The power characteristic is given in Figure G.2.

An engine simulation is not possible with this electric motor due to the higher inertia of this electric motor compare to an engine. Also, the torque ripple can not be simulate.

### G.2 Dynamo

The dynamo, effectively a brake, is the load of the transmission. It can absorb a power up to  $91kW$ . The maximum speed and torque is respectively  $1800rpm$  and  $450Nm$ .

### G.3 Input and output sensor

The two speed and torque sensors, located at the input and output of the variator, monitor the power of the transmission. The torque is measured by

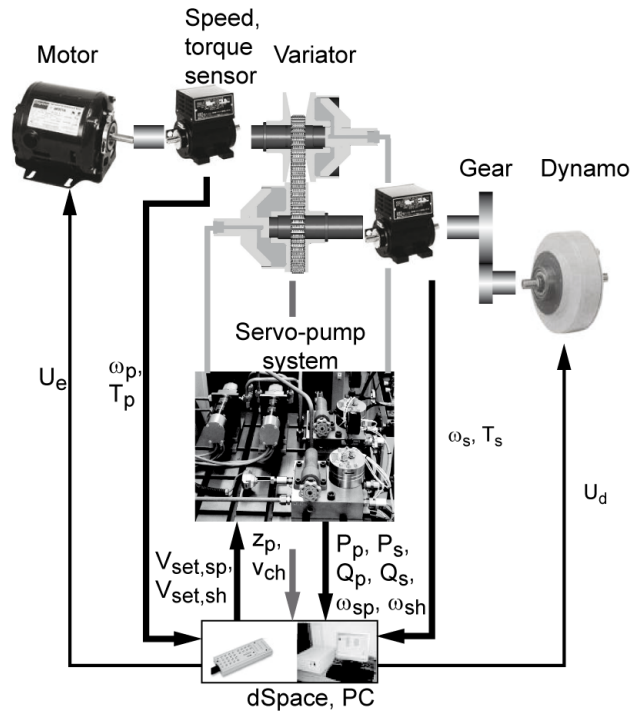


Figure G.1: Testing facilities overview

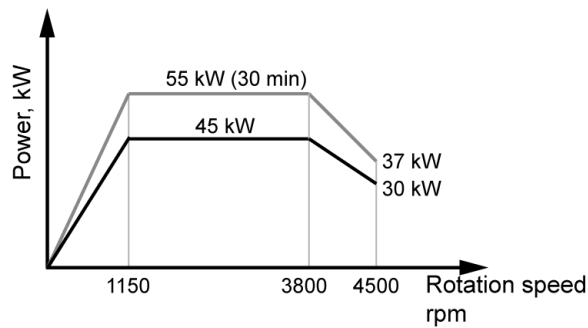


Figure G.2: Power characteristic of the electric motor that drive the variator

torsional deformation of a compliant shaft on which two gears target wheels are mounted. Two proximity sensors on each wheel measure the phase shift between the two signals to give the torque measurement. Also one of these signals is used to monitor the shaft speed like an encoder. This output sensor is therefore a torque/speed sensor. The torque and speed limits are respectively  $100Nm$  and  $6000rpm$ .

## G.4 CVT variator

The variator is a made home design. It was design to minimize the leakage and to increase the hydraulic pressure at low torque.

Parameter	Symbol	Value	Unit
Pulley distance	$d_a$	180	$mm$
Chain length	$l_{ch}$	747	$mm$
Chain width	$l_{pin}$	30	$mm$
Underdrive ratio	$r_{cvt,g}$	0.48	—
Primary radius	$R_p$	39	$mm$
Secondary radius	$R_s$	81.26	$mm$
Overdrive ratio	$r_{cvt,g}$	2.1	—
Primary radius	$R_p$	81.43	$mm$
Secondary radius	$R_s$	38.78	$mm$
Hydraulic piston area	$A_x$	40.62	$cm^2$

Table G.1: Specification of the the CVT variator

## G.5 Hydraulic system

The hydraulic system is composed of two servo motors, each connected to a bi-directional external gear pump. The flow generated by the servo pumps and the pulleys pressure are measured for both, the primary and the secondary pulley of the variator.

### G.5.1 Servo amplifier

The controller of the servo motor is a digital servo amplifier with sinusoidal current commutation for a control of electronic commutations (EC) motors. The EC motors must be equipped with Hall sensors and/or a digital encoder. The controller of the servo motor and, the monitoring of the speed or current (depends on the control mode) are implemented in a digital signal processor.

### G.5.2 Servo motor

The servo motor is a brushless motor having a power equivalent to  $400W$ . The maximum no load speed is  $3100rpm$  and the maximum torque is  $0.687Nm$ .

A brushless PM motors are constructed with electric windings on the stator and permanent magnets on the rotor.

### G.5.3 Pump

The hydraulic pump is a bi-rotational external gear pump with a displacement equal at  $0.88\text{cm}^3/\text{rev}$  and a maximum rotation speed of  $7000\text{rpm}$

## G.6 Test bench control

A dSPACE rapid prototyping system has been installed to control the test bench. This include a  $466\text{MHz}$  PowerPC 750 processor (DS1005 PPC board) and a multi input-output board (DS2201). The later is composed of 20 A/D channels, 8 D/A channels and 16 digital input-output lines. Using the dSPACE system with MATLAB/Simulink allows an easy generation of real time C code for control algorithm development.

This dSPACE system is connected to a personal computer to be able to generate the MATALB/Simulink files and to create an user interface.



## Appendix H

# CVT Linear Control

This appendix briefly describes the linear control used to control the secondary clamping force and the speed ratio used for the validation presented in *Chapter 6*.

*Chapter 5* discussed the variator and actuators dynamics. To simplify the synthesis, the slip model is not considered. The simplify model become :

$$\dot{r}_{cvt,g} = \omega_p G(r_{cvt,g}, F_s, L_f) \left[ \ln\left(\frac{F_p}{F_s}\right) - \ln\left(\frac{F_p}{F_s}\bigg|_{eq}\right) \right] \quad (\text{H.1})$$

$$\dot{P}_x = \frac{\beta_s}{V_{x,0} + A_x z_x} Q_x - \frac{A_x \dot{z}_x \beta_s}{V_{x,0} + A_x z_x} \quad (\text{H.2})$$

Where the two pulleys flows are given by :

$$Q_p = \frac{G_p \eta_p}{a_p s^2 + b_p s + 1} V_{p,set} \quad (\text{H.3})$$

$$Q_s = \frac{-G_p \eta_p}{a_p s^2 + b_p s + 1} V_{p,set} + \frac{G_{sp} \eta_{sp}}{a_{sp} s^2 + b_{sp} s + 1} V_{s,set} \quad (\text{H.4})$$

The system is non-linear and should be linearized at a certain working point to design the linear control, as for example a PID controller (Longchamp (1995), Guzzella (2004)).

The linearization can be easily obtain and will not be discussed here

### H.1 Transfer function

The two inputs of the MIMO system are the two voltages that set the rotation speed of the clamping and the shifting servo pump  $\mathbf{U} = [V_{p,set} \quad V_{s,set}]^T$  and the two outputs are the speed ratio and the secondary clamping force or pressure  $\mathbf{Y} = [r_{cvt} \quad P_s]^T$ . After linearization, the transfer function of the MIMO system yields to:

$$\begin{bmatrix} r_{cvt} \\ P_s \end{bmatrix} = \begin{bmatrix} H_{11}(s) & H_{12}(s) \\ H_{21}(s) & H_{22}(s) \end{bmatrix} \begin{bmatrix} V_{p,set} \\ V_{s,set} \end{bmatrix} \quad (\text{H.5})$$

The MIMO system can be decomposed in two SISO systems and two approaches can be pursued, depending on the basic requirements (Albertos & Sala (2004)):

- **decentralised control** tries to divide the plant and design independent controller for each of the subsystems as a way to handler the control of the overall plant. In this case, two alternatives:
  - neglect the coupling
  - carry out a decoupling
- **Cascade control**, adding extra sensors and actuators to improve closed-loop performance of a basic control loop.

For reason of simplicity, the decentralised control with neglect coupling is chosen. The secondary pressure and ratio control are separately design.

## H.2 Secondary pressure control

Figure H.1 depicts the control diagram of the secondary pressure. This layout shows that the regulator  $C_{P_s}$  has to fill the double function of regulation (rejection the perturbation  $V_{p,set}$ ) and tracking (following the pressure reference  $P_{s,ref}$ ). For example, the controller is design using the regulation case and considering the secondary pressure reference constant. A PI controller is enough to reject the perturbations. Usually, the controller also gives good response in tracking mode.

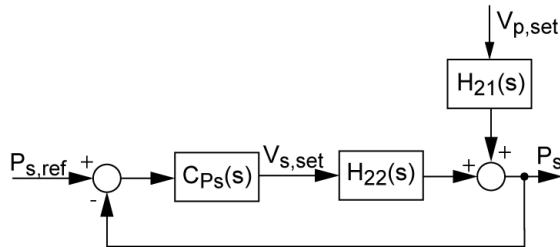


Figure H.1: Diagram of the secondary pressure control for the linear control of the CVT

## H.3 Ratio control

Figure H.2 depicts the control diagram of the ratio. This layout shows that the regulator  $C_{rcvt}$  has to fill the double function of regulation (rejection

the perturbation  $V_{s,set}$  and tracking (following the ratio reference  $r_{cvt,ref}$ ). For example, the controller is design using the regulation case and considering the secondary pressure reference constant. A PI controller is enough to reject the perturbations. Usually, the controller also gives good response in tracking mode.

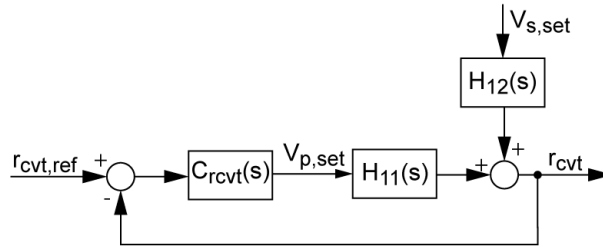


Figure H.2: Diagram of the ratio control for the linear control of the CVT



# Nomenclature

$A_{ch}$	Chain area, $m^2$	$N_n$	Normal force of the pin $n$ , $N$
$A_{pin}$	Area of the pin, $m^2$	$P_x$	Pulley pressure, $Pa$
$A_x$	Hydraulic area of the piston, $m^2$	$Q_x$	Pulley flow, $m^3/sec$
$D_y$	Total FEM axial pulley deformation, $m$	$Q_{x,ref}$	Pulley flow reference, $m^3/sec$
$D_{cl,y}$	Axial deformation due to the clearance between the shaft and the pulley, $m$	$R_x$	Non deform pulley radius, $m$
$D_{cl}$	Total axial deformation due to the clearance between the shaft and the pulley, $m$	$R_{\Gamma,pin}$	Crowning of the pin, $m$
$D_{fm}$	Total elastic deformation of the two pulley sheave, $m$	$R_{\Gamma,pl}$	Crowning of the pulley, $m$
$D_{n,y}$	FEM axial pulley deformation due to the normal force $n$ , $m$	$R_{\Lambda,pin}$	Crowning of the pin, $m$
$E_{ch}$	Young modulus of the chain, $N/m^2$	$R_{\Lambda,pl}$	Crowning of the pulley, $m$
$E_{pin}$	Young modulus of the pin, $N/m^2$	$R_{min,x}$	Minimum pulley radius, $m$
$E_{pl}$	Young modulus of the pulley, $N/m^2$	$S_f$	Safety factor
$F_x$	Pulley clamping force, $N$	$T_x$	Pulley torque, $Nm$
$F_{ax,n}$	Axial force acting on the pin $n$ , $N$	$T_{loss}$	Torque losses, $Nm$
$F_{ax}$	Total axial force acting on the pulley, $N$	$T_{max}$	Maximum theoretical transmissible torque, $N$
$F_{ch,n}$	Chain force acting on the pin $n$ , $N$	$T_{x,fr}$	Friction torque due to the chain slip. $Nm$
$F_{max}$	Maximum chain force, $N$	$V_r$	Radial chain speed, $m/s$
$F_{min}$	Minimum chain force, $N$	$V_x$	Pulley volume, $m^3$
$F_{x,fr}$	Friction force due to the chain slip, $N$	$V_{\theta}$	Tangential chain speed, $m/s$
$J_x$	Pulley inertia, $Nm^2$	$V_{x,0}$	Pulley initial volume, $m^3$
$L_f$	Load factor	$V_{x,set}$	Voltage input of the servo pump to set the rotation speed, $V$
$L_{ch}$	Chain length, $m$	$\Delta L_{pin}$	Compression of the pin, $m$
$L_{pin}$	Length of the pin, $m$	$\Delta P_{l,i}$	Contact loss, $W$
$M_s$	Total frictional torque, $Nm$	$\beta_0$	Non deformed pulley half angle, $rd$
$M_{ch}$	Chain weight element between the pulleys, $kg$	$\beta_e$	effective bulk modulus, $Pa$
		$\beta_s$	Sliding half angle, $deg$
		$\dot{R}_x$	Pulley radial velocity due to the shifting, $m/s$
		$\dot{r}_{cvt,g}$	Change rate of the geometrical ratio, $1/s$

$\dot{s}_x$	Change rate of the pulley slip, 1/s	$s_{sd}$	Standard slip synthesis
$\dot{s}_{tot}$	Change rate of the standard slip synthesis, 1/s	$s_{tot}$	Total slip
$\dot{s}_{tot}$	Change rate of the total slip, 1/s	$v_r$	Radial sliding velocity, m/s
$\dot{z}_x$	Axial speed of the movable pulley, m/s	$v_s$	Pulley sliding velocity, m/s
$\epsilon_{ch}$	longitudinal strain of the chain	$v_x$	Slip between the pulley sheave and the intermediate element, m/s
$\eta_x$	Pulley efficiency	$v_\theta$	Tangential sliding velocity, m/s
$\eta_T$	Torque efficiency	$v_{ch,0}$	Non deform chain speed, m/s
$\eta_{ch}$	Chain efficiency	$v_{ch}$	Chain speed, m/s
$\eta_s$	Slip efficiency	$v_{sd}$	Standard speed loss, m/s
$\eta_{var}$	Variator efficiency	$z_x$	Movable pulley sheave position, m
$\gamma_x$	Pulley wrapped angle, rd		
$\mu_x$	Pulley traction coefficient		
$\mu_{sd}$	Variator traction coefficient		
$\nu_{pin}$	Poisson coefficient of the pin		
$\nu_{pl}$	Poisson coefficient of the pulley		
$\omega_x$	Pulley speed, rd/s		
$\omega_{loss}$	Speed losses, rpm		
$\psi$	Sliding angle between the pin and the pulley sheave, rd		
$\sigma_{pin}$	Pin stress, N/m <sup>2</sup>		
$\sigma_{xy}$	Normal stress within the contact area between the pin and the pulley, N/m <sup>2</sup>		
$\theta_c$	Center of the edge expansion, rd		
$\theta_{def}$	Angular position where the pulley deformation is measured, rd		
$\xi$	Ratio between the minimum and the maximum chain force, $\xi = F_{min}/F_{max}$		
$dF_{fr}$	Differential friction force defined inside the contact area between the pin and the pulley, N/m <sup>2</sup>		
$dM_s$	Differential moment due to the friction forces, Nm/m <sup>2</sup>		
$d_a$	Pulley center distance, m		
$r$	Deformed pulley radius, m		
$r_{cvt,g}$	Geometrical ratio, $R_p/R_s$		
$r_{cvt}$	Speed ratio, $\omega_s/\omega_p$		
$s_x$	Pulley slip		
$s_{ref}$	Slip reference		

# Bibliography

- Abromeit, G. & Wilkinson, A. (1983). An Eletronic Control Concept for a Continuously Variable Transmission. *In Proc. of ISATA*, (vol. 1), pp. 31–45.
- Adachi, K., Wakahara, T., Shimanka, S., Yamamoto, M., & Oshidari, T. (1999). Robust Control System for Continuously Variable Belt Transmission. *JSAE Review*, (vol. 20), pp. 49–54.
- Akehurst, S., Vaughan, N., Parker, D., & Simner, D. (2004a). Modelling of Loss Mechanisms in a Pushing Metal V-belt Continuously Variable Transmission. Part 1: Torque Losses Due to Band Friction. *Proc Instn Mech Engrs, IMechE, Part D, Journal of Automobile Engineering*, (Vol 218), pp. 1269–1281.
- Akehurst, S., Vaughan, N., Parker, D., & Simner, D. (2004b). Modelling of Loss Mechanisms in a Pushing Metal V-belt Continuously Variable Transmission. Part 2: Pulley Deflection Losses and Total Torque Loss Validation. *Proc Instn Mech Engrs, IMechE, Part D, Journal of Automobile Engineering*, (Vol 218), pp. 1283–1293.
- Akehurst, S., Vaughan, N., Parker, D., & Simner, D. (2004c). Modelling of Loss Mechanisms in a Pushing Metal V-belt Continuously Variable Transmission. Part 3: Belt Slip Losses. *Proc Instn Mech Engrs, IMechE, Part D, Journal of Automobile Engineering*, (Vol 218), pp. 1295–1306.
- Albertos, P. & Sala, A. (2004). *Multivariable Control Systems: An Engineering Approach*. Springer. ISBN 1-85233-738-9.
- Asayama, H., Kawai, J., Tonohata, A., & Adachi, M. (1995). Mechanism of metal pushing belt. *JSAE Review*, (Review 16), pp. 137–143.
- Bonsen, B. (2006). *Efficiency Optimization of the Push-Belt CVT by Variator Slip Control*. PhD thesis, University of Eindhoven.
- Bradley, T. & Frank, A. (2002). Servo-Pump Hydraulic Control System Performance and Evaluation for CVT Pressure and Ratio Control. *VDI-Gesellschaft Entwicklung Konstruktion Vertrieb, CVT 2002 Congress*, (VDI-Berichte Nr. 1709), pp. 35–41.

- Carbone, G., Mangialardi, L., Bonsen, B., Tursi, C., & Veenhuizen, P. (2006). CVT Dynamics: Theory and Experiments. *Mechanism and Machinery Theory* 42, pp. 409–428.
- Carbone, G., Mangialardi, L., & Mantriota, G. (2001). Theoretical Model of Metal V-Belt Drives During Rapid Ratio Changing. *ASME, Journal of Mechanical Design*, (Vol 123), pp. 111–117.
- Carbone, G., Mangialardi, L., & Mantriota, G. (2003). EHL Visco-Plastic Friction Model in CVT Shifting Behavior. *Int. J. Veh. Des.* 32 (3/4), pp. 333–357.
- Carbone, G., Mangialardi, L., & Mantriota, G. (2005). The Influence of Pulley Deformation on the Shifting Mechanism of Metal Belt CVT. *ASME, Journal of Mechanical Design*, (Vol 127), pp. 103–113.
- Carbone, G., Scaraggi, M., & Mangialardi, L. (2008). EHL-squeeze at Pin-Pulley Interface in CVTs: Influence of Lubricant rheology. *Tribology International*, under review.
- Chen, C. (2004). *Linear System Theory and Design* (Third ed.). Oxford University press. ISBN 0-19-511777-8.
- Cools, S. & Veenhuizen, B. (2004). Model-based Servo Hydraulic Control of a Continuously Variable Transmission. *7th International Symposium on Advanced Vehicle Control (AVEC'04)*, pp 117–122.
- Englisch, A., Faust, H., Homm, M., Teubert, A., & Vornehm, M. (2004). Development of High Performance CVT Components. *International CVT and Hybrid Transmission Congress (CVT'04)*.
- Faust, H., Homm, M., & Reuschel, M. (2002). Efficiency-Optimised CVT Hydraulic and Clamping System. *VDI-Gesellschaft Entwicklung Konstruktion Vertrieb, CVT 2002 Congress*, (VDI-Berichte Nr. 1709), pp. 43–58.
- Gruber (1988). *Mécanique Générale*. Presses Polytechniques Romandes. ISBN 2-88074-155-6.
- Guzzella, L. (2004). *Analysis and Synthesis of SISO Control Systems*. ETH Zürich.
- Hanselman, D. D. (2003). *Brushless Permanent Magnet Motor Design*. The Writers' Collective. ISBN 1-932133-63-1.
- Harris, T. (1991). *Rolling Bearing Analysis* (Third ed.). John Wiley & Sons, Inc. ISBN 0-471-5134-0.
- Ide, T. (1999). Effect of effect of power losses of metal v-belt cvt components on the fuel economy. *Proceedings of Congress (CVT'99)*, pp. 93–98.



- Ide, T., Udagawa, A., & Kataoka, R. (1996). Experimental Investigation on Shift-Speed Characteristics of a Metal V-Belt CVT. *In Proc. of the International Congress on Continuously Variable Power Transmission (CVT'96)*, pp. 59–64.
- Ide, T., Udagawa, A., & Kataoka, R. (Tsukuba, Japan, 1994). A Dynamic Response Analysis of a Vehicle with a Metal V-Belt CVT. *In proc. of the 2<sup>nd</sup> Internat. Symp. on Advanced Vehicle Control (AVEC'94), col. 1*, pp. 230–235.
- Ioannou, P. A. & Jun, J. (1996). *Robust Adaptive Control*. Prentice Hall, Inc. ISBN 0-13-439100-4.
- Johnson, K. (1985). *Contact Mechanics*. Cambridge University Press. ISBN 0-521-34796-3.
- Kanokogi, K. & Hashino, H. (2000). Simulation of Metal Pushing V-Belt for CVT. *In Proceedings of the 15th ADAMS European User Conference*.
- Kim, H., Song, H., Kim, T., & Kim, J. (1996). Metal Belt CVT and Engine Optimal Operation by PWM Electro-hydraulic Control. *SAE Technical paper Series*, (No. 9636501), pp. 157–160.
- Kim, W. & Vachtsevanos, G. (2000). Fuzzy Logic Ratio Control for a CVT Hydraulic Module. *In Proc. of the 15th IEEE Internat. Symp. on Intelligent Control*, pp. 151–156.
- Klassen, T. (2007). *The Empact CVT, Dynamics and Control of an Electromechanically Actuated CVT*. PhD thesis, University of Eindhoven.
- Kobayashi, D., Mabuchi, Y., & Katoh, Y. (1998). A Study on the Torque Capacity of a Metal Pushing V-Belt for CVT's. *SAE Technical papers*, (No. 980822).
- Kurosawa, M. & Okahara, H. (2007). Future Innovations in Transmission. *Ingénieurs de l'Automobile*, (No. 791 bis), pp. 26–29.
- Linnenbruegger, A., Baumann, M., & Endler, T. (2004). High Performance Chain CVTs and Their Tribological Optimisation. *Proceeding of TVT Congress, Tribology of Vehicle Transmissions*, pp. 14–19.
- Linnenbruegger, A., Englisch, A., A.Goetz, Simon, E., Teubert, A., & Vornehm, M. (2007). High Performance CVT Components by Luk - A Key Factor for Improved Fuel Efficiency -. *Society of Automotive Engineers of Japan, International Congress on Continuously Variable and Hybrid Transmission*, (No. 20074572), pp. 177–182.
- Longchamp, R. (1995). *Commande numérique de Systèmes Dynamiques*. Ecoles Polytechniques Fédéral de Lausanne. ISBN 2-88074-282-X.

- Merritt, H. E. (2001). *Hydraulic Control Systems*. John Wiley & Sons. ISBN 0-471-59617-5.
- Metsenaere, C. D., Veenhuizen, P., Commissaris, G., Klassen, T., Nelissen, J., & van Rooij, J. (2005). Modeling, Simulation and Control of a Power Loop Test Rig for Continuously Variable Transmissions. *Proc. EAEC*.
- Micklem, J., Longmore, D., & Burrows, C. (1994a). Belt Torque Losses in a Steel V-Belt Continuously Variable Transmission. *Proc Instn Mech Engrs, Part D: Journal of Automobile Engineering*, (Vol. 208), pp. 91–97.
- Micklem, J., Longmore, D., & Burrows, C. (1994b). Modelling of the Steel Pushing V-Belt Continuously Variable Transmission. *Proc Instn Mech Engrs, Part D: Journal of Automobile Engineering*, (Vol 208), pp. 13–27.
- Micklem, J., Longmore, D., & Burrows, C. (1996). The Magnitude of the Losses in the Steel Pushing V-belt Continuously Variable Transmission. *Proc Instn Mech Engrs, IMechE, Part D, Journal of Automobile Engineering*, (Vol 210), pp. 57–62.
- Ohm, Y. (1997). TDynamic Model of PM synchronous Motors. *Technical report, Drivetech inc., Blacksburg, Virginia*.
- Oudijk, M. (2005). Optimization of CVT Control For Hybrid and Conventional Drive Lines. Master's thesis, Eindhoven University of Technology.
- Poll, G., Kruse, T., & Meyer, C. (2006). Prediction of Losses in Belt-type Continuously Variable Transmission Due to Sliding Between Belt and Disc. *Proc. IMechE Part J: Journal Engineering Tribology*, (Vol 220), pp. 235–243.
- Poll, G. & Meyer, C. (2007). Losses in Continuously Variable Transmission (CVT) due to Sliding Motion and Ratio Change. *Society of Automotive Engineers of Japan, International Congress on Continuously Variable and Hybrid Transmission*, (No. 20074546), pp. 25–30.
- Pulles, R. (2004). Slip Controller Design and Implementation in a Continuously Variable Transmission. Master's thesis, Eindhoven University of Technology. Report No DCT 2004-102.
- Pulles, R., Bosen, B., Steinbuch, M., & Veenhuizen, P. (2005). Slip Controller Design and Implementation in a Continuously Variable Transmission. *American Control Conference, Portland, Oregon*.
- Rothenbühler (2005). Dynamic Simulation with DADS (Dynamic Analysis Design and System). *Internal JTEKT research*.
- Sakagami, K., Fuji, T., Yoshida, H., & Yagasaki, T. (2007). Study on Belt Slip Behavior in Metal V-belt type CVT. *Society of Automotive Engineers of Japan, International Congress on Continuously Variable and Hybrid Transmission*, (No. 20074565), pp. 135–139.

- Sastry, S. & Bodson, M. (1989). *Adaptive Control, Stability, Convergence, and Robustness*. Prentice Hall, Inc. ISBN 0-13-004326-5.
- Sato, K., Sakakiyama, R., & Nakamura, H. (1996). Development of Electronically Controlled CVT System Equipped with CVTip. *SAE Technical Paper Series*, (No. 9636321).
- Sattler, H. (1999). Efficiency of Metal Chain and V-Belt CVT. *International Congress on Continuously Variable Transmissions*, (CVT'96), pp. 99–104.
- Sferra, D., Pennestri, E., Valentini, P., & Baldascini, F. (2002). Dynamics Simulation of a Metal-Belt CVT under Transient Conditions. *Proceedings of the DETC02, ASME Design Engineering Technical Conference*, (Paper No. DETC02/MECH-34228, Vol 5A), pp. 261–268.
- Shafai, E., Simons, M., Neff, U., & Geering, H. (1995). Model of a Continuously Variable Transmission. *JSAE*, (No. 9636330).
- Shastri, S. & Franck, A. (2004). Comparison of Energy Consumption and Power Losses of a Conventionally Controlled CVT and with a Belt and Chain as the Torque Transmitting Element. *International CVT and Hybrid Transmission Congress*.
- Simons, S. (2006). Shift Dynamics Modelling For Optimization of Variator Slip Control in a Continuously Variable Transmission. Master's thesis, Eindhoven University of Technology. Report No. DCT 2006-081.
- Simons, S., Klaassen, T., Veenhuizen, B., & Carbone, G. (2006). Shift Dynamics Modeling For Optimization Variator Slip Control in a Continuously Variable Transmission. *Society of Automotive Engineers of Japan, FISITA, World Automotive Congress*, (F2006P208).
- Slotine, J.-J. & Li, W. (1991). *Applied Nonlinear Control* (1st ed. ed.). Prentice Hall. ISBN 0-13-040890-5.
- Sorge, F. (1996). Influence of Pulley Bending on metal V-belt Mechanics. *International Congress on Continuously Variable Transmissions*, (CVT'96).
- Sorge, F. (2007). Shift Mechanics of Metal Belt CVT. *Society of Automotive Engineers of Japan, International Congress on Continuously Variable and Hybrid Transmission*, (No. 20074542), pp 1–6.
- Spijker, E. (1994). *Steering and Control of a CVT Based Hybrid Transmission for a Passenger Car*. PhD thesis, University of Eindhoven.
- Srivastava, N. & Haque, I. (2007). Clearance-induced Nonlinear Dynamics of Chain CVT Drives. *Society of Automotive Engineers of Japan, International Congress on Continuously Variable and Hybrid Transmission*, (No. 20074545), pp. 19–24.

- Srivastava, N., Miao, Y., & Haque, I. (2006). Influence of Clearance on the Dynamics of Chain CVT Drives. *Proceeding of IMEC2006, ASME International Mechanical Engineering Congress and Exposition*, (No. IMECE2006-14059), pp. 163–175.
- Srnik, J. (1998). *Dynamik von CVT-Keilkettengetrieben*. PhD thesis, University of Munich.
- Tarutani, I., Tani, H., & Nagasawa, Y. (2006). Analysis of the Power Transmission Characteristics of a Metal V-Belt Type CVT. *Research paper, R&D Review of Toyota CRDL*, (Vol. 40, No. 3), pp. 6–13.
- Tenberge, P. (2004). A New Mathematical Model for a very fast Calculation of a Chain Forces, Clamping Forces, Clamping Ratio, Slip and Efficiency. *International CVT and Hybrid Transmission Congress*.
- Vaccaro, R. (1995). *Digital Control, A State-Space Approach*. McGraw-Hill, Inc. ISBN 0-07-066781-0.
- van de Meerakker, K., Rosielle, P., Bonsen, B., Klassen, T., & Liebrand, N. (2004). Mechanism proposed for ratio and clamping force control in a cvt. *In proceedings of the FISITA 2004 World Automotive Congress*, (F2004F108).
- van der Laan, M. & Luh, J. (1999). Model-based Variator Control Applied to a Belt Type CVT. *In Proc. of the Internat. Congress on Continuously Variable Power Transmission (CVT'99)*, pp. 105–110.
- van der Laan, M., van Drogen, M., & Brandsma, A. (2004). Improving Push Belt CVT Efficiency by Control Strategies Based on New Variator Wear Insight. *International CVT and Hybrid Transmission Congress*, (No. 04CVT-39).
- van der Meulen, A. (2006). Pulley Positioning System for CVT. Master's thesis, Eindhoven University of Technology. Report No. DCT 2006.28.
- van Drogen, M. & van der Laan, M. (2004). Determination of Variator Robustness Under Macro Slip Conditions for a Push Belt CVT. *SAE International World Congress*, (No. 2004-01-0480).
- van Eersel, K. (2005). Slip Behavior in the Variator by Measuring the belt speed. Master's thesis, University of Eindhoven.
- van Rooij, J., Commissaris, G., van de Meerakker, K., & Nelissen, J. (2007). The GCI High Torque CVT Chain for Torques up to 2500 Nm. *Society of Automotive Engineers of Japan, International Congress on Continuously Variable and Hybrid Transmission*, (No. 20074571), pp. 171–175.
- Veenhuizen, J., Bonsen, B., Klaassen, T., K.G.O, van de Meerakker, & Veldpaus, F. (2002). Variator loading and control in a V-belt type geared neutral

- transmission in and around the geared neutral point. *VDI-Gesellschaft Entwicklung Konstruktion Vertrieb, CVT 2002 Congress*, (VDI-Berichte Nr. 1709), pp. 297–309.
- Vroemen, B., Serrarens, F., & Veldpaus, F. (2000). CVT Control: a Hierarchical Approach. *in Proc. of Intern. Symposium on Advanced Vehicle Control*.
- Wade, J. (1984). An Integrated Electronic Control System for a CVT Base Powertrain. *In Proc. of ISATA*, (vol. 1 No. 84006).
- Wallmark, O. (2002). Modeling of Permanent-Magnet Synchronous Machines with Non-sinusoidal Flux Linkage. *Technical report, Department of Electric Power Engineering, Chalmers University of Technology, Sweden*.
- Yamaguchi, H., Tani, H., & Hayakawa, K. (2006). Measurement and Estimation Technologies for the Experimental Analysis of Metal V-belt Type CVTs. *Research paper, R&D Review of Toyota CRDL*, (Vol. 40, No. 3), pp. 6–13.



# Curriculum Vitae

## Personal Data

Name Yves Rothenbühler  
Date of Birth 30 May 1973  
Place of Birth Geneva, Switzerland  
Nationality Swiss

## Education

2005 - 2009 Ph.D. in Technical Science  
Swiss Federal Institute of Technology, Lausanne (EPFL)  
Joint research between the Mechanical Systems Design  
Laboratory, the Robotic Systems Laboratory and  
JTEKT Co., Japan  
1993 - 1999 Master of Science in Microtechnical Engineering  
Swiss Federal Institute of Technology, Lausanne (EPFL)  
Major in production and robotics  
1987 - 1993 Engineer ETS/HES in electricity science Engineering  
Engineer School of Geneva (EIG), Switzerland  
Major in electricity with orientation in computer Science

## Professional Experiences

2003 - 2008 Assistant Manager at Mechatronic Systems Research  
& Development Department of JTEKT Co. in Nara, Japan.  
Conducted modeling and control of CVT (Continuous Variable  
Transmission)  
2000 - 2003 Engineer development at Development Units Department of  
JTEKT Co. in Osaka, Japan.  
Development of active magnetic bearings high speed  
spindle.  
1999 - 2000 Internship at Mechatronics Systems Research & Development  
Department of JTEKT Co. in Nara, Japan.  
Development of low power active magnetic bearings.